Department of Electrical and Electronic Engineering

Imperial College London

Low Cost Fabrication Processing for Microwave and Millimetre-Wave Passive Components

Mario D'Auria

A thesis submitted for the degree of Doctor of Philosophy of

Imperial College London

and the

Diploma of the Imperial College

October 2015

ABSTRACT

Microwave and millimetre-wave technology has enabled many commercial applications to play a key role in the development of wireless communication. When dissipative attenuation is a critical factor, metal-pipe waveguides are essential in the development of microwave and millimetre-wave systems. However, their cost and weight may represent a limitation for their application.

In the first part of this work two 3D printing technologies and electroless plating were employed to fabricate metal pipe rectangular waveguides in X and W-band. The performance for the fabricated waveguides was comparable to the one of commercially available equivalents, showing good impedance matching and low attenuation losses. Using these technologies, a high-performance inductive iris filter in W-band and a dielectric flap phase shifter in X-band were fabricated. Eventually the design and fabrication of a phased antenna array is reported.

For microwave and millimetre-wave applications, system-on-substrate technology can be considered a very valuable alternative, where bulky coax and waveguide interconnects are replaced by low-loss transmission lines embedded into a multilayer substrate, which can include a wide range of components and subsystems. In the second part of this work the integration of RF MEMS with LTCC fabrication process is investigated. Three approaches to the manufacture of suspended structures were considered, based on laser micromachining, laser bending of aluminium foil and hybrid thick/thin film technology. Although the

fabrication process posed many challenges, resulting in very poor yield, two of the solution investigated showed potential for the fabrication of low-cost RF MEMS fully integrated in LTCC technology.

With the experience gained with laser machining, the rapid prototyping of high aspect ratio beams for silicon MEMS was also investigated. In the third part of this work, a statistical study based on the Taguchi design of experiment and analysis of variance was undertaken. The results show a performance comparable with standard cleanroom processing, but at a fraction of the processing costs and greater design flexibility, due to the lack of need for masks.

DECLARATION OF ORIGINALITY

The results reported in Chapter 3 and 5 were obtained through a collaboration with the University of Leeds, under the IeMRC grant for “3D microwave and Millimetre-wave System-on-substrate using Sacrificial Layers for Printed MEMS Components”, consisting of joint work with Dr Razak Mohd Ali Lee and Ayodeji Sunday.

The results reported in Chapter 7 were obtained from the joint work with Tim Pusch and Dr Nima Tolou, from the Delft University of Technology (Netherlands), under the guidance of Prof Andrew Holmes. All other results reported in this thesis are primarily due to the author, except from background results, which are clearly referenced.

COPYRIGHT DECLARATION

“Non est ad astra mollis, sed per aspera e terris via”
Not through the easy path, but through the hard one
is the way from the earth to the stars.
Seneca

“The scientist is not a person who gives the right answers,
he's one who asks the right questions”
Claude Levi-Strauss

ACKNOWLEDGEMENTS

During the long time spent in Imperial I had the luck of meeting many people that helped and supported me along this journey. For all of them I have fond memories of the help they gave me and the relax moment we shared, because more than on office of colleagues I can say I found a second family away from home. Naming them all would only me a memory exercise, but still I would like express my gratitude in written for some of them and first I want to thank Dr Munir M. Ahmad. I start with him because I don't think he receives the right amount of acknowledgements for all his work and the knowledge he regularly brings to the group. In the specific I want to thank him more than for the notions of chemistry and processing, for the long chats about life and the exchange of opinions on the most different topic, because these are the things that make you grow. Secondly, a well-deserved thank you goes to Prof Andrew Holmes. The amount of knowledge I could absorb by working with him is invaluable and I'm grateful for that. Among the academics a special acknowledgements goes to Dr Tom Tate for being my inspiration in teaching and if I obtained a student choice award is also thanks to him. Last, but surely not less important, my supervisor Dr Stepan Lucyszyn deserves an acknowledgement not only for his merits as supervisor, but also for the many life lessons I learned for being his student.

I am also grateful I shared this journey with people like Fangjing, Tasmiat, Krystallo, Hadri and Dixi, which supported me so much in these years. Many others should be named, but deep in my heart they will never be forgotten.

CONTENTS

LIST OF FIGURES

LIST OF TABLES

NOMENCLATURE

g	Gap height of the cantilever
g_0	Maximum gap height (no bias)
A	Actuation electrodes overlapping area
a a	Broadwall size of a rectangular waveguide
$AF(\theta)$	Array factor
d	Distance between elements of the array antenna
d_{max}	Maximum distance between array antenna elements to achieve θ_{max}
E	Young's modulus
F	Load applied on a cantilever beam
f	Frequency
F_e	Electrostatic force
F_r	Beam's restoring force
I	Second moment of area
k	Spring constant (with exception of the wavenumber)
k_c	Spring constant for a concentrated load
k_d	Spring constant for a uniformly distributed load
k_t	Spring constant for a triangularly distributed load
l	Cantilever beam length
L	Distance between anchors of a buckled beam
L_0	Beam length before buckling
p	Bottom foxed actuation electrode length
P	Axial load applied on a beam

$P_{cr\,f\text{-}f}$	Critical minimum load to generate buckling in a fixed-fixed beam
PO	Pulse overlap
R	Perpendicular reaction force at the fixed end of a buckled beam
ss	Laser spot size
t	Cantilever beam thickness
$tan(\delta)$	Loss tangent
V	Voltage applied between the actuation electrodes
w	Cantilever beam width
w_{eff}	Effective beam width to compensate for fringing fields effect
δ	Beam deflection
δ_c	Deflection for a concentrated load
δ_d	Deflection for a uniformly distributed load
δ_t	Deflection for a triangularly distributed load
θ	Array antenna look angle
θ_{max}	Array antenna maximum desired look angle
λ	Free space wavelength
λ_g	Guide wavelength
$v(x)$	Deflection along a buckled beam
ξ_0	Maximum load for a triangularly distributed load
ψ	Progressive relative phase shift
ε_0	Permittivity of vacuum
ε_{eff}	Relative dielectric constant in a dielectric slab loaded waveguide
ε_r	Relative dielectric constant

Abbreviations

ABS	Acrilonitrile Butadiene Stirene
AM	Additive Manufacturing
ANOVA	ANalysis Of Variance
CAD	Computer Assisted Drawing
CNC	Computer Numerically Controlled
CPW	Co-Planar Waveguide
CVD	Chemical Vapour Deposition
DC	Direct Current
DLP	Digital Light Processing
DOE	Design Of Experiment
DOF	Degree Of Freedom
DPSS	Diode-Pulses Solid-State
DRIE	Deep Reactive Ion Etching
FDM	Fused Deposition Modeling
FET	Field Effect Transistor
HEMT	High Electron Mobility Transistor
HF	Hydro-fluoridric acid
HTCC	High Temperature Co-fired Ceramic
IC	Integrated Circuit
IR	Infrared
LCP	Liquid Crystal Polymer

LIGA	Lithographie, Galvanoformung, Abformung – Lithography, Electroplating, and Molding
LTCC	Low Temperature Co-fired Ceramic
LTTT	Low Temperature Transfer Tape
MEMS	Micro Electro Mechanical System
MSD	Mean Square Deviation
PAS	Pressure Assisted Sintering
PCB	Printed Circuit Board
PIN	p-type – intrinsic – n-type
PLA	PolyLactic Acid
PLAS	Pressure-Less Assisted Sintering
PM-AM	Phase to Amplitude
PVD	Physical Vapour Deposition
RF	Radio Frequency
RIE	Reactive Ion Etching
RP	Rapid Prototyping
S/N	Signal to Noise
SFF	Solid FreeForm
SIW	Substrate Integrated Waveguide
SLA	Stereolithography Apparatus
SLS	Selective Laser Sintering
SoS	System on Substrate
SPnT	Single Pole n-Throw
SPST	Single Pole Single Throw

STL	Standard Tessellation Language
TCE	Thermal Coefficient of Expansion
UV	Ultra-Violet

CHAPTER 1: INTRODUCTION

1.1 General overview

Microwave and millimetre-wave technology has enabled many commercial applications to play a key role in the development of wireless communication. Today this technology is ubiquitous in everyday life and many standards have been defined on the use of this frequency range. For example, IEEE 802.11 (Wi-Fi) and IEEE 802.15 (Bluetooth) standards, along with all the high speed communication standards recently developed that are generally categorised under the name of 4G.

Although technologies such as Wi-Fi and Bluetooth, with their relative standards, were originally developed more than two decades ago, only recently they have become an essential part for a vast majority of personal, household and industrial devices, from mobiles to smart home appliances. Generally this delay from development to widespread availability is caused by the initial cost of these technologies and in many cases the limitations are imposed by manufacturing costs the active devices. However, with the development of new processes in the semiconductor industry and with higher performance substrates these limitations are often overcome in a relatively short time. Conversely, the same is not true for passive components, such as waveguides and waveguide integrated filters, which still rely on mechanical machining and welding. In fact, the manufacturing process for these components has not changed significantly in many decades and, because of this, associated the price has dropped only marginally.

When dissipative attenuation is a critical factor, metal-pipe waveguides are essential in the development of microwave and millimetre-wave systems. However, because of the aforementioned reasons, their cost can increase exponentially with operating frequency and their size/weight may represent a limitation for their application. Moreover, complex geometry components (e.g. bends, twists and splitters) pose challenges in their manufacture.

In the first part of this work, an alternative manufacturing process based on 3D printing will be demonstrated for the manufacture of lightweight, low-cost, microwave and millimetre-wave metal-pipe rectangular waveguides (MPRWGs).

1.2 Rapid prototyping and 3D printing – technology overview

The term "rapid prototyping" (RP) is used to identify a group of processes used to quickly fabricate models of parts using three-dimensional (3D) computer aided design (CAD) data. RP, referred often as solid freeform (SFF) manufacturing or more commonly as additive manufacturing (AM), was born as a way to visualise and inspect the design of an object before production. Other applications include the study of aerodynamics, as it allowed one to build a scale model to be tested in a smaller wind tunnel. While particularly expensive at its early stages, this technology has now become more affordable and widely available for hobbyists. This increasing popularity, together with its ability to transform a CAD drawing into a solid object, led the general public to introduce the new and more widely recognised term '*3D printing*'. This name is now also widely accepted and, hence, the equipment used for AM is now commonly referred to as a 3D printer.

As both definitions of additive manufacturing and 3D printing suggest, this family of technologies is based on the deposition of material, layer by layer, to achieve three-dimensional objects. This represents the main difference from computer numerically controlled (CNC) milling, which is a subtractive process. CNC used to be the method of choice for the production of 3D objects, often requiring post-machining assembly. Because of the very low waste of material and the ability to easily create geometrically complex shapes, 3D printing is becoming of ever increasing interest, not only for rapid prototyping but also for manufacturing. This fabrication process has proved to be economically advantageous in several cases: when high value materials are required and the low amount of waste becomes a key factor towards the final cost of the item. For example, 3D printing was used in the fabrication of aeroplane engines, where a great amount of high value metals, such as titanium, are generally wasted during standard CNC machining. For such applications, 3D printing is also used to fabricate moulds for casting. This increase in process efficiency combines also with the flexibility of the process. Indeed, whether as directly printed or casted in a 3D printed mould, one single 3D printer is able to produce an unlimited variety of designs with high complexity geometries, without the need for assembly. This effectively reduces not only material waste but also fabrication time. 3D printing is also finding applications for the production of small batches – from one to a few thousand pieces – of plastic items as an alternative to injection moulding, as no initial cost is required for the mould and unforeseen problems can be solved without adding costs.

1.2.1 3D printing technologies

Depending on the application, a great variety of 3D printers are available on the open market, based on a variety of technologies, but all sharing the same principle of building sequentially layer by layer. To achieve this, software, usually referred to as a "slicer", is used to convert the 3D CAD model into a sequence of layers – slices – that will be deposited one at a time. The most widely accepted input file format for "slicer" software is Standard Tessellation Language (STL), which is now considered as a universal standard for 3D printing. The produced output file, which then is read by the printer, is most often proprietary to the equipment, but in general is based on the G-CODE format. The G-CODE file format, also known as RS-274, was originally developed for CNC machining and printed circuit board prototyping and is used in additive material technology to describe the tool path.

It is not easy to categorise each 3D printing technology, as each mutation has its own name, but for simplicity it is possible to group them into three general families: selective deposition of extruded material, which includes fused deposition modelling (FDM) [1]; UV curing of resin, which includes inkjet printing and stereolithography apparatus (SLA) technology [2]; and powder binding, which includes selective laser sintering (SLS) [3].

Fused deposition modelling (FDM)

FDM 3D printing, also known as fused filament fabrication (FFF), has become a very popular technology for rapid prototyping of models where high definition is not required. This technology is based on the melting of thermoplastics, which is then extruded through a nozzle and selectively deposited, as illustrated in Figure 1.1.

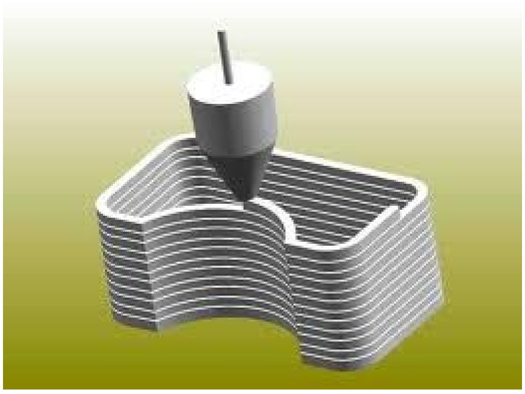

Figure 1.1: Example of FDM technology's working principle. The plastic filament is pushed through a heated nozzle and the melted material is deposited [4].

This technology is characterised by a low manufacturing cost, both for equipment and materials. With FDM printers it is possible to use several kinds of thermoplastics, but the most commonly used are acrylonitrile butadiene styrene (ABS) and polylactic acid (PLA). With FDM 3D printing the minimum feature size is limited by the nozzle aperture diameter, generally 400 µm wide. The lateral surfaces of the printed item will also show visible ridges, more or less evident depending on the chosen layer height. Aside from its resolution, one of the major drawbacks of this technology is the difficulty in realising unsupported suspended structures. To create suspended structures, a support structure needs to be printed. This support structure, which is usually created in the same material as the building one, has to be mechanically removed, resulting in scarring of the surface. To overcome this, professional FDM 3D printers often offer two nozzles, one for the building material and one for soluble support material.

Stereolithography apparatus (SLA)

Stereolithographic 3D printing was the first commercial process for AM. In its original configuration a UV laser is scanned on the surface of a photosensitive resin contained in a vat, as illustrated in Figure 1.2. As the thin superficial layer of resin is cured, the platform is lowered, exposing a fresh layer of liquid resin.

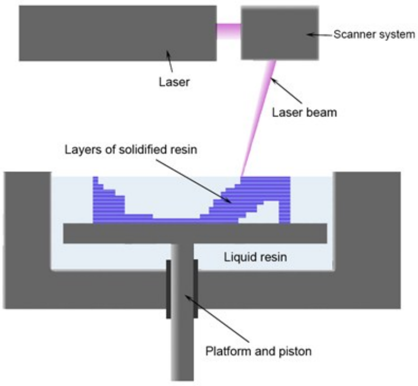

Figure 1.2: Example of SLA technology. The vat is filled with resin and a scanned UV laser beam cures the superficial layer [5].

The small spot size of the laser and the low viscosity of the resin allow for much smoother surfaces and smaller feature size. On the other hand, the running costs of this technology are roughly two to three orders of magnitude higher than FDM printing. The higher costs are mainly driven by the expensive, short shelf-life resins; increasing exponentially with the working area dimensions of the equipment, as it requires more expensive optics and more accurate mechanics. For this reason SLA technology has been mainly employed in high value markets like jewellery and dentistry, for the fabrication models to use for '*lost wax investment casting*'. Depending on the composition of the photosensitive resin, it can exhibit different properties, from high temperature resistance to flexibility, and it is possible to also load such resins with ceramic, silica or other powders, to change its properties.

A less expensive alternative to the use of UV lasers was developed using digital light processing (DLP®) projectors. While the curing process is similar, the whole layer is illuminated at once, making the process inherently faster. However in this case the resolution is proportional to the projected one, eventually causing restrictions on the maximum working area and, therefore, lower throughput.

Selective laser sintering (SLS)

SLS technology is based on the laser sintering of powders. With an underlying concept very similar to SLA printing, in a tank full of powder, the most superficial layer is laser sintered according to the layer pattern, as illustrated in Figure 1.3. Then the tank bottom platform is lowered and another layer of powder is deposited and compacted with a roller; the process then repeats. The procedure is common for a wide variety of powders, from plastics (e.g. nylon) to metals (e.g. titanium). In this case the laser is generally a CO_2 laser, which is in the mid-infrared region (10 µm wavelength).

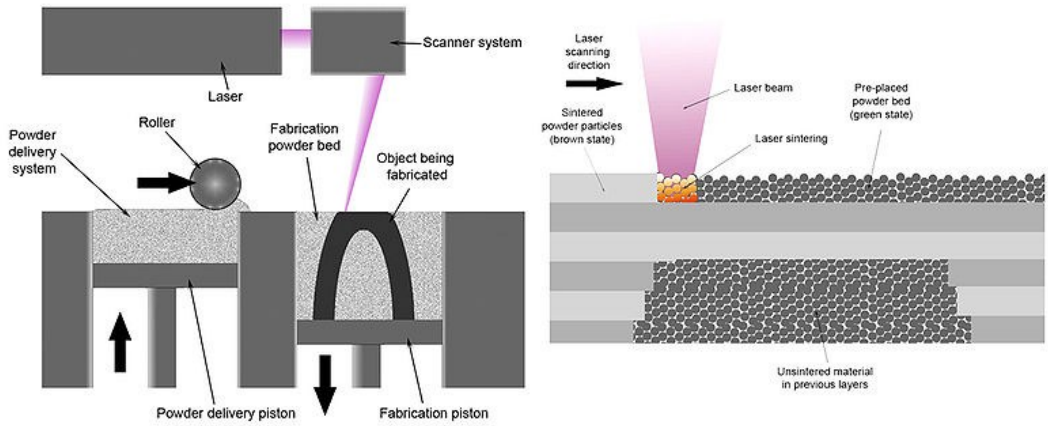

Figure 1.3: Example of SLS technology. After a layer of powder is spread onto the working area, a laser beam scans across the surface layer of powder to sinter it [6].

The resolution in this technology is not only defined by the laser spot size, but from the powder particle dimensions; surface finish quality is generally relatively low, with usually visible roughness. The advantage with this technology is given by the un-sintered powder that works as a support for suspended parts. This enables higher geometrical complexity and the fabrication of readily-assembled structures (i.e. joints, hinges and roller bearings) that would otherwise be impossible to realize. This technology is also preferred when large items are needed.

1.2.2 3D printing in research

3D printing is finding increasing interest in research, for an ever-expanding diversity of applications. Over the past two decades it has attracted the attention of researchers working on electromagnetic metamaterials (e.g. anisotropic metamaterial components [7] and dielectric cloaking [8]) and radio frequency (RF) components (e.g. antennas and filters [9]–[11]). This technology also enabled a simplified manufacturing of Luneburg and graded index lenses [12], [13]. Moreover, at THz frequencies hollow core and plasmonic waveguides were proposed [14]–[16]. A more complete list of 3D printed components for RF applications from the open literature is reported in the following chapter.

1.3 RF MEMS and LTCC

For microwave and millimetre-wave applications, system-on-substrate (SoS) technology can be considered a very valuable alternative, where bulky coax and waveguide interconnects are replaced by low-loss transmission lines embedded into a multilayer substrate, which can include a wide range of components and subsystems.

Advantages are substantially enhanced if RF microelectromechanical systems (RF MEMS) can be integrated with the substrate. Looking at manufacturing costs, it is a much more attractive proposition to integrate the fabrication of RF MEMS components in ceramic or organic laminate technology. Of particular relevance is low temperature co-fired ceramic (LTCC) technology. This was found to be very useful in the realization of compact RF multi-chip modules and for conventional RF MEMS packaging, as is allows the fabrication of robust and hermetic cavities, fundamental for the good performance of such devices.

The aim in the second part if this work is the realisation of RF MEMS components embedded directly onto a ceramic substrate with only modest extra process complexity. The development of this technology would lead to a manufacturing process that is capable of low-cost large-scale SoS designs for applications such as switches, variable capacitors and active antenna arrays. With surface micromachining, using a sacrificial layer, new MEMS devices and 3D structures can be fabricated for many applications in the microwave and millimetre-wave frequencies range. Furthermore, the embedding of bare chip active devices, RF MEMS and high-Q RF passive elements within a single temperature coefficient of expansion (TCE) matched and robust package will offer outstanding capabilities and low cost of manufacture for high frequency and harsh environment applications.

1.3.1 RF MEMS – Technology overview

RF MEMS is the technology that combines microelectromechanics and RF functionality. This technology is generally associated with semiconductor microfabrication processing that results in creating high performance tuneable RF filters and phase shifters; offering significant advantages over a great range of applications, from smart sensor networks to mobile handsets. Other significant applications are in the field of reconfigurable networks and subsystems, where the overall system size and weight reduction plays a fundamental role, making RF MEMS a very important enabling technology. The advantage of using RF MEMS instead of other options, like PIN (p-type–Intrinsic–n-type) diodes and switching field effect transistor (FET), is the lower insertion loss and higher isolation, signal power linearity and Q-factor. On the other hand, they have a shorter life-cycle, generally require higher control voltages and special packaging [17]. The latter, in particular, contributes significantly to the cost of each single device, as hermetic packaging in inert gas is usually required.

1.3.2 RF MEMS Examples

RF MEMS for circuit applications can be categorised into switching and tuneable devices. The former are used to connect or disconnect signal lines or to re-route a signal, and can be divided into ohmic and capacitive switches. These find applications in reconfigurable networks and phase shifters. The second category, consists of capacitors or inductors whose value can be changed, and are generally used for realizing tuneable filters and resonators.

In the open literature, many examples are demonstrated for both categories. Examples of ohmic contact and capacitive membrane RF MEMS switches are shown in Figure 1.4 and 1.5. With ohmic contact switches a physical connection is made between metals; with capacitive membrane switches a thin dielectric layer on one of the contacts creates a significant shunt capacitance that only allows the high frequency signal to propagate through, blocking any DC component.

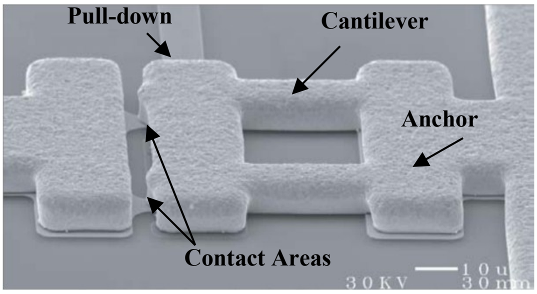

(a)

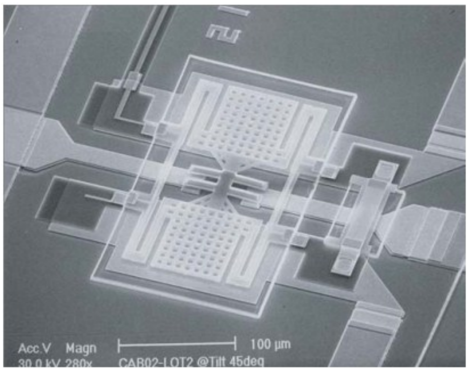

(b)

Figure 1.4: Ohmic contact switches from (a) Analog Devices and (b) Rockwell Scientific [17].

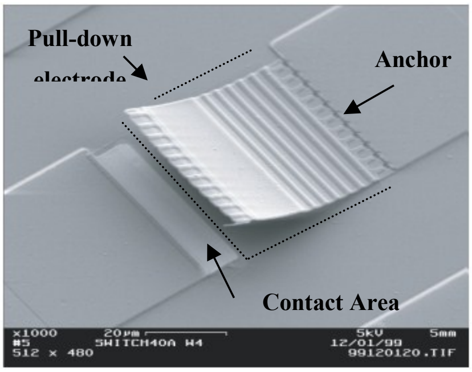

(a)

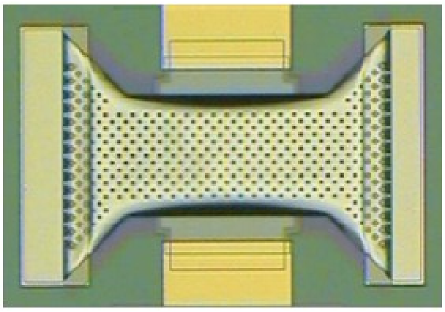

(b)

Figure 1.5: Capacitive membrane switches developed by (a) Lincoln Labs and (b) Raytheon [17].

These switch types are defined as single-pole single-throw (SPST), as only one output signal electrode can be selected. Such switches have been successfully used in the development of delay-line phase shifters; for example as the one illustrated in Figure 1.6, developed by the University of Michigan and Rockwell Scientific [17]. However, it is possible to find more advanced switches that, within the same device, are able to route an input signal to multiple points and are defined as single-pole n-throw (SPnT). A good example is the single-pole eight throw (SP8T) ohmic contact switch developed at Imperial College London, based on the wobble motor principle shown in Figure 1.7. In this device the input signal travels up the axis of the motor and the electrostatically actuated rotor acts as the switching connector [18], [19].

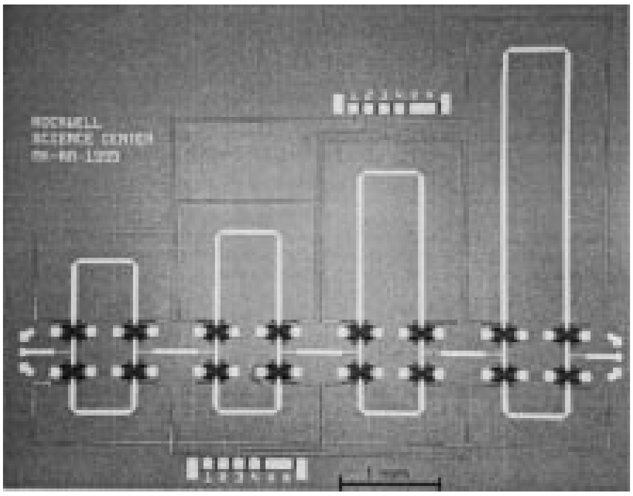

Figure 1.6: Photograph of a4-bit true time delay network realised using 16 RF MEMS switches [20].

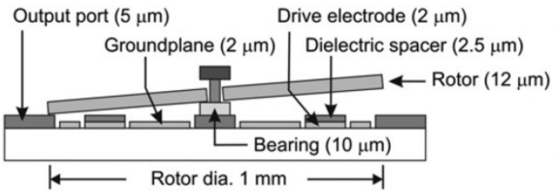

(a)

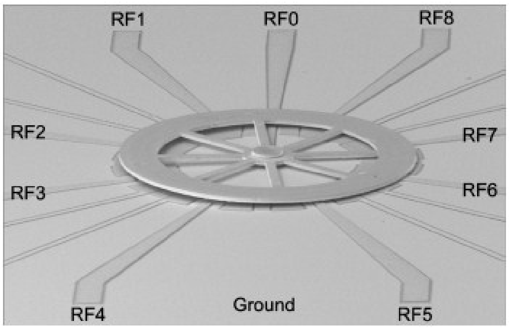

(b)

Figure 1.7: (a) Cross-sectional illustration of the SP8T rotary switch, and (b) SEM micrograph of the fully assembled switch [18].

With the second category, many RF MEMS variable capacitors have been demonstrated in the open literature having capacitance ratios of 20 or higher [21], [22]. Several possible structures have been implemented to achieve variable capacitors, most commonly based on out-of-plane separation distance (or gap) with a parallel-plate capacitor or displacing the fingers of an interdigitated capacitor, thereby changing the in-plane separation distance [23], [24]. Examples of these variable capacitors are shown in Figure 1.8(a) and (b), respectively.

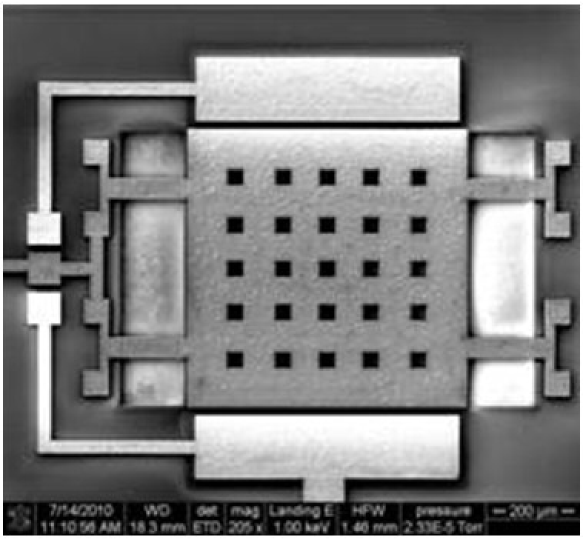

(a)

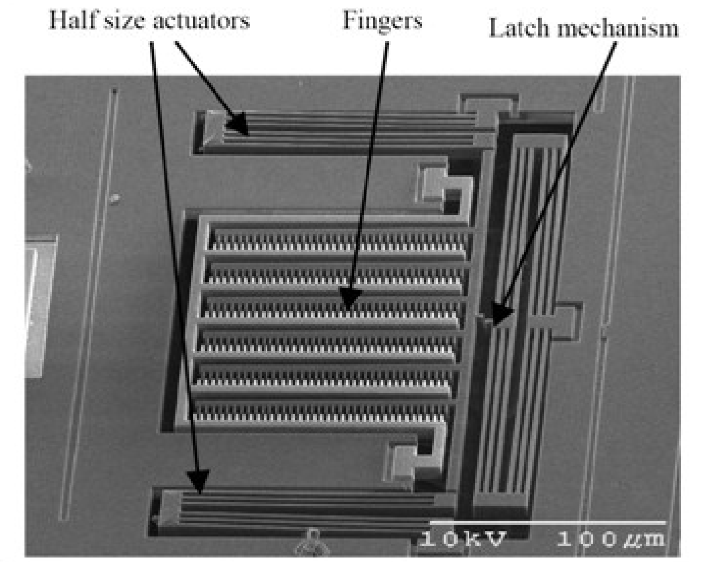

(b)

Figure 1.8: SEM micrograph (a) of a parallel-plate tuneable capacitor [22], and (b) of an interdigitated tunable capacitor [24].

Similarly, for inductors, displacement of the coils would change the coupling between them and, therefore, the value of the overall inductance [25]–[27]. An example of a tuneable inductor is shown in Figure 1.9.

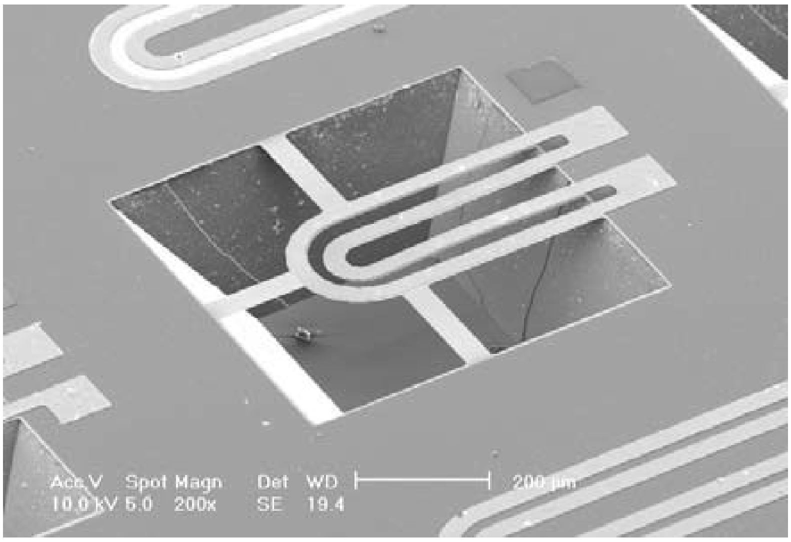

Figure 1.9: SEM micrograph of a variable inductor. The inner coil can move downwards via thermal actuation [26].

1.3.3 MEMS fabrication methods

MEMS are commonly associated with semiconductors and, therefore, to silicon micromachining processes. Silicon micromachining and MEMS fabrication are undertaken within a cleanroom and are made through a sequence of processes, the most relevant among all of them are: lithography, deposition, oxidation and etching [28]. Lithography is the step for the definition of patterns and is based on the spin-coating, exposure and development of photosensitive polymers, usually called photoresist. Selective exposure is obtained by aligning a mask on the substrate and illuminating with UV light. The pattern obtained would act as a protection layer for the following processes, allowing selective addition or removal of material. Several materials can be deposited, according to needs, but most frequently a metal layer is needed for conductive tracks and pads. Metals can be deposited by evaporation or sputtering and the most common ones are aluminium and gold. Deposition by evaporation is obtained by heating or bombarding with an electron beam a target of the required metal. Deposition by sputtering is achieved by bombarding the metal target with heavy ions (i.e. argon), which will liberate the atoms, which will uniformly deposit on the substrate. These methods are defined as physical vapour deposition (PVD).

In contrast, chemical vapour deposition (CVD) methods involve a chemical reaction to form the desired layer. Among these, oxidation is one of the most important. This is used to grow a thin film of silicon oxide and is obtained by heating the substrate in oxygen rich atmospheric steam.

Finally, etching is the process used to remove material. It can be achieved through the use of liquid etchants (wet etching) or plasma (dry etching). Etching is also classified as isotropic or anisotropic. Plasma anisotropic etching techniques like reactive ion etching (RIE) and deep reactive ion etching (DRIE) are the most common for silicon micromachining, enabling the fabrication of high aspect ratio trenches with very good wall verticality. The previous summary of microfabrication processing steps is by no means exhaustive, but highlights the complexity and, by extension, the costs associated in manpower, consumables and infrastructure.

MEMS are usually based on suspended or free-moving structures. These can be achieved by using sacrificial materials that can be removed to release the suspended element (e.g. a cantilever), or by assembly of a previously formed component (e.g. gears on an axel). Materials that can be removed with high selectivity are generally used as sacrificial layers and include photoresist and SiO_2, which can be removed by organic solvents or hydrofluoric acid (HF), respectively. For the assembly, parts are often electroformed or produced with a

LIGA (Lithographie, Galvanoformung, Abformung – Lithography, Electroplating, and Moulding) process and then released. Alternatively, these two possibilities can be combined to obtain a self-assembling device, where the movement for the assembly is obtained by the released built-in stress [29] or the surface tension [30], [31].

1.4 LTCC

Ceramic microelectronic devices, where the entire substrate and any conductive, resistive and dielectric materials are fired in a furnace at the same time, are generally referred to as co-fired ceramic devices. Typical components integrated in co-fired ceramic devices include capacitors, inductors and resistors, printed using thick-film technology. Ceramic substrates and similar processing technology are used in multi-layer packaging for MEMS, microprocessors and RF applications. They are also employed for harsh environments or when there is a need for good heat dissipation.

Co-fired ceramics belongs to the greater branch of laminate technology, which includes other technologies, such as liquid crystal polymer (LCP). Indeed, the production process involves a number of layers independently fabricated and assembled through lamination into a single component as the final step. This differs from semiconductor device fabrication, where layers are processed sequentially, each new layer is created on top of the previous one.

Co-fired ceramic technology can be divided in two categories: LTCC and high temperature co-fired ceramic (HTCC). As the name suggests, the main difference is in the firing temperature that is lower than 1000°C for LTCC and generally around 1600°C for HTCC. This difference is due to the composition of the substrate material. While HTCC is generally composed by pure alumina (Al_2O_3), LTCC is mostly a mixture of alumina and glass, whose composition changes substantially between manufacturers. The processing steps involved in both LTCC and HTCC are very similar; however, the higher firing temperature of the latter limits the choice of metals suitable for the printing of conductors. Indeed, suitable metals need to have a melting point higher than the firing temperature and only refractory metals like tungsten or molybdenum alloys can be used for such applications. Therefore, the advantage of LTCC over HTCC, apart from the less demanding firing process, is the possibility to use high conductivity metals, such as copper, silver or gold, for its conductive layer.

The technique of deposition of conductive materials, as well as resistive or dielectric ones, for ceramic substrates is defined as thick-film technology. It is important to appreciate this point, before considering LTCC processing further.

1.4.1 Thick-film Technology

The deposition of thick layers (usually more than 15 μm) of materials on a substrate using screen or stencil printing is commonly defined as thick-film technology. This technology is defined "thick" in contrast to what is known as thin-film technology. These two categories of deposition can be characterised by the minimum layer thickness achievable and usually belong to very different manufacturing fields. Examples of thin-film depositions are chemical or CVD, PVD and spin coating. These are generally associated with semiconductor processing, together with a lithography step for patterning. Thick-film technology is normally associated with printed circuit boards (PCB), flexible substrates and multilayer systems in general (e.g. LTCC, HTCC, LCP) and does not need any extra process for patterning. Recent improvements in thick-film technology have spread its application to areas that include solar cells for the fabrication of the conducting tracks, as it offers a fast method for patterning large areas.

As previously described, two possible options for thick-film depositions are available: screen printing and stencil printing. Screen printing consists in a woven mesh screen with a patterned emulsion to reproduce the desired shapes on a substrate.

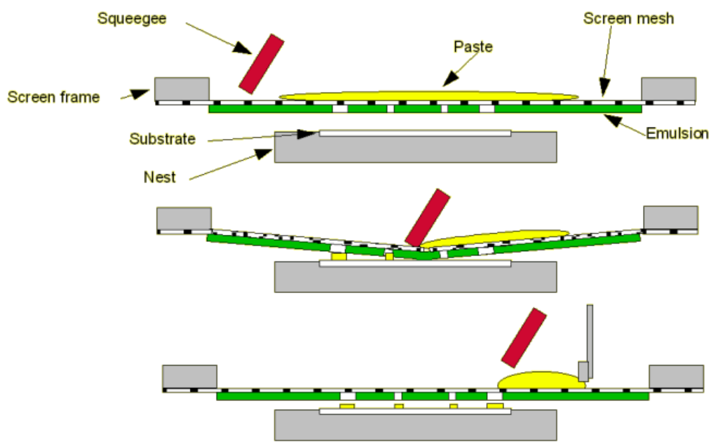

Figure 1.10: Screen printing process [32]

As illustrated in Figure 1.10, the patterned mesh is aligned and placed above the substrate, which is held in place by a vacuum chuck. With a squeegee, the ink or paste is pushed through the mesh openings and deposited on the substrate, transferring the pattern onto it. During this process, the characteristics of the printed pattern, such as thickness, uniformity and minimum feature size, depend on many factors. These include the paste rheology, the gauge, openings and material of the mesh wire, and the openings and the thickness of the emulsion that defines the pattern on the screen. An example is shown in Figure 1.11. Other influencing factors include the squeegee material, angle, speed and pressure. Great expertise is required to achieve good quality repeatable results.

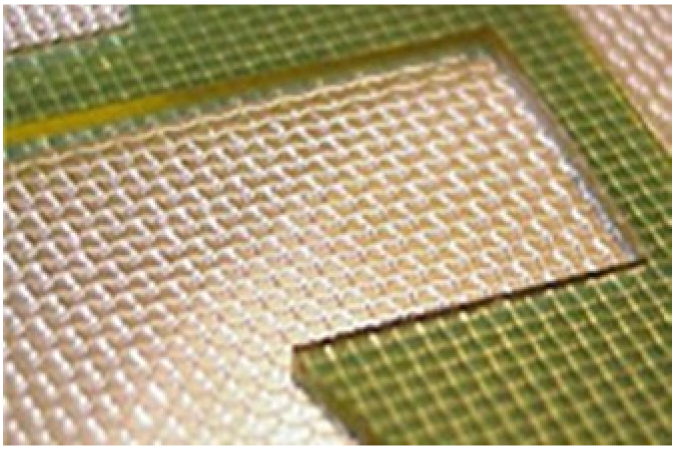

Figure 1.11: Detail of mesh and emulsion for screen printing [33].

Different to screen printing, with stencil printing a solid stencil is used, generally made of stainless steel. An example is shown in Figure 1.12. This technique is particularly suitable for high viscosity pastes (e.g. solder paste), but causes some limitations on the geometries. While with screens it is possible to reproduce almost any shape or pattern, stencils cannot be used for hollow geometries (e.g. rings), otherwise the internal pattern cannot be supported. Stencil printing is defined as "on-contact" printing, in contrast with screen printing, which is defined as "off-contact". Indeed, it can be noticed from Figure 1.10 that the screen is held at a distance above the substrate and pushed in contact by the squeegee; while for stencil printing, the stencil is directly placed in contact with the substrate and lifted only at the end of the swipe.

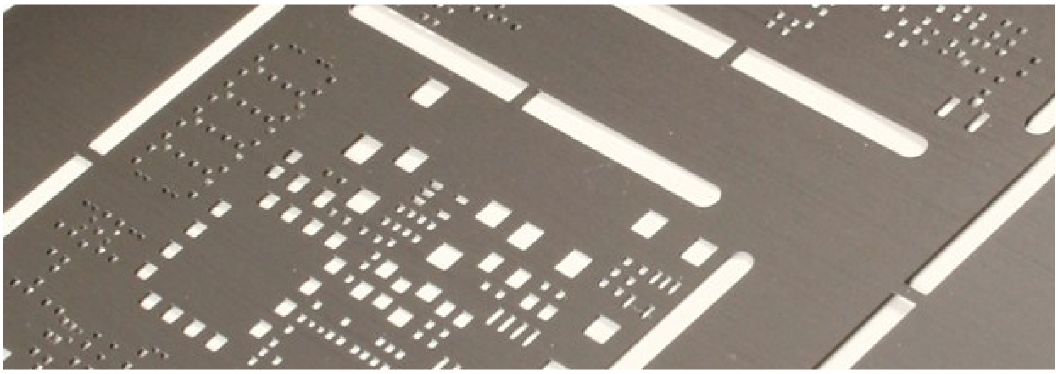

Figure 1.12: Stainless steel stencil for solder paste [33].

The speed and large printing areas achievable with these technologies represents a very important advantage. It allows the deposition of many kinds of materials, such as high-conductivity metals pastes, resistive inks and low-loss dielectrics, which are essential for RF applications. Others materials include sacrificial material pastes, fundamental for the realization of suspended structures, and piezoelectric material pastes [34]. More generally, any material that can be suspended in a paste, including organic compounds, can be printed with these technologies.

In the past few years, many important advances have been made, such as photoimageable low-loss dielectrics or conductor pastes (gold and silver) [35], or ultra-fine screen meshes able to achieve feature size as small as 20 μm [36]. These advances in technology enabled the manufacturing of structures usually associated with thin-film processing, with a substantially lower cost and higher throughput, due to the large area and speed of this printing process.

1.4.2 Standard LTCC manufacturing technology

LTCC technology: Standard processing steps

LTCC is made from a mixture of fine ceramic powders (mainly Al_2O_3), glass powder, and organic binders and plasticisers. This mixture is then tape cast into sheets, commonly referred to as "green body" or "green tape". All the processing relative to this technology is usually done on this green tape and, when complete, all the layers are precisely stacked, laminated and fired, as illustrated in Figure 2.

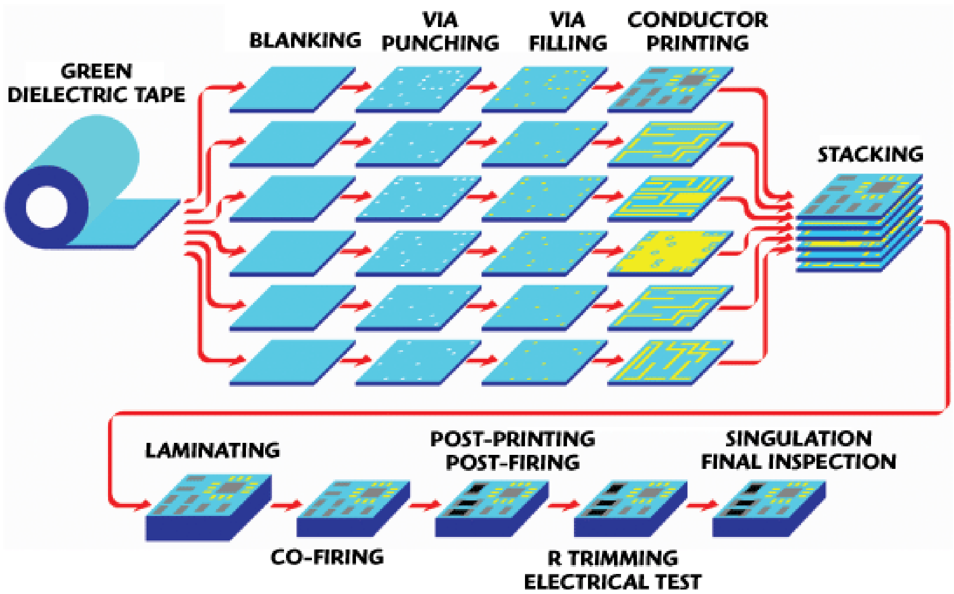

Figure 1.13: LTCC processing steps [37].

Pre-conditioning: Due to the presence of volatile solvents in the green body, during processing its dimensions will change due to natural shrinkage. To avoid shrinkage, before processing, each layer is set to rest in an oven, so that part of the solvents evaporate and the material is mechanically more stable, allowing tighter tolerances at final product.

Via machining: In any multilayer circuit, connections are needed between layers. There are mainly two ways of drilling holes in this technology: punching and laser drilling. Punching consists in forcing a cylindrical pin through the LTCC layer, creating a hole. This technique allows high precision for the via diameter and wall verticality, but is relatively slow and the pin wears out rapidly, due to the high concentration of hard ceramic particles in the substrate. In contrast, laser machining offers better performance in speed, flexibility and has a lower running costs. However, there is compromise on the quality of the via.

Via filling and screen printing: After all the vias are ready they are filled with conductive paste and the required pattern is printed on the substrate. For both these steps, screen printing represents a viable solution, but different pastes are required for these two purposes. After printing, the paste is left drying in an oven. It is particularly important that the pastes used are well matched with the substrate, so that during the firing process their shrinkages are similar. This helps prevent warpage and distortion or even delamination.

Stacking: To realise a multilayer circuit, all the layers, after having been printed and checked free of defects, need to be precisely stacked. This can be done manually, using a jig and fiducial holes or through automated equipment that optically recognise fiducial patterns and aligns the layers. A precise alignment between layers is fundamental to achieve good inter-layer interconnects.

Lamination: The lamination process is particularly important and is a fundamental step for the achievement of good tolerances in the final product; as the shrinkage uniformity during the firing process depends on it. In this process both pressure and heat have to be applied and a hot uniaxial press or hot isostatic press can be used. The application of pressure only in one direction with a uniaxial press would lead to spatially non-uniform shrinkage (i.e. only planar uniform). Nevertheless, this is a widely adopted solution, as it is faster, more cost effective and able to handle large substrates. With an isostatic press, the multi-layer substrate is vacuum sealed in an antistatic plastic bag and positioned in a sealed, high pressure chamber filled with liquid (e.g. water or oil). The liquid is then heated to the required temperature and pressure applied. Due to the uniformity of the process, better overall tolerances are obtained using an isostatic press [38].

Firing: In the following step of the process, the laminated substrates need to be fired within a furnace, so that the layers will sinter into a single block. Even though the main component of LTCC is alumina, which sinters at 1500-1700ºC, the presence of glass and other minerals, such as lanthanides, enables a ceramic body to form at much lower temperatures (850-900°C). The firing profile is specific to the LTCC composition and suggested by the manufacturer. However, when introducing non-standard layers, like graphite-based sacrificial materials, the firing profile has to be adapted to take into account their burnout [39].

Port-process printing: In some cases, more processing is required to improve integration with other components (e.g. interconnects). For this purpose more printing might be needed on the top layer. Always achieved via screen printing, the pastes used in this case generally require a further firing process and are designed to have good solderability. If needed, post-firing pastes for the brazing of metal cases on the ceramic substrate are also available.

Laser trimming: Screen-printed components, such as resistors and capacitors, can have relatively high tolerances, up to 15% for commercial processes. If accessible, whether on the top layer or through a purposely designed cut-out, the values of these components can be adjusted to tolerances of 5% or lower. This is achieved through laser trimming of these components. During this process a laser removes part of the printed material, while the value of the component is probed, and stops when it reaches the desired value. In industrial manufacturing, where patterns of the printed parts are well known and defined, this process can be fully automatized. In some cases, when the full system behaviour needs to be carefully calibrated, the trimming process can be performed while an input signal is applied and the output measured.

Other LTCC related processes

Pressure assisted sintering: One of the main disadvantages of LTCC technology is shrinkage during the firing step. This shrinkage is generally of the order of 10% in the planar *x-y* direction and of 12% in the out-of-plane *z* direction (i.e. perpendicular to the layers). *A priori* design compensation is often not a suitable solution, as this shrinkage may have significant variations and non-uniformities, as it depends on the geometry of the printed pattern and the lamination technique used. To overcome these issues, several solutions have been proposed. One of them is the application of pressure to the laminated piece during the firing process. This technique is defined as pressure assisted sintering (PAS) and involves the use of very expensive specially built furnaces [40]. The application of pressure constrains the shrinkage only in the *z* direction, which would therefore increase, with the result of leaving the features of the printed pattern unaffected. This procedure also improves the flatness of the final substrate.

Pressure-less assisted sintering: A less expensive alternative to the PAS is pressure-less assisted sintering (PLAS). Similarly to the previous technique, it is based on constraining the shrinkage in the *z* direction, but via the lamination of additional layers that would not undergo shrinkage during the firing, at both ends of the stack [41]. These additional layers are referred as low temperature transfer tape (LTTT). The structure is then fired in a furnace, as in the standard process. The disadvantage of this process is that these additional layers need to be mechanically removed with techniques such as sand-blasting or waterjet [40]. Based on the same principle, Heraeus™ developed a series of zero-shrinkage tapes (Heralock HL800 and HL2000), formed by the sandwiching a non-shrinking layer between of two LTCC layers [42]. This kind of tape is substantially more expensive and needs specially formulated proprietary pastes to match its composition and reduced shrinkage.

Sacrificial pastes: The use of sacrificial materials is fundamental for the realisation of suspended structure and cavities. Birol *et al.* [43]–[45] have shown two possible sacrificial pastes, based on mineral composites (i.e. MgO and CaB_2O_4) and on graphite. The formers offer a support during the whole firing process, but needs to be removed via chemical etching and their shrinkage during firing needs to be well matched with the substrate used. The latter outgases during the firing process at temperature lower than the sintering one, and is therefore suitable as a support for cavities. As highlighted earlier, the firing profile needs to be carefully calibrated to obtain good results, in particular for cavities. The gasification of the graphite-based sacrificial layer needs to happen before full sintering of the ceramic substrate, which start at temperatures around 750°C; gasses produced need to be able to escape through the porous layers [39]. Graphite proves to be a suitable material for this purpose, as it oxidises at temperatures between 600°C and 720°C. The firing profile will, therefore, need an extended dwell time at 720°C to fully remove all the graphite. However, at this temperature, the LTCC is very fragile with the particles essentially held together by weak surface forces, and an excessively long firing time at 720°C may cause the cavity roof to sink, as shown in Figure 1.14.

(a) (b)

Figure 1.14: Graphite filled cavities after firing. With the sample on the left the firing profile did not have a prolonged dwell at 720°C; while with the sample on the right the dwell time was excessively long [39].

1.4.3 RF Applications of LTCC

FR4 has been the material of choice for many RF circuit substrates, due to ease of processing, identical to PCB processing and its relatively very low cost. However, when low losses or frequencies higher than a few GHz are needed, FR4 is no longer suitable. Rogers™ and Taconic™ offer alternative substrate materials that can be used at higher frequencies, but, even though the manufacturing cost is similar to FR4, the costs increase dramatically. LTCC offers better properties, both electrically (higher dielectric constant and lower losses at frequencies >60

GHz) and mechanically (ease of lamination for multilayer and robustness). Although the equipment needed for its processing is more expensive, the cost of processing and of consumables is lower and, if a large scale production is considered, LTCC can be effectively considered a viable option for large-scale production of RF circuit boards.

LTCC has been of great academic interest in the microwave and millimetre-wave field in the past decades, due to its excellent properties and lower processing costs, when compared to semiconductor and HTCC technologies. Its ease of layering enabled the creation of complex circuits, leading to low-loss microwave modules. In industry, LTCC is still very popular for the production of compact RF integrated modules. This is mainly due to several factors: the TCE of LTCC is very similar to silicon or GaAs and this enables easy integration of active elements at chip level; LTCC is a well-known technology for interconnects and packaging. These factors improve integration, and the high level of robustness of the final module makes it suitable for harsh environments, from automotive and aerospace (e.g. electronics near engines) to the oil and gas industries [46]–[48].

1.4.4 Substrate integrated circuits

Low-cost, high-yield microwave and millimetre-wave technologies are fundamental for the development of RF systems. One of the main challenges is the design of low-loss, high-Q structures in planar technology, as these components are usually associated with metal-pipe waveguides. The development of substrate integrated waveguides (SIW) aims to fill the performance gap between planar microwave circuits and metal-pipe waveguides [49]. The combination of planar and non-planar structures with active components leads to the development of hybrid systems, whose level of integration and performance grows significantly if combined with multilayering. LTCC, again, seems to be a suitable material for SIW and several research groups demonstrated the feasibility of non-radiating dielectric waveguides integrated within the substrate. Most of these structures have been realised using vias to define the side walls of the waveguide (sometimes referred to as a picket fence waveguide) [50]; the possibility of developing air-filled cavities in LTCC clearly opens up new opportunities for developing higher performing structures. Examples of the SIW technology in LTCC have been reported, with results comparable to standard rectangular waveguides in Ka-band (26.5 – 40 GHz) [51], [52].

1.4.5 MEMS and LTCC

In industry, LTCC is a well-known technology for RF module and packaging applications. In the area of MEMS and micromachining, work on LTCC is in its infancy. With laser prototyping of microwave and millimetre-wave circuits on LTCC, by Robertson *et al.* [50], [53], a number of research teams worldwide have started studying the fabrication of actual MEMS components in LTCC technology. For example, Newborn *et al.* have shown that an electrostatically-actuated leaf spring vertical actuator could be realized in LTCC technology. Here, sacrificial layers are designed to burn off during firing [54]. Birol *et al.* demonstrated that microfluidic devices could be fabricated in LTCC by employing the sacrificial carbon layer method [43]–[45]. The Georgia Tech group, widely known for its System-on-Package work, has reported a wireless pressure sensor in LTCC, employing a cavity and membrane technique [55]. Reported works have included using laser machining and the fabrication of LTCC cavities using hot embossing and silicon micro moulds [56]. Sedaghat-Pisheh *et al.* demonstrated the fabrication of a conical spiral antenna using a sacrificial layer technique and chemical etching [57].

1.5 Laser micro-machining

The use of lasers for material removal was first introduced as an alternative to standard machining, for cutting particularly hard materials. This technique had the clear advantage of not being subject to tool wear and, therefore, proved to be a suitable and commercially valid alternative for cutting and drilling materials such as hardened steel, ceramics and diamond. Moreover, laser cutting offered further advantages when high precision is required. The focused laser beam offers very narrow and clean cuts and allows the production of particularly small components.

Laser cutting is based on the ablation of the material hit by the laser beam. The high pulse energy concentrated in the focal spot causes the material to heat to the point of sublimation, thereby leaving a hole. The heat generated in the process is highly localised and generally does not affect surrounding areas, making it suitable for delicate materials or for the introduction of highly localised stress, for applications such as laser bending [58], [59].

Many kinds of laser are available, with wavelengths ranging from infrared (IR) to ultraviolet (UV) and recently also X-ray, working with different principles (i.e. solid state, gas, fibre, dye or semiconductor). Lasers can be divided into two categories: pulsed and continuous wave. Pulsed lasers are able to deliver a very high amount of energy per pulse in a very short amount of time, ranging from few tens of nanoseconds to femtoseconds. With recent developments, laser technology has become widely available at relatively low cost and has found many more applications, from marking/engraving to micromachining or even propulsion [60], [61].

Laser micromachining, in particular, has found particular interest in the manufacturing of high precision devices. Laser ablation for micromachining is usually obtained through two procedures: scanning and projection. In scanner-based laser machining systems, the laser beam is moved on the substrate using mirrors. After the scanning mirrors a lens system is used to focus the beam onto the working plane. A normal convex (focusing) lens receiving a beam of collimated light at an angle from a laser would have a concave focal surface. This condition would not allow uniform processing of the material in the scanner field of reach. Therefore, a telecentric *f-theta* lens is used to overcome the issue. This type of lens, which is actually composed by 3 or more lenses, takes its name from its property of having a variable focal length *f* linearly depending on the angle of incidence *theta*; allowing a flat focal plane. An example of the lenses used for scanning is illustrated in Figure 1.15.

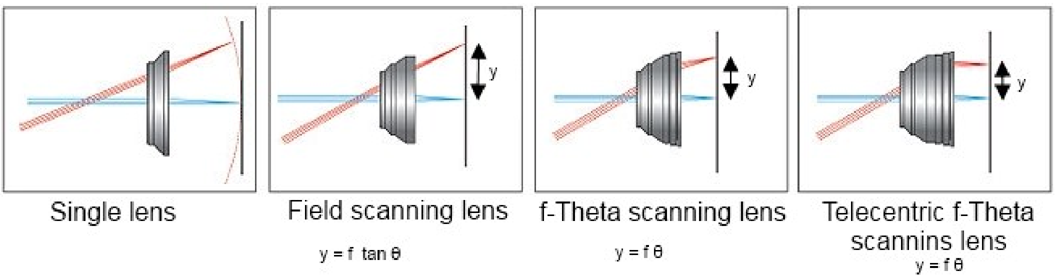

Figure 1.15: Possible alternatives for focusing a scanned beam.

In a projection laser system, the laser beam is expanded and homogenised (its fluence made constant over its cross section), shaped through an aperture, patterned through a mask and eventually the image is scaled down by a projection lens. The outcome is a machined pattern reproducing the image on the mask, but with features much smaller than the initial ones, depending on the projection lens magnification.

While the first system described offers greater flexibility, due to the lack of masks, the second allows for smaller features and higher precision, at a cost of a reduced working area (usually one to few millimetres squared). Moreover, due to the larger area illuminated, the pulse energy needed in a projection system is much higher (approximately one order of magnitude), in order to obtain sufficient fluence and ablation.

Lasers have recently found applications in the semiconductor industry for via drilling and wafer dicing, particularly with thin wafers. For similar applications, innovative high performance techniques like water jet-guided [62] and stealth cutting [63] offer low damage, low debris solutions for dicing. In the open literature few examples are available for the use of laser micromachining for purposes other than dicing, with one of the most interesting applications being the trimming and tuning of MEMS accelerometers proof mass [64].

1.6 Conclusions from the literature review

1.6.1 3D Printing

3D printing technology has recently received great attention from many fields of research and manufacturing. Its ability to easily create geometrically complex shapes, its flexibility in production and the eventual cost savings make this technology a very important tool for the development of new products and services. Since its first development in the late 1980s, with the first stereolithographic apparatus, 3D printing has mainly been applied only for the development of artistic items and non-functional models. This led to a strong limitation in the materials available and it is only recently possible to find materials with different properties. Nevertheless, until now little-to-no functional material (i.e. conductive or mineral loaded) is commercially available. The opportunities offered by this technology are still to be discovered, but its potential appears evident.

1.6.2 LTCC

LTCC is a widely applied technology, in many fields, but its most relevant field of use is as a substrate for RF circuits. For this application it is a very competitive technology, compared to alternatives available on the market. The reasons for its success can be summarised in a few significant points. The very good properties at microwave frequencies, the ease of manufacturing of complex multilayer circuits and integration of active components on a chip scale contribute towards high levels of integrations. Moreover, the low cost for the consumables and the manufacturing process make this material suitable for large scale production.

Nevertheless, there has been little advancement since LTCC technology was first widely adopted for commercial manufacturing over the past two decades. For integrating waveguides and cavities in LTCC, it appears obvious that there is still great potential for this substrate material to support an enabling technology for higher performance integrated microwave circuits. This opportunity can reopen the interest in research in LTCC technology, but may not be enough to drive a significant step-change in commercial RF systems.

The following step is the integration of active elements, aiming to complete a SoS. Although some devices and circuits (e.g. amplifiers) cannot be realised in any other technology apart from semiconductor (e.g. GaAs and SiGe), it is feasible to imagine that other components can be integrated into standard LTCC processing to achieve tuneable or reconfigurable systems. In particular, such functionalities can be achieved by RF MEMS, for which LTCC represents not only a suitable substrate for RF signals, but also one of the best packaging materials.

1.7 Hypothesis and aims

The general hypothesis of this thesis is that commercially viable devices should not be manufactured using expensive processes and that sensible alternatives can be found that would achieve similar functionalities with only a minor compromise in the performance. In modern society, where technology plays a dominant role in everyday life and the global economy, there is a drive for lowering costs. The development of new processes based on well-known low-cost technologies or on other emerging ones can open-up new possibilities and opportunities. LTCC is a well-known low-cost and high-performance technology and the integration of other components without introducing further complexity to the manufacturing process represents an important tool in the development of novel integrated devices and system-on-packages. The rational underlying this part of the work is that RF MEMS can be integrated onto an LTCC substrate, with only modest extra process complexity. The main aim is to evaluate some of the possible structures that can be realised to achieve RF functionalities, such as switches and variable capacitors. The design of these integrated devices will be based on maintaining compatibility with standard LTCC processing, on the requirements for large-scale manufacturing and eventually on containing costs.

3D printing is a developing technology showing great potential. The constantly growing number of materials available, together with the shape complexity easily achievable, indicates the great flexibility that this technology offers, whether for prototyping or small-volume bespoke manufacturing. The aim of this part of the work is to prove the feasibility of 3D printing as a manufacturing technology for bespoke lightweight waveguide passive components, reducing costs and production time. The work reported in this thesis aims to prove the feasibility of the above mentioned concepts and to show enabling technologies and processes for the development of high performance devices.

1.8 Outline of the thesis

1.8.1 3D Printing

Chapter 2

In the second chapter of this thesis, an alternative production process based on two different 3D printing technologies (fused deposition modelling and stereolithography) will be proposed for the manufacture of metal-pipe waveguides. The 3D printing fabrication and RF characterisation of X-band and W-band metal-pipe rectangular waveguides will be covered. An inductive iris filter in W-band is also demonstrated.

Chapter 3

In the third chapter a fully 3D printed dielectric flap phase shifter presented and is applied in the design and fabrication of a 4-element phased antenna array is reported. All the components of the antenna, including all the feed lines and junctions, are 3D printed.

1.8.2 LTCC

Chapter 4

In the fourth chapter laser micromachining of LTCC in its green state is studied for the manufacturing of suspended structures. LTCC bulk laser micromachining is used to define new structures and geometries that, via trimming, cutting and lamination, can generate suspended 3D structures. Equally relevant for this purpose is the study of sacrificial layers and a novel composition for a graphite-based sacrificial paste will be proposed. Eventually, the suspended structures and its fabrication process will be demonstrated.

Chapter 5

In chapter five a second approach to the fabrication of suspended cantilevers is proposed, based on a hybrid structure which combines standard LTCC processing and metal foil. Aluminium foils are readily available commercially in a variety of well-controlled thicknesses. This material offer the characteristics needed for the development of effective, easily actuatable cantilevers. Two possible structures were investigated, using laser bending and photoimageable polymer thin films. Their design, fabrication and performance will be demonstrated.

This part of the work was conducted via an inter-university collaboration based on a joint project between Imperial College London, the University of Leeds and the University of Loughborough.

Chapter 6

In the sixth chapter an analytical study of cantilever structures, based on their mechanical and electrostatic actuation properties is also proposed. The limits of general textbook equations will be highlighted and a different, more accurate approach, will be proposed with an alternative set of equations valid for a wider range of cases.

1.8.3 Laser micromachining of silicon

Chapter 7

In the seventh and last chapter of this thesis the laser micromachining of silicon is studied, to obtain high aspect ratio beams. In particular, a statistical study will be undertaken to optimise the laser parameters and machining strategy to achieve high quality beams. Such beams are then used to develop folded suspensions and a laser micromachined micro-gripper will be demonstrated.

CHAPTER 2: 3D PRINTED METAL-PIPE RECTANGULAR WAVEGUIDES

The following chapter is based on the paper:

"**3-D printed metal-pipe rectangular waveguides**," by D'Auria, M., Otter, W.J., Hazell, J., Gillatt, B.T.W., Long-Collins, C., Ridler, N.M., and Lucyszyn, S., published on *IEEE Transactions on Components, Packaging and Manufacturing Technology (CPMT)*, vol. 5, no. 9, pp.1339-1349, September 2015.

The relatively very low loss characteristics of conventional metal-pipe rectangular waveguides (MPRWGs), compared to planar transmission lines (e.g., coplanar waveguide or microstrip), make this technology essential for applications where dissipative attenuation is a critical factor. The manufacturing cost for complex 3D structures represents a limitation for low cost applications; this is exacerbated when frequency increases into the millimetre-wave band, due to the more demanding requirements in mechanical precision for smaller feature sizes. For this reason, alternative enabling technologies have been explored for their manufacture. For example, for monolithic microwave integrated circuits, surface micromachined dielectric-filled MPRWGs were demonstrated [1] and [2] in W-band (75 to 110 GHz) at 105 GHz. This concept was then adapted to low-cost thick-film processing on ceramic substrates and demonstrated from 60 to 90 GHz [67]. A more recent innovation that readily supports tunable components and reconfigurable architectures employs the use of 2D and 3D metamaterials (holey metal surface and wire media, respectively) with demonstrators at X-band (8 to 12

GHz) [68]. Advanced reconfigurable substrate integrated waveguide architectures for terahertz applications was proposed in [69], with the use of *virtual* sidewalls within high-resistivity silicon wafers, patterned by programmable laser light sources. Unfortunately, these alternative manufacturing technologies can result in much higher dissipative losses.

Alternative techniques for the constructions of waveguides are based on lamination technology for the development of substrate integrated waveguides (SIW). An early example of laminated SIW in glass ceramic (LTCC) is proposed in [70].With this glass ceramic-filled rectangular waveguides the horizontal wall metallization is obtained via screen printing and the vertical ones by metal filled via holes (picket fence wall) and has a reported attenuation of 40 dB/m in W-band. With thick-film technology, in [71] photoimageable paste is used to define the internal geometry of SIW in V and W-band, with reported attenuation of 100 dB/m and 200 dB/m, respectively. More recently picket fence SIW on polyethylene terephthalate (PET) substrate was demonstrated in [72] with an attenuation of 700 dB/m at 5 GHz. With all these proposed solutions, however, the losses are very high and can be associated with the material filling the waveguide. Lower losses can be obtained when the SIW is air filled, such as the one proposed in [73]. Such waveguides, fabricated using Rogers RT/Duroid 6002 substrate and picket fence vertical walls, shows an attenuation of 45 dB/m at 30 GHz.

Commercial MPRWGs are traditionally manufactured by reshaping (drawing) metal pipes through rectangular dies or from machining by either computerized numerically controlled (CNC) milling or electronic discharge machining (EDM) with spark erosion. For convenience, these will be classified as machining technologies. A state-of-the-art CNC machined split-block WR-10 band (75-110 GHz) thru line in aluminium was reported with an average attenuation of 4-dB/m across W-band [74]. Chemically polished copper EDM WR-10 waveguides have also been measured with the same level of attenuation [75].

In contrast, micromaching technologies can include bulk micromachining of silicon [76]–[80] and surface micromachining of dielectrics [65], [66] or photoresist layers [81]–[90]. Silicon micromachined MPRWGs are of particular interest for (sub-)millimetre wave frequencies. For example, a gold-plated WR-10 waveguide has a reported measured attenuation of 0.05 dB/λ_g at 100 GHz [76]. A similarly WR-1.5 band (500-750 GHz) waveguide was recently reported with attenuation of ~ 80 dB/m at 600 GHz [80].

The pioneering work, reported in [81] demonstrated the use of X-ray photoresist lithography for the manufacturing of waveguides for terahertz applications. The following year, this concept was developed further by Collins *et al.* with standard photolithography using SU-8 photoresist as the sacrificial building material for the manufacture of air-filled waveguides and slotted *H*-plane sectoral horn antennas in W-band, G-band (140-220 GHz) and at 1.6 THz [14]–[17]. This work was undertaken within the U.K.'s EPSRC-funded research program Terahertz Integrated Technology Initiative (TINTIN). It is also interesting to note that the TINTIN consortium first reported the concept of SU-8 formed split-block waveguides, using their snap-together techniques, demonstrating a loss of ~ 0.5 dB/λ_g at W-band [15]. More recently, Smith *et al.* [86] demonstrated WR-3.4 band (220-330 GHz) split-block waveguides and cylindrical cavities. The most recently reported work on SU-8 formed split-block waveguides, from the University of Birmingham (U.K.), also showed impressive results at 60 GHz [87], 280 GHz [88], [89] and 650 GHz [90].

Machining and micromachining technologies are relatively expensive manufacturing solutions. A low cost alternative for the manufacture of MPRWGs is to use micro moulding (which include injection moulding and hot embossing), followed by a traditional metal plating process. WR-10 gold electroplated plastic waveguides [91] and filters [92] have been reported. The former demonstrated a worst-case return loss of 14 dB across W-band and minimum attenuation of 0.116 dB/λ_g (or 27.6 dB/m) at 92.5 GHz [91]. The associated 5^{th}-order inductive iris filter demonstrated a worst-case pass-band return loss of 12 dB and attenuation of 3.49 dB at 95.4 GHz [92].

Over the past two decades, 3D printing (also known as additive manufacturing) has found widespread applications in rapid prototyping and manufacturing of high geometrical complexity components. Academic interest in microwave and millimetre-wave research began at the University of Michigan Ann Arbor in 2002, with the development of metamaterials and electromagnetic bandgap (EBG) structures in ceramics, by either coextrusion or casting in stereolithographically made moulds. This research was led by Chappell and Katehi [93]–[95]. In 2004, they then went on to investigate microwave passive components (e.g., cylindrical and rectangular air-filled cavity resonators, and nonplanar helical and monopole antennas) and coupled-cavity resonator filters [11], [96], [97]. This pioneering work on stereolithography included K_u-band (12 to 18 GHz) horn antennas in 2005 [10].

In 2006 Sarabandi *et al.* used ceramic stereolithography to develop dielectric antennas [98]–[100] and photonic crystal waveguides [101], [102]. At the same time, within Europe, XLIM–UMR CNRS at the University of Limoges used ceramic (micro)stereolithography for the fabrication of microwave filters, antennas, and millimetre-wave EBG crystals [9], [103]–[106].

Over the past 8 years, further examples of 3D printed microwave and millimetre-wave components have been reported: 1) metamaterials [7], [8], [107]; 2) corrugated and dielectric-filled horn antennas [108], [109]; 3) patch antennas [110], [111]; 4) graded index and Luneburg lenses [12], [13]; 5) frequency selective surfaces [112]. At terahertz (THz) frequencies, EBG structures, plasmonic and hollow core wire waveguides, and dielectric reflectarray antennas [14]–[16], [113], [114].

Apart from the early examples, by Chappell's group in 2004 and 2005, of 3D printed air-filled MPRWG components: e.g., cavity resonators [11], [96], [97], filters [97] and WR-62 band (12.4-18 GHz) pyramidal horn antennas [10], little has been reported in the open literature. Notable exceptions include a 35-39.5 GHz dielectric-filled horn antenna array in [108] and the W-band air-filled MPRWG (and circular waveguide corrugated horn antenna) in [109].

In 2012, the Swiss Federal Institute of Technology in Lausanne (EPFL) and its spin-off company (Swissto12) reported the 3D printing of passive structures for millimetre-wave and terahertz applications in their short note [115]. More recently, since 2014, Swissto12 have been advertising 3D printed metal-coated plastic (MCP) waveguides and diagonal pyramidal horn antennas [116], [117]. These air-filled MPRWGs operate in the WR-3.4 band and, with copper metallization, have a reported minimum attenuation of 12 dB/m at *ca.* 280 GHz. In addition, WR-5.1 band (140 to 220 GHz) MCP waveguides are also commercially available in both straight and with S-bend sections. In 2012, a 3D printed corrugated conical horn antenna in K_u-band was reported [118] and, more recently, a spherical resonator filter in X-band was demonstrated, with an average passband insertion loss of 0.107 dB [119].

With all the examples of 3D printing [7]–[16], [93]–[119], little detail is given on the metrology for determining performance. Moreover, to date, the lower cost 3D printing technology that exploits plastic extrusion techniques has not been reported for microwave rectangular waveguide applications. In this chapter, the 3D printing of X-band and W-band MPRWGs using plastic extrusion (thermoplastic deposition) and stereolithographic (UV resin curing) techniques, respectively, are compared and contrasted. In addition, a high performance W-band inductive iris bandpass filter is reported. All measurements are traceable to national standards in metal-pipe rectangular waveguide, performed by the U.K.'s National Physical Laboratory.

2.1 3D printing technologies and metallization

3D printing is based on layer-by-layer material deposition to realize arbitrary 3D objects. Different 3D printer technologies are commercially available. They can be classified into three main categories: 1) selective deposition of extruded material, which includes fused deposition modeling (FDM) [1]; 2) UV curing of resin, which includes inkjet printing and stereolithography apparatus (SLA) technology [2]; and 3) powder binding, which includes selective laser sintering (SLS) [3]. Within the scope of this chapter, the first two (specifically, FDM and SLA) will be considered further.

2.1.1 Fused deposition modelling technology

Injection moulding is by far the cheapest fabrication technology when high-volume manufacturing is required. However, the cost of the mould can be very expensive (thousands of dollars) and there are practical limitations on geometry for 3D structures. As an alternative for rapid manufacturing, there is increasing interest in FDM 3D printing; comparative case studies have been reported [120]–[124]. In general, since the cost per unit with 3D printing is relatively constant with volume, while the cost of injection moulding falls sharply, a break point in total manufacturing costs exists at low volumes. Moreover, 3D printing can be used to realize be-spoke components with highly complex geometries.

FDM printing is based on extrusion and selective deposition of thermoplastics. With this technology, the smallest achievable feature size on the horizontal *xy* plane is limited by the extrusion nozzle aperture; for example, having a typical diameter of 400 μm. Along the vertical build *z*-axis, feature size is limited by the minimum repeatable mechanical displacement; typically between 50 and 100 μm. As a result, the typical voxel size is of the order of 400 x 400 x 50 μm^3.

Solid objects are usually partially hollow, having a solid shell that defines the outer geometry and internal support scaffold for additional rigidity. The walls of the printed object will have visible scallops in the vertical direction; the extent of which is dependent on the chosen layer height. Scallops are caused by the melted thermoplastic assuming a circular shape. An illustration of FDM technology is shown in Figure 2.1.

(a) (b)

Figure 2.1: (a) Example of FDM technology's working principle. The plastic filament is pushed through a heated nozzle and the melted material is deposited [4]. (b) Cross section of an FDM 3D printed model showing the external shell and the infill.

2.1.2 Stereolithography apparatus technology

With SLA 3D printing, a photosensitive resin is contained within a tank. The top of the tank is scanned with a UV laser, which selectively cures the top layer of resin. The 3D printed object sits on a platform within the tank. After one layer has been cured, the platform is lowered and a fresh layer of resin is poured in front of the squeegee and levelled off by the squeegee; the whole process is then repeated. A schematic of an SLA equipment is shown in Figure 2.2 Finally, the part is rinsed of excess resin and then fully cured in a UV oven.

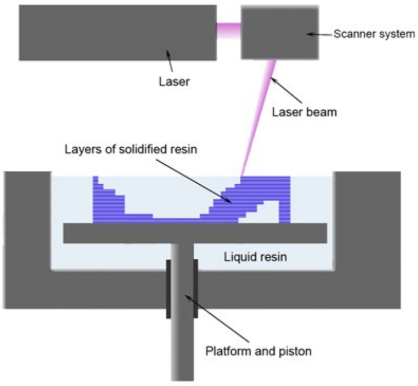

Figure 2.2: Example of SLA technology. The vat is filled with resin and a scanned UV laser beam cures the superficial layer [5].

When compared to FDM printing, the small spot size of the laser and the low viscosity of the resin allow for much smoother surfaces, resulting in a greatly reduced minimum feature sizes in all directions, resulting in a typical voxel size of 50 x 50 x 50 μm^3. While greater resolution can be achieved, the capital equipment and running costs are significantly greater than those associated with FDM printing.

2.1.3 Electroless plating

Unlike FDM and SLA, with SLS it is possible to 3D print solid metal structures [3]; albeit having relatively poor conductivity and, therefore, high dissipative losses for microwave and millimetre-wave applications. In practice, this very expensive manufacturing technology is usually reserved for bespoke applications where metal casting or CNC machining is impractical.

The two very different 3D printing technologies considered here can create arbitrary 3D structures, but in general only from lossy dielectric materials (plastic with FDM and resin with SLA). As a result, in order to create MPRWG structures, the dielectric material is only used here as a structural support for the internal metal wall. This process is then followed by metal plating to realize the air-filled structure.

A standard commercial electroless metal plating process was employed. Here, the dielectric structure is sequentially immersed in a series of chemical baths for surface preparation, surface activation (with a catalyst) and metal deposition [125]. With optimal conditions, this technique is able to uniformly coat the entire surface of the structure with a seed layer, which can then be electroplated with the desired metal having a thickness that greatly exceeds five skin depths.

2.2 3D printed metal-pipe rectangular waveguides

The MPRWGs were originally designed to be compatible with standard flanges and waveguides [UBR100 flanges with WR-90 band (8.2-12.4 GHz) waveguides for X-band and anti-cocking UG-387/U-M flanges with WR-10 waveguides for W-band]. The calculated midband insertion loss for ideal waveguides having pure copper internal walls are 0.108 dB/m at 10 GHz for WR-90 and 2.69 dB/m at 90 GHz for WR-10 [126]. Obviously, assuming copper walls, the measured insertion loss for commercially available waveguides are expected to be higher than these theoretical lower bound values.

For manufacturing the larger X-band waveguide structures, FDM technology was employed, as it represents a lower cost solution; the larger voxel size and mechanical positioning repeatability may be considered to be within acceptable manufacturing tolerances for many microwave applications. With the metal plating process, for WR-90, the internal dimensions are sufficiently large to avoid regions of depleted solute within the chemical solutions inside the waveguide structure. As a result, the MPRWG components can be designed as a single-piece structure. An illustration of a WR-90-compatible thru line design is given in Figure 2.3(a).

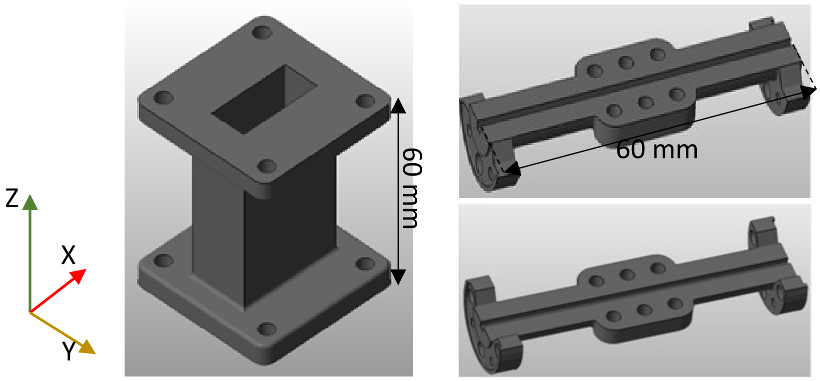

(a   (b)

Figure 2.3: CAD designs for 3D printable MPRWG thru lines. (a) Single piece WR-90 compatible. (b) Split-block WR-10 compatible. The printed layers are orthogonal to the Z axis.

An entry-level desktop 3D printer was used (Makerbot Replicator 2X) with acrylonitrile butadiene styrene (ABS) as the building material. The 3D printer software cuts the CAD drawing of a solid structure into horizontal slices and translates each slice into a 2-D path for the nozzle head to follow. The operator must first define three parameters: 1) surface wall thickness (1 mm in our case) along the *x*, *y* and *z* axes; 2) infill percentage between surface walls for the hexagonal (honeycomb) scaffolding in the *x*-*y* plane, along the *z*-axis (10% in our case); and 3) layer resolution along the *z*-axis (100 µm in our case). With our designs, the total thickness of the waveguide walls (i.e., distance between the surface walls) was 6 mm. After printing, electroless plating of a 3-µm-thick nickel seed layer was performed, followed by the electroplating of a 27-µm-thick layer of copper. The resulting manufactured thru line is shown in Figure 2.4. The weights for each individual post-plated flange and waveguide are 5.9 g and 250 mg/mm, respectively. Comparable waveguide components commercially available within our laboratory have corresponding values of 7.5 g and 730 mg/mm. Clearly, there is a considerable weight advantage in 3D printing X-band waveguides.

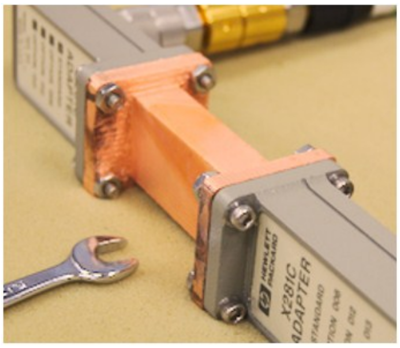

Figure 2.4: 3D printed and copper plated WR-90 thru line between commercial measurement test heads.

For manufacturing the smaller W-band waveguide structures, SLA technology was employed, as the smaller voxel size and higher mechanical accuracy of the galvo-scanner are required to meet the more demanding manufacturing tolerances of both flanges and waveguides. In contrast to WR-90, the internal dimensions of a single piece WR-10 structure are too small to give acceptable metal plating. As a result, a split-block design was adopted. To minimize radiation losses, the break was along the E-plane and located at the centre of the broad wall. In principle, SLA technology allows for good mechanical alignment of the two halves. An illustration of a WR-10-compatible thru line design is given in Figure 2.3(b).

The solid SLA printed parts were fabricated using a 3D Systems Viper si2® with Accura Xtreme resin [127] as the building material. This professional-level system offers a minimum focused laser beam spot diameter of 25 μm and a layer resolution of 25 μm. After printing, the same electroless plating and electroplating processes were performed as with the previous WR-90 waveguide components. The assembled manufactured thru line is shown in Figure 2.5. A small amount of warping of the two individual parts of the MPRWG was observed along its longitudinal direction. It is believed that warping is due to the built-in stresses that are created when the structure undergoes final curing in a UV oven after printing. However, with our self-aligning design for the two individual split-block parts, no noticeable warping in the final assembled components was observed.

(a) (b)

Figure 2.5: 3D printed and copper plated WR-10 thru line after assembly of the split block. (a) and (b) Side-view end view showing the self-aligned flange.

2.3 Internal surface roughness analysis

With both X and W-band MPRWGs, the surface profile after plating of the inner waveguide walls was measured using a Veeco Wyco® NT9100 optical surface profiler. A scan line in the *z*-direction represents the worst-case condition, due to scalloping associated with 3D printing; the measured results are shown in Figure 2.6. With FDM printing, the lower layer resolution and poor nozzle positioning repeatability cause significant levels of surface roughness (observed relative peak values of ± 13 μm) and steps (observed relative values of ± 3 μm), respectively. In contrast, as expected, SLA printing performs much better (observed relative peak values of surface roughness are ± 3 μm and without noticeable steps). The average surface roughness values, defined as the arithmetic average of the absolute values of the profile height deviations from the mean line [128], is calculated to be 4.02 μm and 0.93 μm with FDM and SLA printing, respectively. The root mean square surface roughness values, defined as the square root of the arithmetic average of the squared values of the profile height deviations from the mean line [128], are 4.99 μm and 1.16 μm with FDM and SLA printing, respectively. It can be seen that, when compared to FDM, SLA printing offers ~ 4:1 reduction in surface roughness.

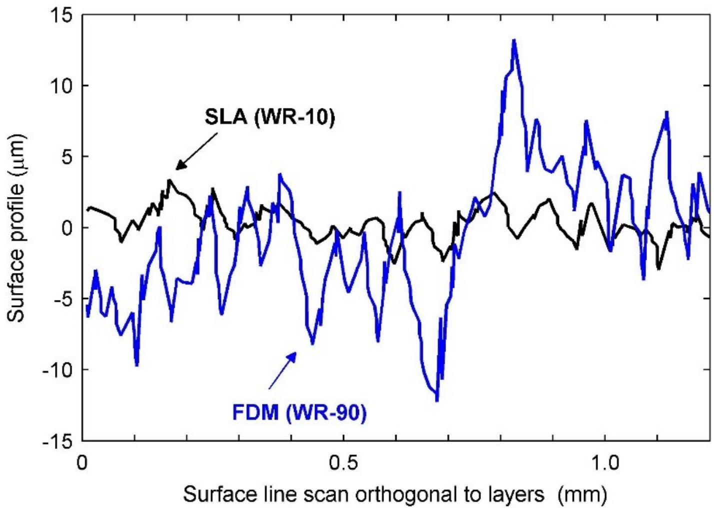

Figure 2.6: Measured postplating surface profile scan lines in the z-direction for both WR-90 and WR-10 compatible waveguides.

2.4 Traceable VNA measurements and methodology

Traceable scattering (S-)parameter measurements were carried out at the U.K.'s NPL. A HP8510C vector network analyser (VNA) was configured for use with either WR-90 or WR-10 waveguide test heads, covering the complete X-band or W-band, respectively. Thru-Reflect-Line (TRL) calibration [129] was first performed, using short circuit and 90° delay primary standards; the test head flanges define the 2-port measurement reference planes. An in-house calibration algorithm was employed, having a seven-term error-correction model [130]. The overall set-up (VNA, primary standards and calibration algorithm) is referred to as the NPL Primary Impedance Microwave Measurement System (PIMMS) [131], [132]. This is the U.K.'s primary national standard system for S-parameter measurements.

For each individual 3D printed and commercial machined (copper alloy WR-90 and aluminium WR-10, the latter taken from a Hewlett Packard VNA verification kit) reference thru line waveguide component, six measurements were taken; each measurement was preceded by a TRL calibration. The calibrated measurements were then processed by the PIMMS software to calculate the average results. This approach was chosen to reduce the influence of flange connection repeatability, cable flexing, system noise and changes in the ambient environment. As a result, the standard error of the mean is reduced, giving greater confidence in the measured results for these proof-of-principle demonstrators.

2.5 Measured S-parameters results

With WR-90, having standard internal cross-section dimensions of a = 22.86 mm and b = 10.16 mm, the lengths of reference thru lines were 60 mm and 127 mm for the FDM printed and commercial machined copper-alloy walled waveguides, respectively. Figure 2.7 show the measured return loss results across X-band. It can be seen that with a worst case return loss of 32 dB the FDM printed MPRWG has excellent impedance matching. With the commercial machined waveguide, the 41 dB worst case return loss performance can be attributed to the reduced alignment errors associated with its flanges (having higher precision in the position and diameter of the alignment/fastening holes). The almost identical and textbook return loss performances at both ports, seen in Figure 2.7, indicates good manufacturing tolerances for the FDM printed waveguide flanges.

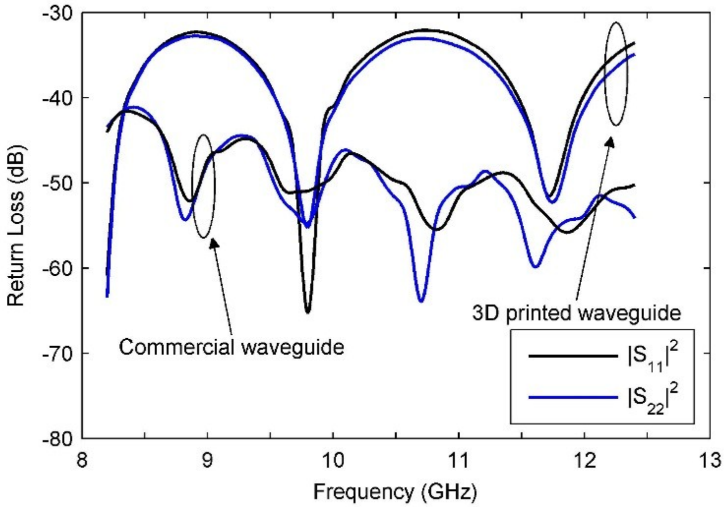

Figure 2.7: Measured return losses for the 60-mm length FDM printed and 127-mm length commercial machined WR-90 waveguides.

With uniform sections of MPRWG thru line, total power attenuation $\alpha_T = \alpha_R + l\alpha_D$ [dB] for a given physical length l [m] is due to impedance mismatch reflection losses α_R [dB] at the flange and dissipative (or ohmic) losses α_D [dB/m] associated with the internal metal walls, with [133]

$$\alpha_R = -10 \cdot log_{10}(1 - |S_{11}|^2) \text{ [dB]} \tag{2.1}$$

$$\alpha_D' = \begin{cases} -\frac{10}{l} \cdot log_{10}\left(\frac{|S_{21}|^2}{1-|S_{11}|^2}\right) \text{ [dB/m]} & \text{(a)} \\ -\frac{10\,\lambda_g}{l} \cdot log_{10}\left(\frac{|S_{21}|^2}{1-|S_{11}|^2}\right) \text{ [dB/}\lambda_g\text{]} & \text{(b)} \end{cases} \quad (2.2)$$

where λ_g is the guided wavelength; S_{11} and S_{21} are the measured input voltage-wave reflection coefficient and forward voltage-wave transmission coefficient, respectively. In general, (2a) is associated with feed lines and interconnects having arbitrary lengths; while (2b) is more appropriate for comparing distributed-element components of specific electrical length (e.g., $\lambda_g/4$ transformers and $\lambda_g/2$ resonators).

Since a designer can control α_R, given a stable manufacturing process, only α_D reflects the quality of a given manufacturing technology. Moreover, since α_R is negligible with our components it will not be considered further. Note that, after visual inspection of the assembled components and detailed numerical electromagnetic simulations, radiation losses associated with gaps between flanges or between the two halves of the split-block components were considered insignificant.

The measured dissipative attenuation results, using (2), are shown in Figure 2.11. With the FDM printed waveguide, the worst-case dissipative attenuation across the whole of X-band is only 0.017 dB/λ_g (or 0.58 dB/m). At 10 GHz, the dissipative attenuation is 0.33 dB/m, which is significantly more than the calculated value of 0.108 dB/m for the ideal copper WR-90 waveguide [126]. By comparison, the commercial machined waveguide has worst-case dissipative attenuation of 0.020 dB/λ_g (or 0.33 dB/m); at 10 GHz, the value of 0.30 dB/m is again still significantly higher than that calculated for the ideal copper waveguide. Nevertheless, the performance of the FDM printed waveguide is better below *ca.* 10 GHz, when compared to our commercial machined waveguide; above *ca.* 10 GHz, the higher dissipative attenuation is thought to be due to the increased levels of surface roughness with the internal copper walls of the 3D printed MPRWG.

With WR-10, having standard internal cross-section dimensions of a = 2.54 mm and b = 1.27 mm, the lengths of reference thru lines were 60 mm and 50 mm for the SLA printed and commercial machined aluminium-walled waveguides, respectively. Figure 2.8 shows the measured return loss results across W-band. It can be seen that, with a worst-case return loss of 16 dB, the SLA printed MPRWG still has good impedance matching.

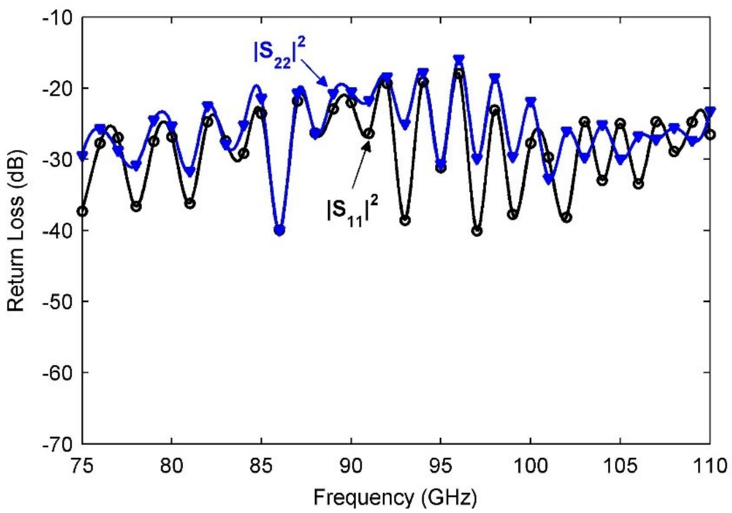

Figure 2.8: Measured return loss for the 60 mm length SLA printed WR-10 waveguide.

The measured dissipative attenuation results are shown in Figure 2.9. With the SLA printed waveguide, the dissipative attenuation increases from 0.06 and 0.03 dB/λ_g (or ~ 9 dB/m) at the band edges to a peak of 0.106 dB/λ_g (or 26.6 dB/m). The mid-band peak in attenuation (with corresponding degraded return loss), performance observed with measurements was extensively investigated using CST Microwave Studio. It was found that there was unexpected weak coupling into the air-filled ring cavity formed between the SLA printed and commercial machined anti-cocking flanges. This ring cavity has an inner diameter of 9.2 mm and outer diameter of 17.2 mm with a 1 mm thickness, and it includes the four fastening bolts and two alignment pins, as illustrated in Figure 2.10(a). Numerical simulations show two main resonance peaks at 93 GHz and 97.2 GHz and the electrical field distribution is shown in Figure 2.10(b) and (c). These frequencies match with the peaks seen in Figure 2.9.

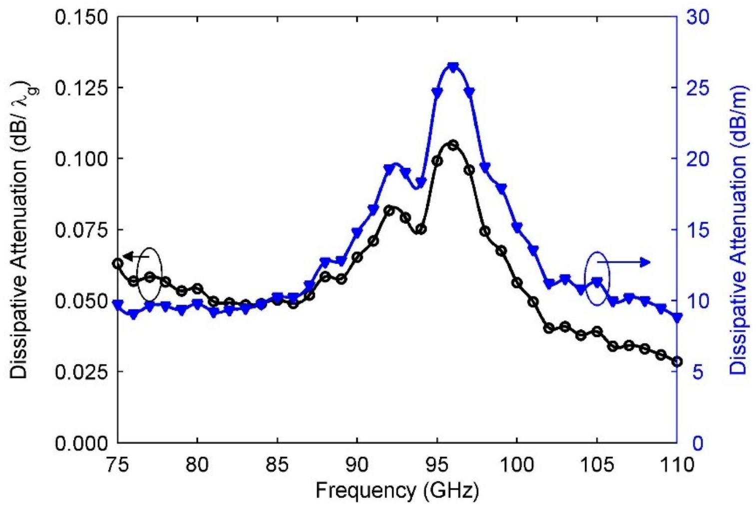

Figure 2.9: Measured dissipative attenuation for the 60 mm length SLA printed with electroplated copper walls WR-10 waveguide.

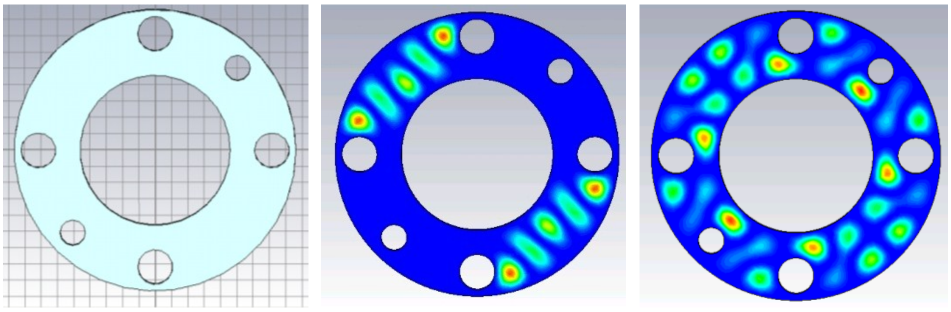

(a) (b) (c)

Figure 2.10: (a) Air cavity between the anti-cocking flanges. The diameter of the larger through holes for the screws and the smaller alignment holes have a diameter of 2.15 mm of 1.55 mm, respectively. Electric field in the cavity at (b) 93 GHz and (c) 97.2 GHz.

To suppress this unwanted resonance, the anti-cocking flange cavities with the FDM printed waveguide were filled with a conducting compound [the recipe for this compound consisted of 0.65 g of commercial polyvinyl-acetate (PVA) glue, 0.2 g of graphite powder (with average particle size of 10 µm), 3 g Pd/Ag conductive paste (DuPont 6143 [134]) and 0.5 g of ready-mix joint filler]. This compound results in an easily workable, high viscosity paste, having a conductivity of 430 S/m after a setting time of 2 hours at 40°C.

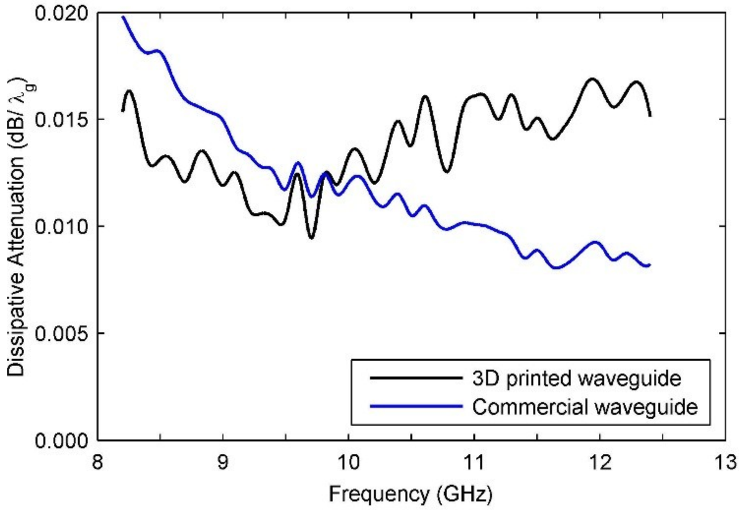

(a)

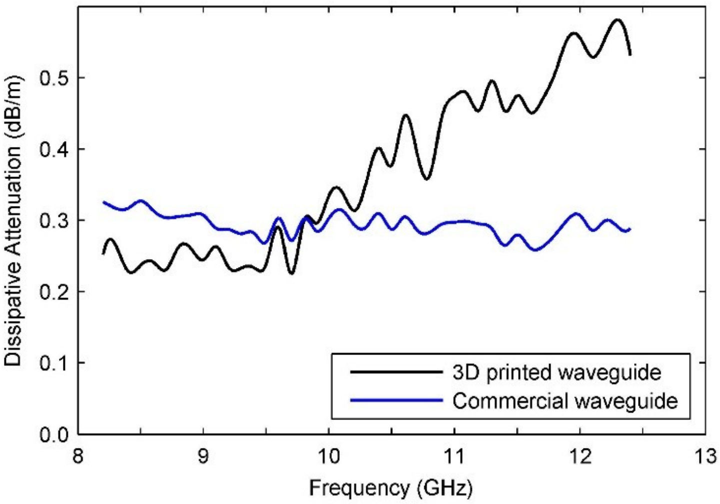

(b)

Figure 2.11: Measured dissipative attenuation for the 60-mm length FDM printed waveguide with copper walls and 127-mm length commercial machined WR-90 waveguides with copper alloy walls (a) per guided wavelength and (b) per meter.

The improved flange is shown in Figure 2.12. In addition, flat flanges were created at both test heads by inserting two calibrated shims (2.00 mm and 3.08 mm in length) from a Hewlett Packard VNA verification kit. The insertion loss of the two W-band shims were measured separately and found to be negligible. As a result, de-embedding was not considered necessary.

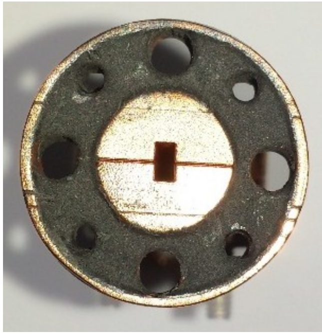

Figure 2.12: SLA printed waveguide flange with conducting compound filler.

Figure 2.13 show the measured return loss results across W-band. It can be seen that with a worst case return loss of 19 dB the SLA printed MPRWG still has good impedance matching. With the commercial machined waveguide, the 34 dB worst case return loss performance can be attributed to the greatly reduced alignment errors associated with its flanges. The almost identical and textbook return loss performances at both ports indicate good manufacturing tolerances for the commercial machined waveguide flanges. With 3D printing, our W-band flanges did not perform as well as the X-band flanges, due to the increased precision requirements needed for the order of magnitude decrease in waveguide cross section and the choice of split-block solution.

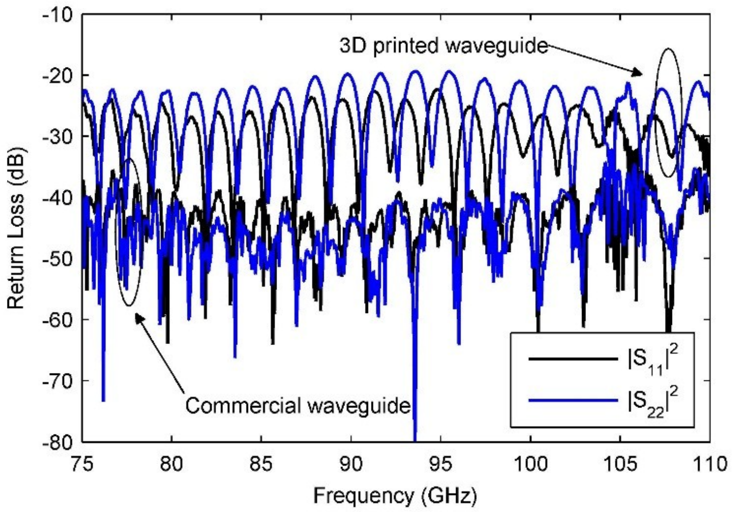

Figure 2.13: Measured return loss for the 60-mm length SLA printed and the 50-mm length commercial machined waveguides.

The measured dissipative attenuation results are shown in

Figure 2.14. With the SLA printed waveguide, the dissipative attenuation increases from ~ 11 dB/m at the band edges to a mid-band peak of 17 dB/m (or 0.07 dB/λ_g).

An iteration in the design and manufacture of the W-band flanges can eliminate the need for the conducting compound filler and introduction of shims. Moreover, since complex geometries can be 3D printed in a single run, the number of flanges needed within a subsystem can be minimized.

At 110 GHz, the dissipative attenuation of 11 dB/m is significantly greater than the calculated value of 2.69 dB/m at 90 GHz for the ideal copper WR-10 waveguide [126]. Nevertheless, at 110 GHz, the dissipative attenuation of 0.036 dB/λ_g (or 11 dB/m) is commensurate with the commercial machined aluminium waveguide performance of 0.032 dB/λ_g (or 10 dB/m) shown in

Figure 2.14 and much better than the micro moulded waveguide having 0.116 dB/λ_g (or 27.6 dB/m) at 92.6 GHz [91].

A comparison of measured dissipative attenuation results for MPRWGs realized using different manufacturing technologies is given in Table 2.1. It should be noted that this table does not represent an exhaustive survey of what can be found in the open literature, but acts as a useful guide.

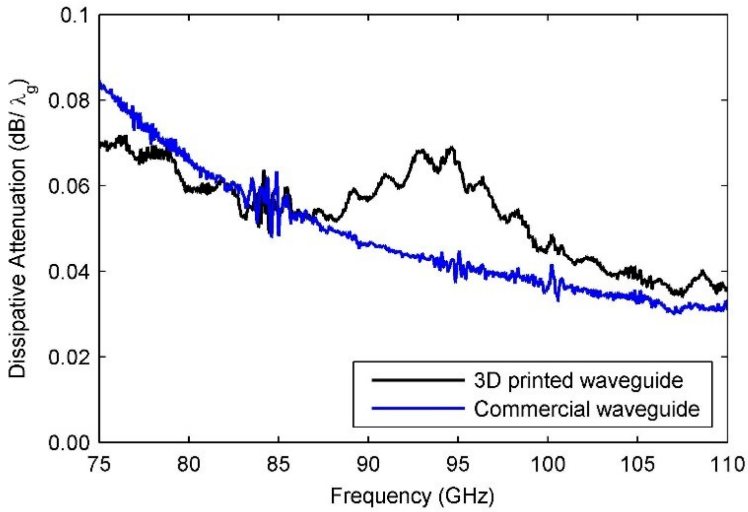

(a)

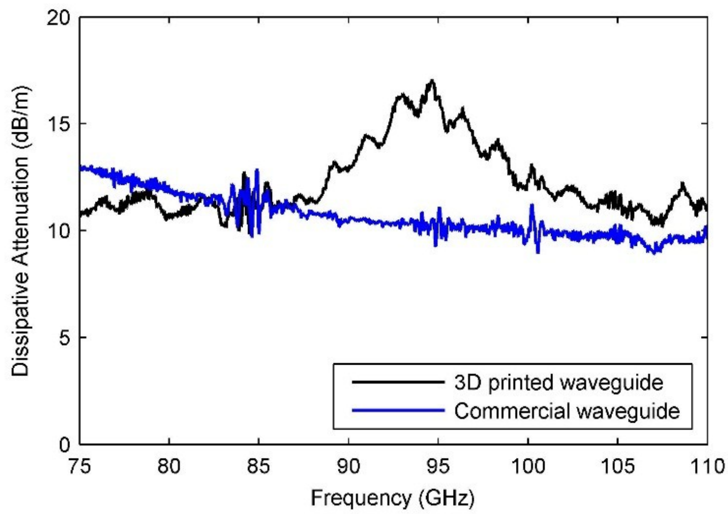

(b)

Figure 2.14: Measured dissipative attenuation for the 60-mm length SLA printed waveguide with copper walls and 50-mm length commercial machined waveguides with aluminium walls (a) per guided wavelength and (b) per meter.

Table 2.1: Comparison of published MPRWG measured attenuation performance.

Waveguide Band	Frequency (GHz)	Manufacturing Technology	Split block	Waveguide Filler	Attenuation		References
					dB/m	dB/λ_g	
WR-187	5	PCB processing	no	PET	700	5.41	[72]
WR-90	10	Machined	no	air	0.30	0.0115	-
WR-90	10	3D printed (FDM)	no	air	0.33	0.0130	This work
WR-28	33	PCB processing	yes	air	44.1	5.21	[73]
WR-12	60-80	Thick-film printing	no	HIBRIDAS HD 1000	500	-	[67]
WR-12	60-80	Thick-film printing	no	HIBRIDAS HD 1000	100	-	[71]
WR-19	50	PCB processing	yes	air	61.5	4.74	[72]
WR-10	92.5	Micro moulding	no	air	27.6	0.116	[91]
WR-10	100	Bulk micromachined silicon	yes	air	-	0.05	[76]
WR-10	105	Surface micromachined	no	polyimide	8,660	44	[65], [66]
WR-10	75-110	CNC machined	yes	air	4	-	[74]
WR-10	75-110	Surface micromachined	yes	air	-	0.5	[83]
WR-10	75-110	Thick-film printing	no	HIBRIDAS HD 1000	200	-	[71]
WR-10	75-110	Thick-film printing	no	LTCC	400	-	[70]
WR-10	110	Machined	no	air	10	0.032	-
WR-10	110	3D printed (SLA)	yes	air	11	0.036	This work
WR-3.4	280	3D printed	no	air	12	-	[115], [116]
WR-1.5	600	Bulk micromachined silicon	yes	air	80	-	[80]

Measurements uncertainty evaluation

As six measurements were performed for each of the manufactured components, it was possible to estimate the uncertainty on the measurements. The PIMMS algorithm associates a rectangular probability distribution (uniform distribution) to the measurements results and calculates the uncertainty, expressed as a circle centred on the measured complex value, as illustrated in Figure 2.15. In its output file the PIMMS algorithm returns the radius of such circle for each measured point of each of the four S-parameter.

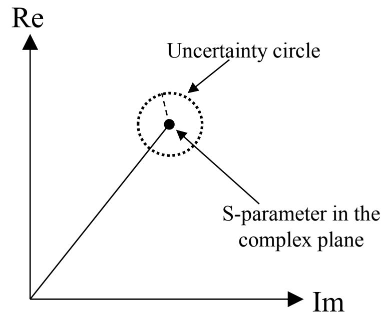

Figure 2.15: Illustration of the uncertainty expressed on the complex plane.

The average uncertainty radius in linear units for the four S-parameters of the X and W-band waveguides are reported in Table 2.2. The similar results between the reference (machined) and 3D printed waveguides show comparable measurements repeatability for the devices realised in the two different manufacturing processes. This indicates that with 3D printed waveguides a similar consistency in performance can be potentially achieved respect to machined ones.

Table 2.2: Radius of the uncertainty circle around the complex S-parameter for the reference and 3D printed waveguides in X and W-band.

	WR-90		WR-10	
	Reference	3D Printed	Reference	3D Printed
S11	0.0021	0.0022	0.0056	0.0048
S21	0.0062	0.0054	0.1611	0.1479
S12	0.0061	0.0054	0.163	0.195.5
S22	0.0021	0.0021	0.0055	0.0445

2.6 W-band filter

In addition to forming feed lines and interconnects, MPRWG technology is also used for implementing critical passive components and networks. For example, high quality (Q)-factor resonators are the basic building blocks for implementing high performance filters. Most of the microwave and millimetre-wave band-pass filters that are currently manufactured are of the Chebyshev family, which has a transfer function that produces the best out-of-band rejection for a given maximum permitted level of passband equiripple insertion loss [135]. Narrow-band high-order conventional Chebyshev filters (e.g. sixth-order and higher) will have their return loss zeros distributed across an extremely small frequency range and, therefore, a very accurate manufacturing process needs to be employed [135]. For this reason, a sixth-order Chebyshev band-pass filter will demonstrate the advantage of 3D printing over the micro moulded and more expensive (micro)machined technologies.

Here, an inductive iris band-pass filter implementation was chosen for the split-block solution, as illustrated in Figure 2.16, so as to minimize misalignment effects. The filter was designed to have an arbitrary chosen centre frequency of 100 GHz and a 3-dB bandwidth of 10 GHz.

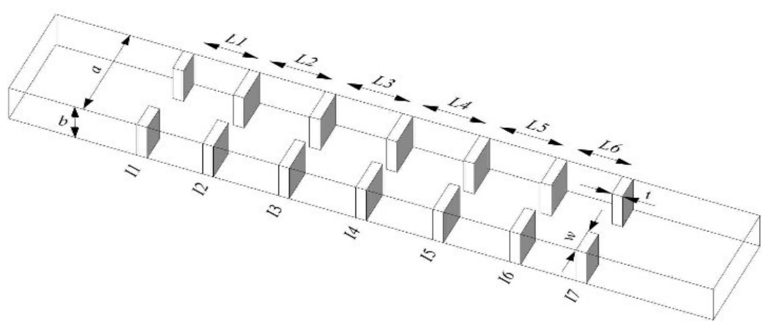

Figure 2.16: Illustration of the sixth-order inductive iris bandpass filter. The associated design values are given in Table 2.2, while the values measured after manufacture are given in Table 2.3.

The filter was designed using Guided Wave Technology (GWT) software that employs the mode-matching method [136]; iterations were needed to achieve spatial symmetry. It should be noted that an ideal manufacturing process is assumed (e.g., spatial features are perfectly rectangular, no mechanical misalignment and with perfect electrical conductor walls).

The minimum reliable thickness for an unplated iris wall was chosen; limited to approximately 140 µm, to maintain repeatability and tolerance control with SLA printing. In addition, the electroless and electroplating process was assumed to give a combined metal wall thickness of 30 µm, as found with the previously manufactured MPRWG thru sections. The inductive iris thickness was, therefore, chosen to be t = 200 µm.

The final filter design dimensions were entered into the numerical 3D modelling software CST Microwave Studio®, for verification; the values are given in Table 2.2. Figure 2.17 shows the simulated frequency response for the ideal band-pass filter. The six return loss zeros of the sixth-order Chebyshev filter can be clearly seen, with an associated predicted worst-case in-band return loss of 18 dB.

Figure 2.18 shows orthogonal cross sections through the filter structure, with the CAD layout and a single manufactured split-block part. The manufactured part appears to have no noticeable visual defects, when compared to the CAD layout.

Table 2.3: Filter design dimensions (assuming ideal manufacturing).

Plated Cavity Length, L (μm)		Plated Iris Width, w (μm)		
		Iris	*Left Side*	*Right Side*
L1	*1346*	*I1*	*583*	*583*
L2	*1551*	*I2*	*765*	*765*
L3	*1592*	*I3*	*809*	*809*
L4	*1592*	*I4*	*817*	*817*
L5	*1551*	*I5*	*809*	*809*
L6	*1346*	*I6*	*765*	*765*
		I7	*583*	*583*

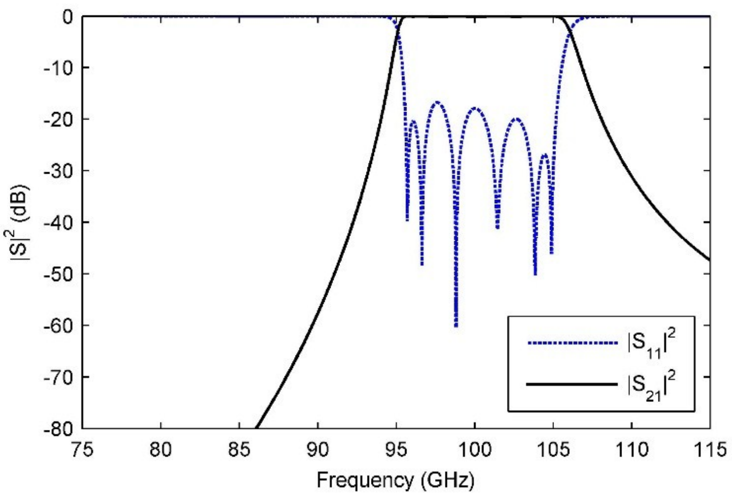

Figure 2.17: Simulated S-parameters for the designed sixth-order Chebyshev filter.

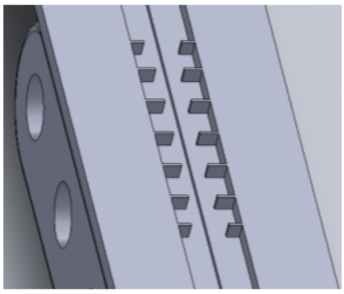

(a)

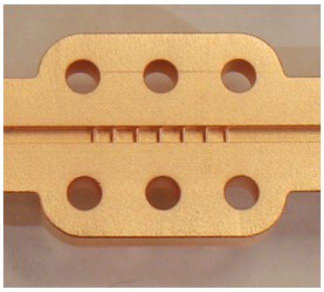

(b)

Figure 2.18: W-band sixth-order filter. (a) CAD layout showing a horizontal cross section through both parts of the assembled split block. (b) Photograph of a single manufactured split-block part showing the vertical cross section.

The physical dimensions for the manufactured filter were measured using a scanning electron microscope and the results are given in Table 2.3. From this data, it was found that there was an average shrinkage of 1.4 % in the resin structure after final UV curing. This results in shorter cavity lengths, increasing the frequencies of the return loss zeros and, therefore, increasing the overall pass band of the filter. In addition, the overall thickness of the metal wall was found to be over-plated by 25 μm, on average, resulting in a total plated inductive iris thickness of 248 μm. With variable resin shrinkage and over-plating, there will be slight asymmetries between the iris pairs associated with both split block parts. This has the effect of slightly reducing the frequencies of the return loss zeros. However, the net effect of resin shrinkage, over-plating and asymmetry is to increase the centre frequency of the pass band. Both internal and external cavity resonator coupling coefficients are directly proportional to the pass-band bandwidth [137]. Therefore, shrinkage and over-plating also results in reduced cavity coupling and a decrease in pass-band bandwidth.

Table 2.4: Manufactured filter dimensions.

Plated Cavity Length, L (μm)			Width and thickness (μm)				
	Left side	*Right side*	*Iris*	*Left side*		*Right side*	
				w	*t*	*w*	*t*
L1	*1283*	*1278*	*I1*	*639*	*228*	*599*	*224*
L2	*1487*	*1489*	*I2*	*759*	*256*	*820*	*252*
L3	*1533*	*1513*	*I3*	*889*	*251*	*857*	*246*
L4	*1525*	*1513*	*I4*	*892*	*248*	*860*	*264*
L5	*1481*	*1459*	*I5*	*879*	*234*	*867*	*248*
L6	*1244*	*1242*	*I6*	*776*	*296*	*826*	*323*
			I7	*623*	*215*	*580*	*222*

Measured internal waveguide dimensions: a = 2.51 mm, b = 1.25 mm.

The S-parameter magnitudes for the manufactured filter, measured using traceable national standards at NPL, are given in Figure 2.19. An excellent bandpass filter performance has been achieved, with a worst case pass band return loss of 11 dB and insertion loss of 0.95 dB at the centre frequency of 107.2 GHz. Clearly, the centre frequency has been shifted up by 7.2% and the bandwidth has shrunk from 10 GHz to 6.8 GHz with this first proof-of-principle demonstrator. With an optimized manufacturing process, design rules can be implemented to compensate for shrinkage and over-plating.

The loaded quality factor for the filter Q_L is given by

$$Q_L(f_0) = \frac{f_0}{\Delta f} = 15.76 \tag{2.3}$$

where f_0 is the centre frequency and Δf is the 3 dB bandwidth. The unloaded quality factor, Q_u, is obtained from the well-known relationship

$$Q_u(f_0) = \frac{Q_L(f_0)}{1 - |S_{21}(f_0)|} = 152 \quad (2.4)$$

The results for our sixth-order filter at 107.2 GHz can be favourably compared with those for the fifth-order filter fabricated using micro moulding manufacturing technology: $Q_L(95.4\ \text{GHz}) = 27.27$ and $Q_u(95.4\ \text{GHz}) = 82$ [92]; with almost twice the measured unloaded quality factor in the final fabricated demonstrator.

Because the original design dimensions in Table 2.2 have changed to the actual physical dimensions in Table 2.3, the measured S-parameters should be compared with re-simulations based on the values in Table 2.3. The results are shown in Figure 2.19, indicating a good fit.

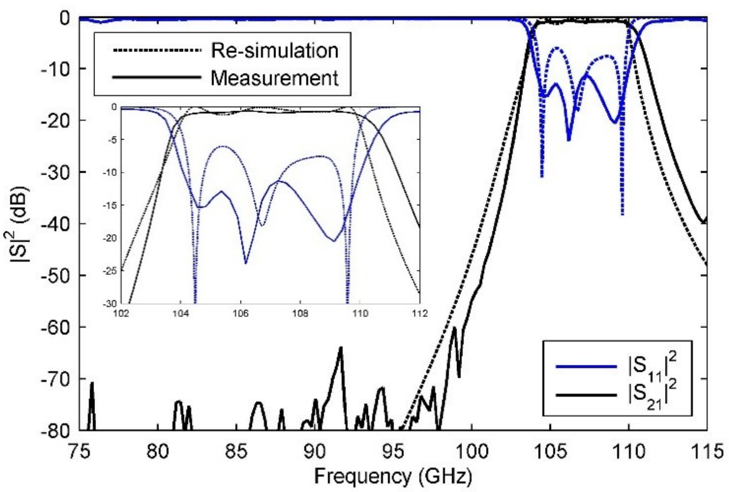

Figure 2.19: Measured and resimulated S-parameters for the sixth-order 3D printed W-band inductive iris band-pass filter.

For future development, compensation equations can be implemented to correct for shrinkage and over-plating. A possible method considers the shrinkage as a proportional error and the plating as an offset error, as in

$$s_{err}X_d + o_{err} = X_m \tag{2.5}$$

where X_d is the designed parameter (i.e. cavity length), s_{err} is the error introduced by the shrinkage, o_{err} is the error introduced by over-plating and X_m is the measured parameter after fabrication of a test piece with similar features.. As there are two unknowns, a minimum of two measurements are needed. Once s_{err} and o_{err} are known, it is possible to make a prediction and compensate at a design level.

2.7 Conclusions

In this chapter the manufacturing of air-filled metal-pipe rectangular waveguides using 3D printing technologies is investigated. Two very different technologies were considered: low-cost lower-resolution fused deposition modeling for microwave applications; and higher cost, high resolution stereolithography for millimetre-wave applications.

Measurements against traceable standards in metal-pipe rectangular waveguides were performed by the U.K.'s NPL to provide confidence in the measured results. It was found that the performances of the 3D printed MPRWGs were commensurate with those of commercial waveguides.

A high performance W-band sixth-order inductive iris bandpass filter, having a centre frequency of 107.2 GHz and 6.8-GHz bandwidth, is also demonstrated. The measured insertion loss of the complete structure (filter, feed sections and flanges) was only 0.95 dB at centre frequency, giving an unloaded quality factor of 152– clearly demonstrating the potential of 3D printed MPRWGs. This passive component fabrication technology offers the advantage of lightweight rapid prototyping/manufacturing. Then compared to traditional (micro)machining, with this technology costs are reduced by half up to a tenth (depending on geometrical complexity) with a potentially comparable performance. The potential price for the bespoke components in both the 3D printing technologies presented vary between £30 and £100 each, with the price mostly driven by the cost of the electroless plating, which depends on the exposed surface.

CHAPTER 3: 3D PRINTED PHASED ARRAY ANTENNA

The high geometrical complexity achievable with 3D printing enabled the simplified manufacturing of other passive microwave components at X-band; such as 90° bends, Tee-junctions, twists, horn antennas and bespoke metal-pipe rectangular waveguides.

The possibility to manufacture such components suggested that more complex systems could be realised with the combination of 3D printed waveguide components. In this chapter, the design and fabrication of a phased array antenna will be discussed and how each component was designed and manufactured using FDM 3D printing technology. Particular focus is on the design of a completely 3D printed waveguide variable dielectric-flap phase shifter.

3.1 Dielectric-flap phase shifter

3.1.1 Phased array antennas

Antenna directivity enhancement for long-range communications has been subject of extensive research in the past decades. Array antennas are multiple-antenna systems with radiating elements usually disposed in a periodical pattern along a line or on a surface. With antenna arrays the radiation pattern can be reinforced in a particular direction and suppressed in undesired directions, resulting in improved beam sharpness. In a phased antenna array each element is fed via a variable phase shifter. This allows for the direction of phased array radiation, also known as look angle, to be electronically steered without the need for any mechanical rotation.

Because of this, since the advent of this technology, phased array antennas have found a wide range of applications, in particular when the antenna cannot be mounted on a gimbal. Traditionally used in military applications (e.g., missile guiding and tracking) [138], [139], they now have gathered increasing interest for civilian radar-based sensors and communication systems in commercial applications [140]–[144]. However, despite the broad range of potential applications, phased array antennas are still uncommon in the commercial arena, due to their high cost and complexity.

3.1.2 Theory

Phased array antennas are systems that allow one to electronically steer the main beam lobe of an antenna array, without physically moving the antenna. The beam steering is achieved by feeding each element of the antenna array with a progressive phase shift. The maximum distance between each element d_{max} of the array depends on the operating wavelength λ and the maximum look angle required θ_{max}, and can be calculated by

$$d_{max} = \frac{\lambda}{1 + \sin\theta_{max}} \text{ [m]} \tag{3.1}$$

Attempting to steer the beam further by increasing the progressive phase shift would generate unwanted grating lobes. Phase shifters have the fundamental role in phased array antennas to introduce the progressive phase shift that enables the beam steering. The beam steering angle θ depends on the progressive phase shift ψ at each element and the distance between elements d as in

$$\theta = \sin^{-1}\left(\frac{\lambda}{2\pi d}\psi\right) \text{ [deg]} \tag{3.2}$$

Figure 3.1 shows the array factor for a four-element linear array evenly spaced with d = $\lambda/2$, obtained from

$$AF(\theta) = \sum_{i=0}^{3} e^{ji(\psi - kd\sin(\theta))} \tag{3.3}$$

where the wavenumber $k=2\pi/\lambda$.

Look angle	Array factor	*Relative phase shift*
$\theta = 0°$	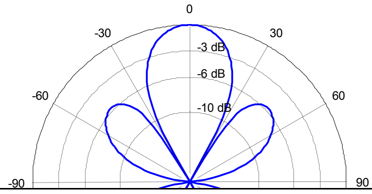	$\psi = 0°$
$\theta = 15°$	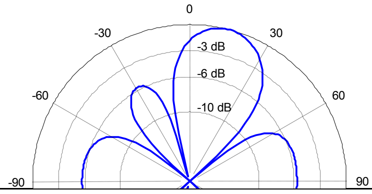	$\psi = 45°$
$\theta = 30°$	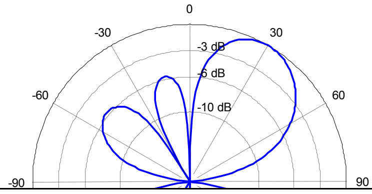	$\psi = 90°$
$\theta = 45°$	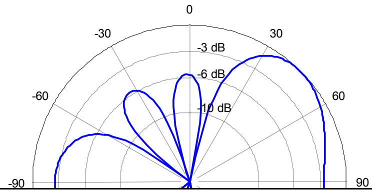	$\psi = 128°$
$\theta = 60°$	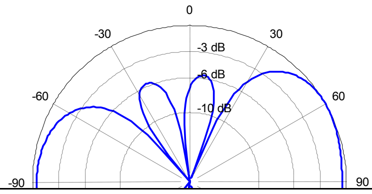	$\psi = 156°$
$\theta = 75°$	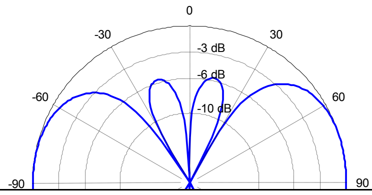	$\psi = 174°$
$\theta = 90°$	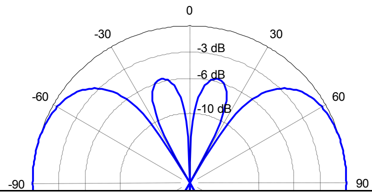	$\psi = 180°$

Figure 3.1: Array factor for a four-element phased antenna array. Changing the progressive phase delay ψ from 0 to 180° changes the corresponding look angle θ between 0 and 90°.

3.1.3 Dielectric flap phase shifter design

A variety of integrated waveguide phase shifters, often based on ferrite, can be found in the open literature [145]. However, in order to take full advantage of

FDM technology, a dielectric-based phase shifter was considered for the manufacturing of an X-band tuneable phase shifter. The insertion of dielectric into an air-filled waveguide at the point of maximum electric field increases the effective dielectric constant, thereby causing the guide wavelength λ_g to decrease, as in

$$\lambda_g = \frac{\lambda}{\sqrt{\varepsilon_{eq} - \left(\frac{\lambda}{2a}\right)^2}} \ \text{[m]} \tag{3.4}$$

where λ is the wavelength in free space, ε_{eq} is the equivalent relative permittivity (i.e. dielectric constant) in the section of waveguide having the dielectric, and a is the internal broad wall dimension of the waveguide. Thus, the insertion of dielectric increases the transmission phase of the wave passing through a fixed length of waveguide section. Several possible configurations employing low loss dielectric slabs are possible [146]–[150]. These devices, however, require the substitution of the slab or electrically-controlled actuators inside the waveguide to move the slab and vary the transmission phase. Other possible alternatives include slabs of low loss dielectric moved inside the waveguide by thin rods or inserted through a non-radiating slot [151], [152], as illustrated in Figure 3.2.

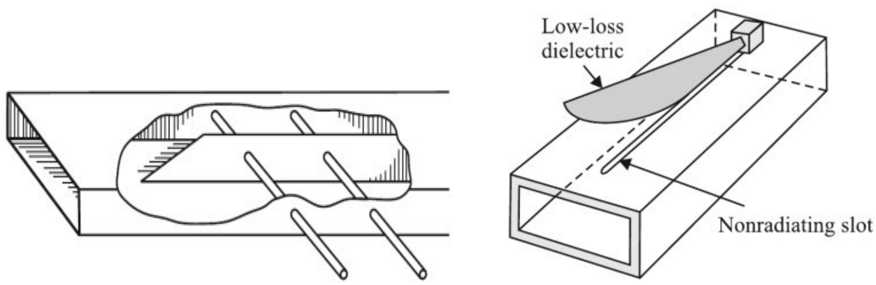

(a) (b)

Figure 3.2: (a) Tapered slab of dielectric in a waveguide, moveable with thin rods; (b) curved dielectric flap inserted in a non-radiating slot on the waveguide [151].

Due to its simpler design and ease of tuning, the configuration with a slot and dielectric flap was chosen. By placing the slot at the centre of the broad wall, the dielectric flap can be inserted where the E-field is at its maximum. The curved shape of the flap is resorted to reduce the reflections. The depth of insertion, on which also the length of the insert in the waveguide depends, changes the effective propagation constant of the waveguide. With this design, care needs to be taken in order to avoid the propagation of higher order modes in the waveguide and radiation from the slot.

3.2 Phase shifter simulations and measurements

Very little was found in the open literature on dielectric-flap phase shifters and, therefore, its design was mainly based on numerical simulations. The aim was to obtain the maximum possible phase shift in a single section of waveguide. The maximum length of the X-band waveguide section and its associated slot length were limited by the maximum building volume of the Makerbot 2X; these were designed to be 150 mm and 100 mm long, respectively. The two parameters left for the design are the shape and thickness of the flap. The profile of the flap was chosen to be an arc of circle, so that its curvature would be the same at any depth of insertion. A radius of curvature of 130 mm was chosen, so that the flap would reach the opposite side of the waveguide with its deepest point, when fully inserted. The thickness of the flap was chosen as the maximum possible value that would not allow the propagation of higher order modes and minimise the radiation losses from the slot. Numerical simulations were used to optimise this parameter. ABS, the same building material for all the FDM 3D printed parts, was chosen as the dielectric material for the flap. ABS was modelled with a dielectric constant ε_r = 2.54 and loss tangent $tan(\delta)$ = 0.015 at 10 GHz [153]. From the numerical simulations, with CST Microwave Studio, the optimum parameter for the slot width which would keep radiation losses to a minimum was found to be 3 mm and a maximum phase delay of 173° was predicted when the flap is fully inserted (flap angle equal to zero) at 10 GHz. The CAD drawing for the designed WR-90 phase shifter and the flap are shown in Figure 3.3. Figure 3.4 illustrates the simulated field patterns in the waveguide when the flap is fully raised or inserted, showing how the wavelength decreases in the region with the dielectric flap.

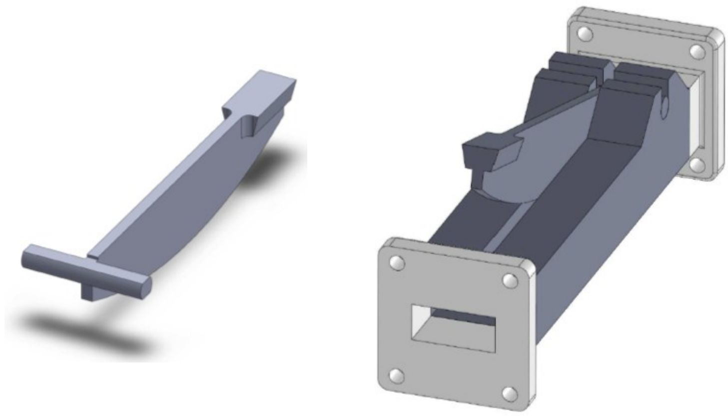

(a) (b)

Figure 3.3: (a) Dielectric flap and (b) waveguide with slot and moveable dielectric flap.

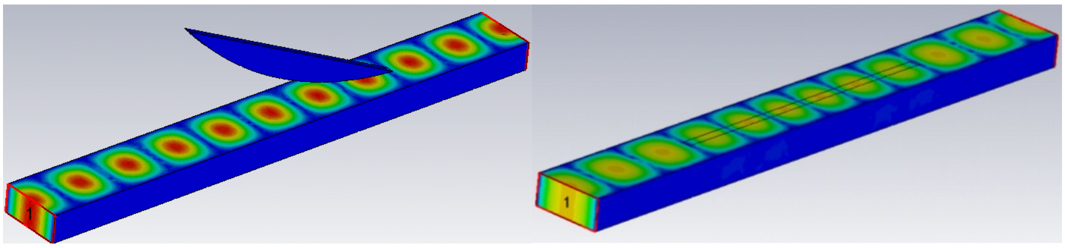

(a) (b)

Figure 3.4: Electric field pattern in the waveguide (a) with the flap removed and (b) with the flap fully inserted.

The manufacturing process was identical to the 3D printed WR-90 waveguides in the previous chapter, with the dielectric flap left un-plated. The manufactured WR-90 waveguide phase shifter is shown in Figure 3.5.

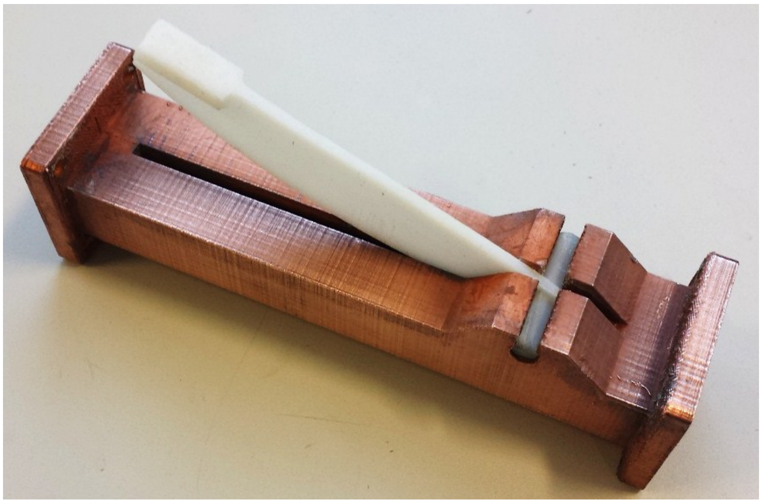

Figure 3.5: Manufactured waveguide phase shifter.

The complete structure was simulated with CST Microwave Studio to find the expected phase shift for different flap angles and the simulated results compared with measurements. Figure 3.6 shows the simulated and measured phase shift at 10 GHz. Figure 3.7 shows the measured insertion phase, relative phase shift and differential-phase group delay over X-band.

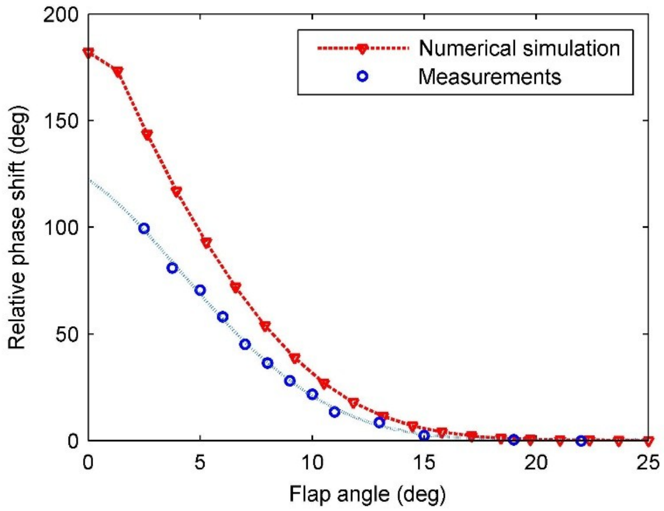

Figure 3.6: Measured and simulated phase shift against dielectric flap angle at 10 GHz.

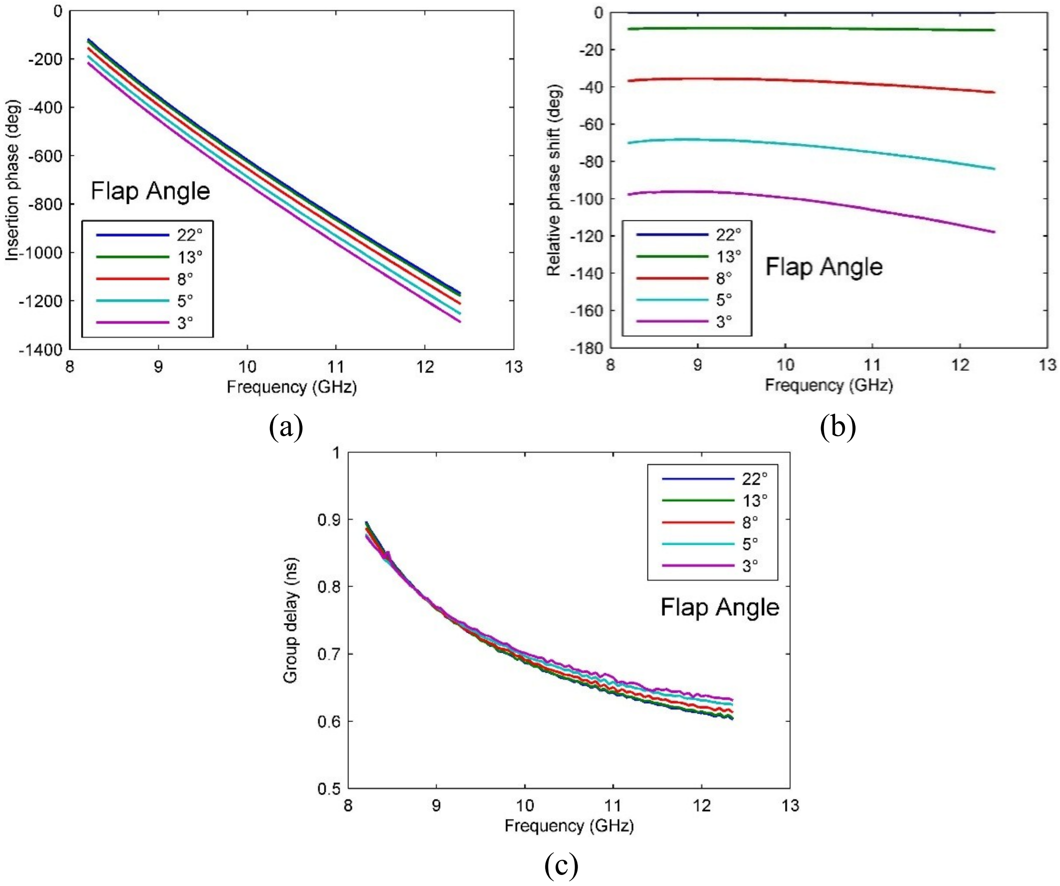

Figure 3.7: Measured (a) insertion phase, (b) relative phase shift, and (c) differential-phase group delay across X-band of the phase shifter for different flap angles.

For the manufactured part, due to fabrication tolerances, it was not possible to fully insert the flap, causing a minimum angle of 3°. The phase shifter, in its linear region, shows a 10° relative phase shift per degree of flap angle, against the simulated predicted value of 16°, and has an expected maximum relative phase shift of 128° if the flap is fully inserted.

The difference between measurements and simulated predictions can be attributed to parallax error in the measurement of the angle, variation in dielectric constant and also density of the 3D printed flap. Indeed, the 3D printing process, which deposits layers of melted plastic filament, will leave air micro-gaps during the deposition, thus reducing the effective density of the printed part. This would eventually cause a reduction in the effective dielectric constant and, therefore, a reduction in relative phase shift. As shown in Figure 3.8 for different flap angle, low levels of insertion loss were recorded (due to the dielectric and radiation), with a worst case value of -0.206 dB at the upper end of X-band. More importantly, the phase-to-amplitude (PM-AM) conversion is also very low, which is important for antenna phased arrays.

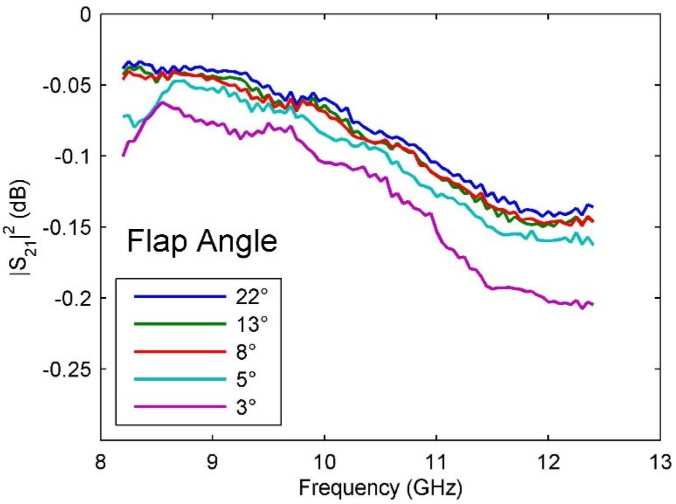

Figure 3.8: Insertion loss for different dielectric flap angle.

3.3 Phased array antenna design

After the design and manufacturing of the phase shifter, all the other components needed for the four element phased array antenna were designed. The whole system was to be completely 3D printed and the first step was to create the manifold feed to the four antenna elements, which most importantly includes the 3-port power splitters. This will be achieved via conventional Tee junctions, two 90° mitred bends and a further two bespoke Tee junctions.

3.3.1 Tee junctions

The input signal is first split into two with a Tee junction. This power splitter was designed as an H-plane junction with a septum to optimise return losses. To achieve a balanced power at the two output ports, a septum was introduced and positioned at the centre; numerical simulations were used to choose the length and width of the septum. Figure 3.9 shows a CAD drawing of the Tee junction with a cross-section, the unplated and plated 3D printed part.

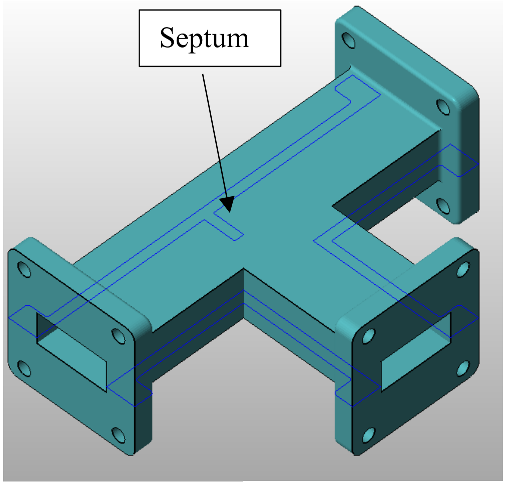

(a)

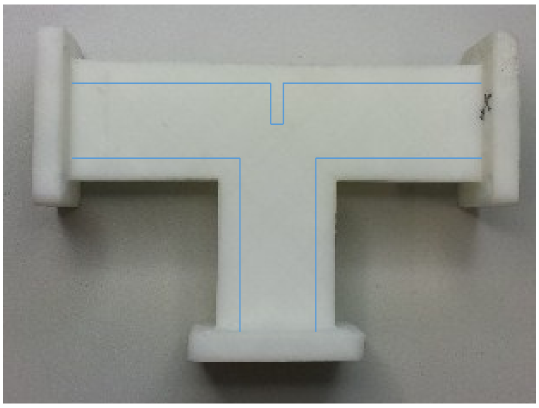

(b)

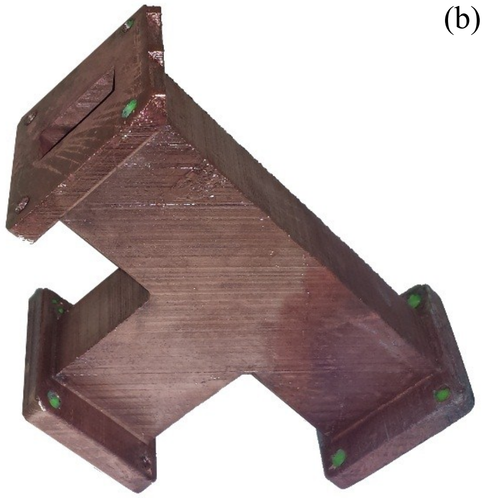

(c)

Figure 3.9: (a) Tee junction CAD model with cross-section profile showing the septum, (b) unplated and(c) plated 3D printed part.

The structure was simulated using CST Microwave Studio for different septum combinations of length and width. The length of the septum was varied between 3 and 13 mm and the width between 3 and 9 mm. The results illustrated in Figure 3.10 show that the length and width that gave the best performance were 10 mm and 3 mm, respectively. For this component, the measured S-parameters showed a particularly poor performance and the cause was identified in the lack of good internal plating. For this reason the measured results will not be reported.

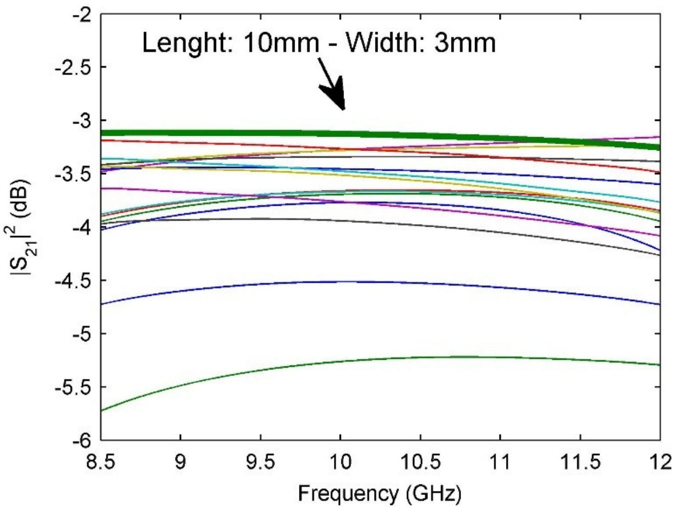

(a)

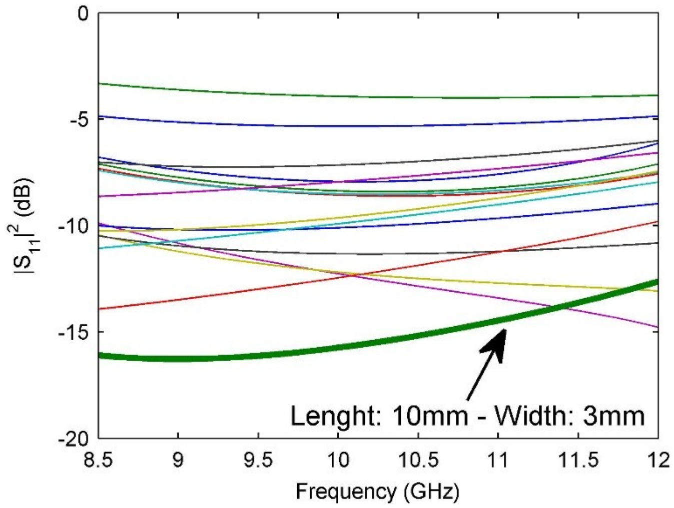

(b)

Figure 3.10: Simulated S-parameters showing the (a) transmitted and the (b) reflected power for the simulated Tee junction for different septum combinations of length and width. As the structure is symmetrical, only one of the two output ports is shown.

3.3.2 Mitred Bend

Waveguide bends are now required to re-direct the signal. Mitred bends are generally preferred to curved bends when a more compact circuit is desired. The bend was numerically simulated for different internal mitre lengths d between 10 and 30 mm; a value of 20 mm, corresponding to λ_g /2 for a frequency of 10 GHz, was chosen. The CAD model and the fabricated part are shown in Figure 3.11. The simulation and measurement results are shown in Figure 3.12 and 3.13, respectively.

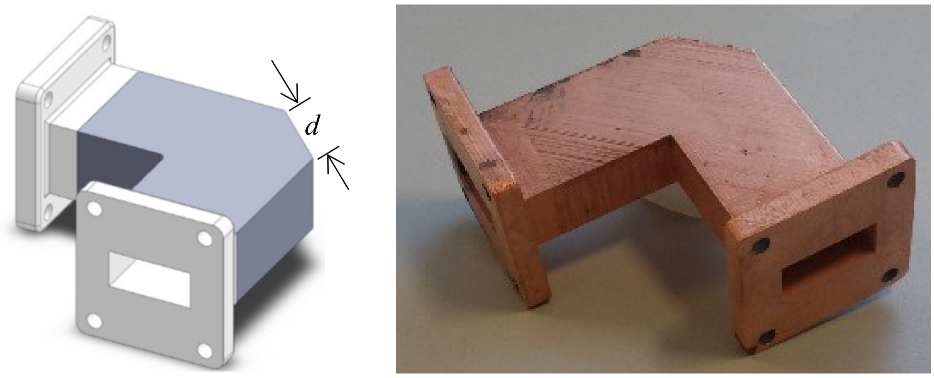

(a) (b)

Figure 3.11: (a) Mitred bend CAD model showing the mitre size *d* and (b) fabricated part.

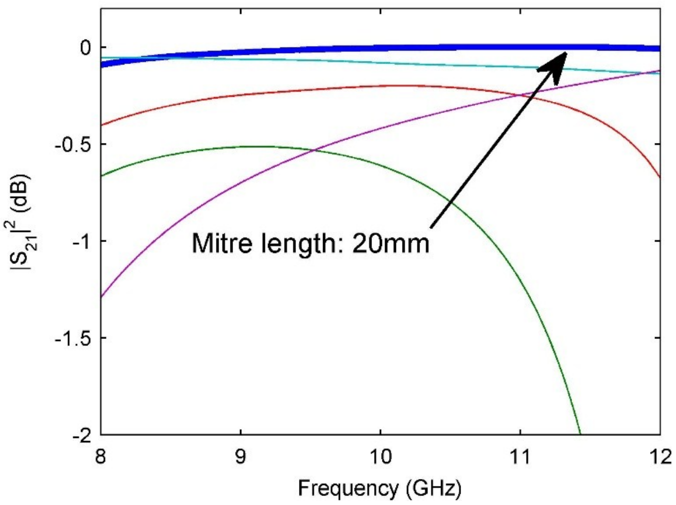

Figure 3.12: Simulated S-parameters showing the transmitted power for the mitred bend for different mitre lengths between 10 and 30 mm.

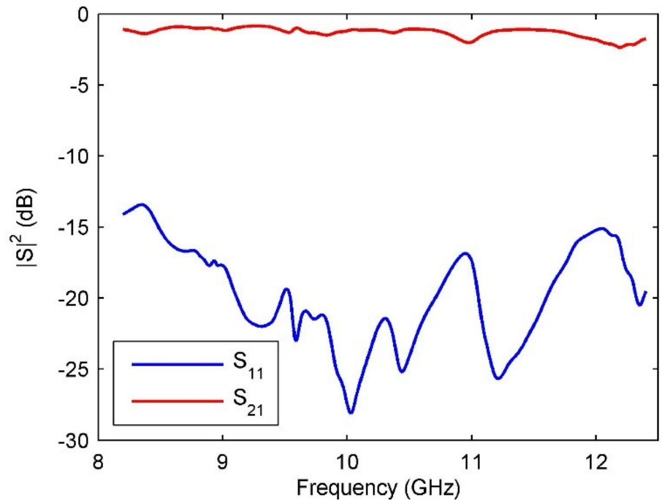

Figure 3.13: Measured S-parameters for the 3D printed 90° mitred bend in X-band.

3.3.3 Combined Tee

Now that the input power is split into two, another power divider was designed. To obtain a more compact system, a Tee junction combined with two mitred bends was the chosen solution. While the bend dimensions were kept constant, the dimensions of the septum needed to be optimised again, because of the shorter electrical length between the septum and the bend. The optimisation process was based on simulations, in a similar way to the Tee junction. The new optimal dimensions for the septum were 1.0 mm and 9.7 mm for the width and length, respectively. Figure 3.14 shows the CAD drawing in the designed component and the measurement setup.

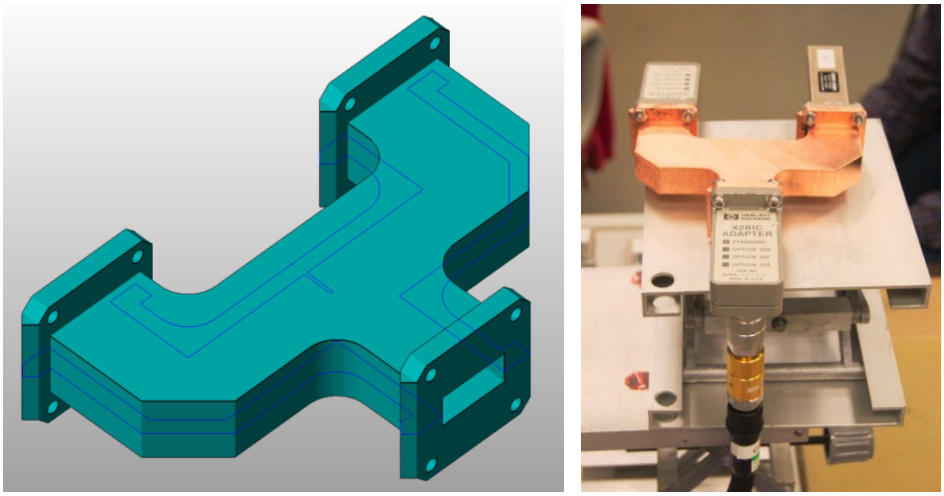

(a) (b)

Figure 3.14: (a) Combined Tee junction CAD model with cross-section profile showing the septum and (b) 2-port measurement setup for the combined Tee junction with the third port terminated with a matched load.

Numerical simulation predictions and measurement results are reported in Figure 3.15 and 3.16, respectively.

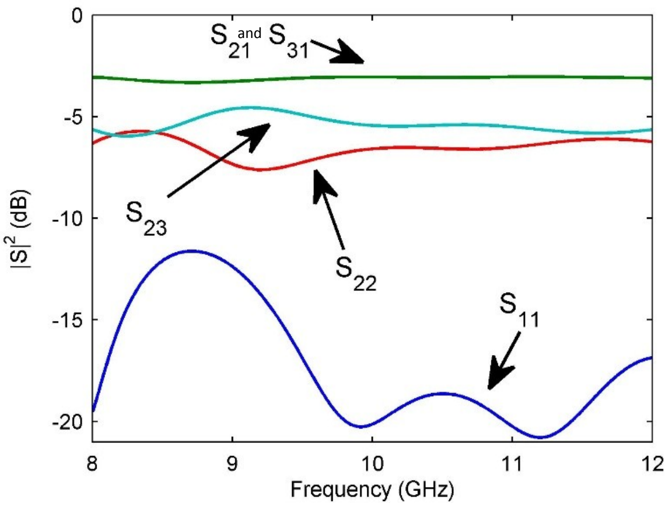

Figure 3.15: S-parameters showing the simulated transmitted and reflected power between the three ports for the designed combined Tee junction.

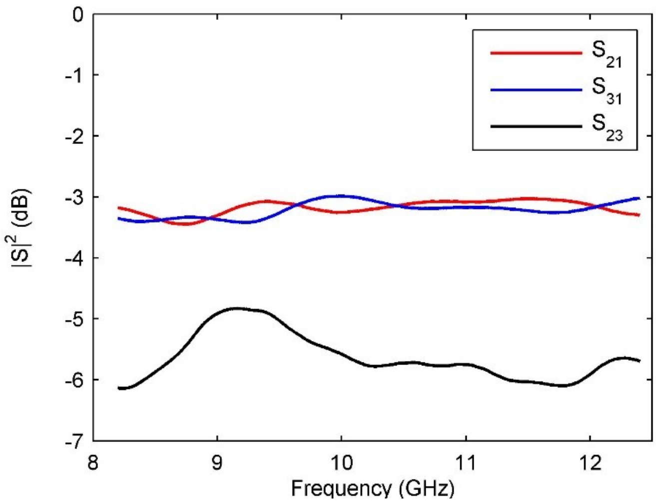

(a)

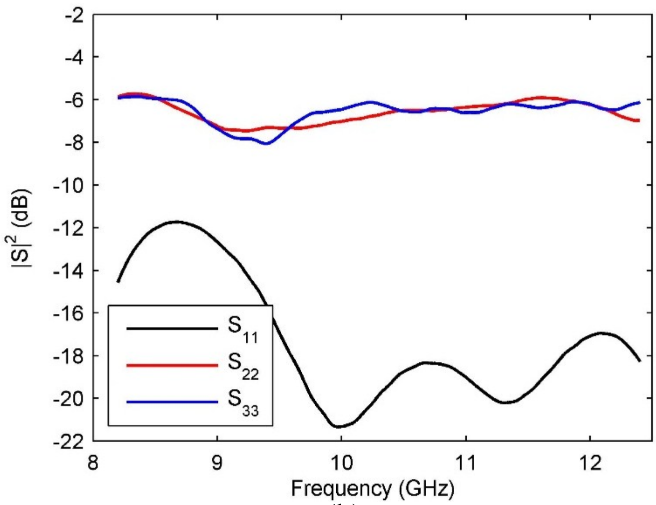

(b)

Figure 3.16: Measured S-parameters showing the (a) transmitted and the (b) reflected power for the Tee junction.

3.3.4 Horn antenna array

Assuming that the signal is separated into four equal paths, with identical path lengths, the 4-element antenna array can be designed. The antennas chosen are H-plane horn antennas spaced $\lambda/2$ apart; at 10 GHz, corresponding to a physical separation of 15 mm. The dimensions of the antenna elements were based on a commercial equivalent (Microwave Instruments Limited, WI 6148) with internal horn length and width dimensions of 75 mm. The CAD design and the 3D printed antenna array (before and after plating) are shown in Figure 3.17.

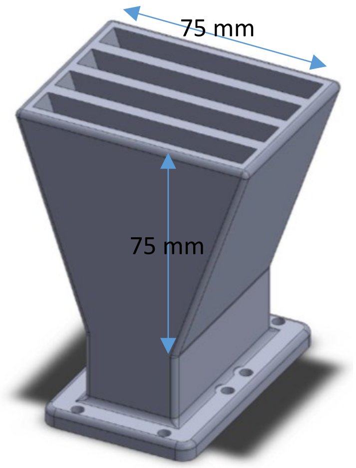

(a)

(b)

(c)

Figure 3.17: (a) Designed, (b) unplated and (c) plated 3D printed horn antenna array.

The single element was simulated to predict its radiation pattern and the result is shown in Figure 3.18.

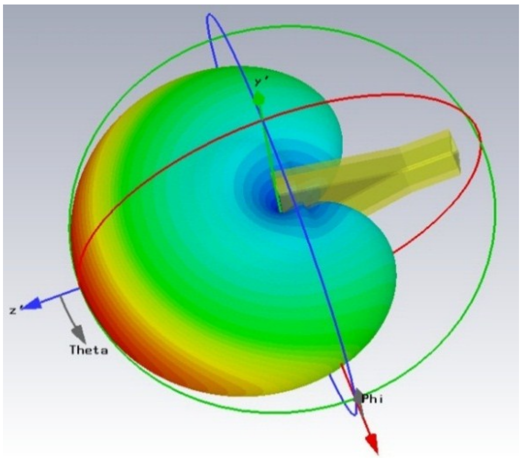

Figure 3.18: Radiation pattern for a single H-plane horn antenna element of the array.

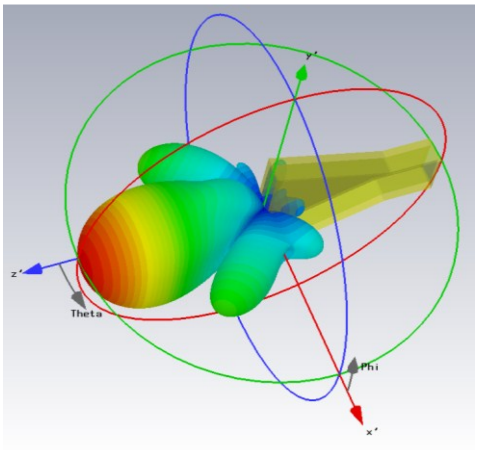

Figure 3.19: Radiation pattern for antenna array without any phase delay.

The antenna array was also simulated and the 3D radiation pattern shown in Figure 3.19. The simulation results for different progressive phase delays showing the beam steering are illustrated in Figure 3.20. As the fabricated phase shifter can achieve a maximum phase shift of approximately 120°, the progressive phase shift between each of the four antenna array elements was varied between 0 and 40°. All the results shown are for an operating frequency of 10 GHz. The -3 dB main lobe angular width varies between 25° and 26° and a beam steering of 3° per 10°

phase shift is found in the simulation range. For the antenna array a simulated peak gain of 51 is predicted against the simulated peak value of 13 for the single element.

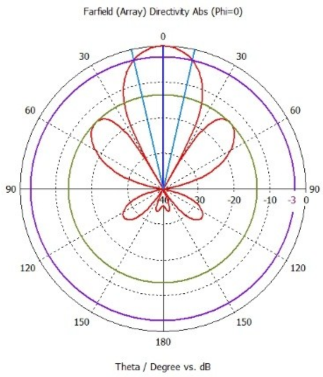

ψ: 0°
θ: 0°

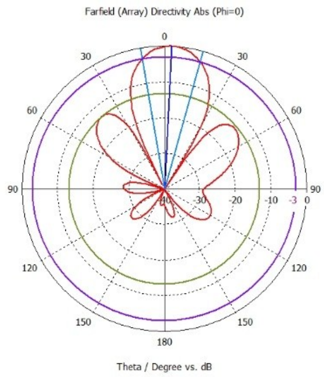

ψ: 10°
θ: 3°

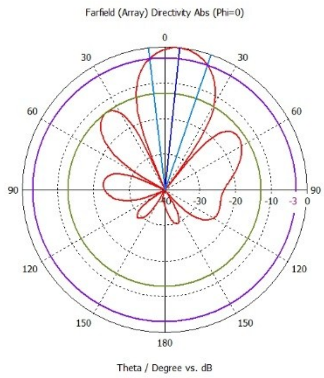

ψ: 20°
θ: 6°

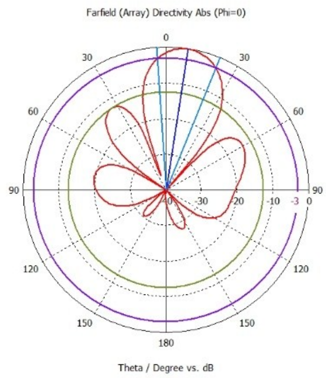

ψ: 30°
θ: 9°

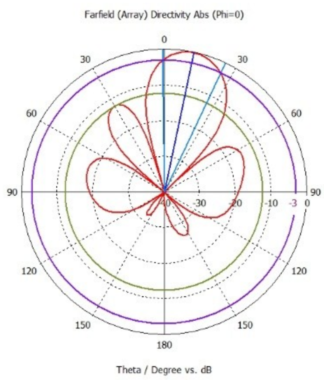

ψ: 40°
θ: 12°

Figure 3.20: Radiation pattern in dB scale of the phased array antenna for different phase shift.

3.3.5 Adapter block

While all the other manufactured parts have standard UBR100 flanges, Figure 3.17 shows that the antenna array has a non-standard connection to accommodate the four rectangular waveguide feeds. 3D printing allowed the manufacturing of bespoke curved sections of waveguide with custom flanges, which allowed connecting the antenna array to the four phase shifters. The CAD drawing and a cross section of the branching adapter waveguides are illustrated in Figure 3.21. This structure is composed of curved sections of waveguide built in pairs. The radius of curvature is equal to 80 mm, approximately $2\lambda_g$ at a frequency of 10 GHz, with the path length of each section identical (to keep the phase shift consistent between each of the four feed lines).

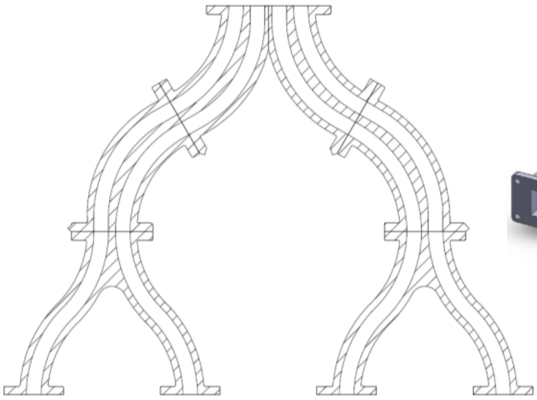

(a)

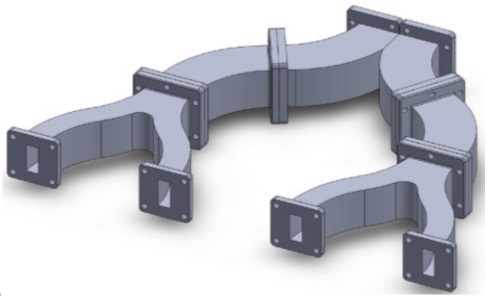

(b)

Figure 3.21: (a) cross section of the branching adaptor block to feed the antenna, and (b) CAD drawing

The signal is fed into the four phase shifters via the 3D printed splitter block, using Tee junctions, two mitred bends and two combined Tee junctions. However, the splitter block and the adapter block have orthogonal waveguide orientations; requiring the need for four additional twist sections. The twists were also 3D printed and have a total length of 10 cm, including flanges, and a constant rotation gradient of 1.125°/mm. In numerical simulations, the adapter block and the twist show ideal performance, with return loss below 30 dB for the twist and below 50 dB for each line of the adaptor block, across X-band. While, because of the bespoke flanges it was not possible to measure the performance of the adapter block, the designed twist was measured and the results shown in Figure 3.22. The complete structure is shown in Figure 3.23.

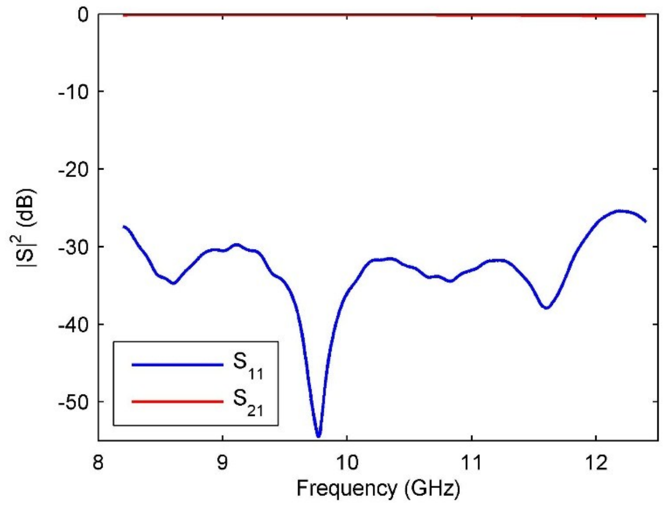

Figure 3.22: Measured S-parameters for the 3D printed twist in X-band.

Figure 3.23: Full 3D printed phased array antenna system (including feed splitters, phase shifters and antenna adaptor block).

3.3.6 Complete system

Although results are reported for most of the components, because of defects in the plating, the overall yield of fully working devices was of relatively poor. Moreover, due to the bespoke flanges, the antenna array and the components of the adaptor block could not be fully characterised. However, by cascading together all the simulations for each of the components in CST Design Studio, the ideal behaviour of the whole system was simulated. As expected, for an identical flap angle at each phase shifter, the four signals received by the antenna array are in phase. The adapter block does not introduce any phase shift between the four paths. However, for different flap angles, the loss introduced is different (because of PM-AM conversion) and, therefore, there will be a slightly different amplitude weighting of the signals fed to the individual antenna elements. The simulation results for the transmitted and reflected power, when all the phase shifters are in the same configuration and when a progressive phase shift is introduced, are shown in Figure 3.24 and 3.25. In all cases, an average value of -6.3 dB is observed for the power transmitted to the antenna, indicating that the input power is evenly split between the four feed lines. The insertion phase when a progressive relative phase shift is introduced is illustrated in Figure 3.26, showing a linear response across X-band.

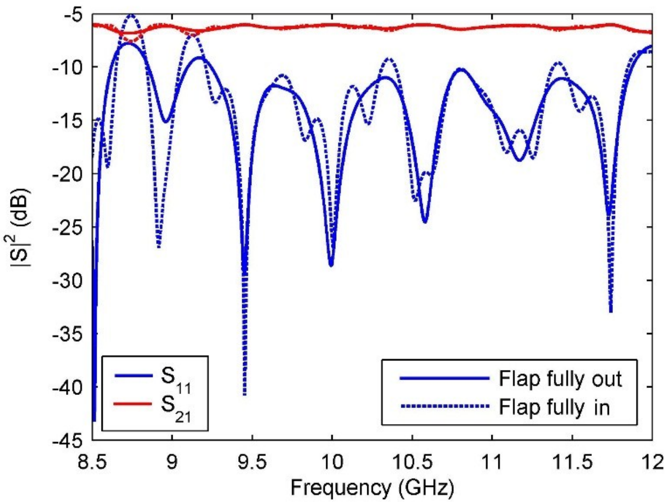

Figure 3.24: Simulated S-parameters for the complete phased array antenna feed line system when the flaps for all phase shifters are fully inserted or extracted.

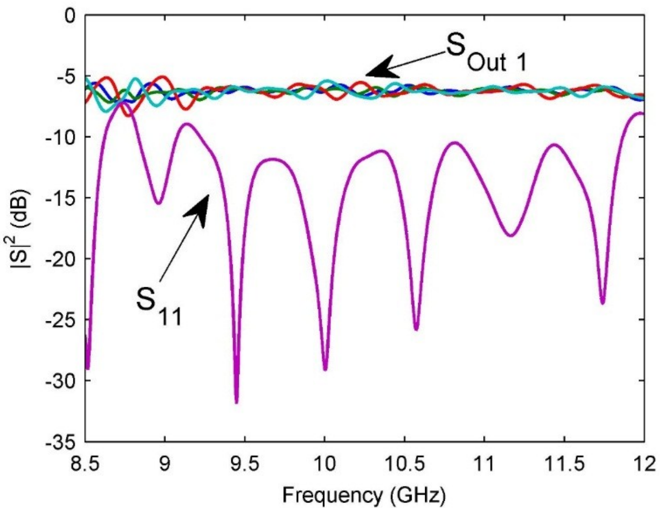

Figure 3.25: Simulated S-parameters for the complete phased array antenna feed line system when the maximum progressive phase shift is introduced.

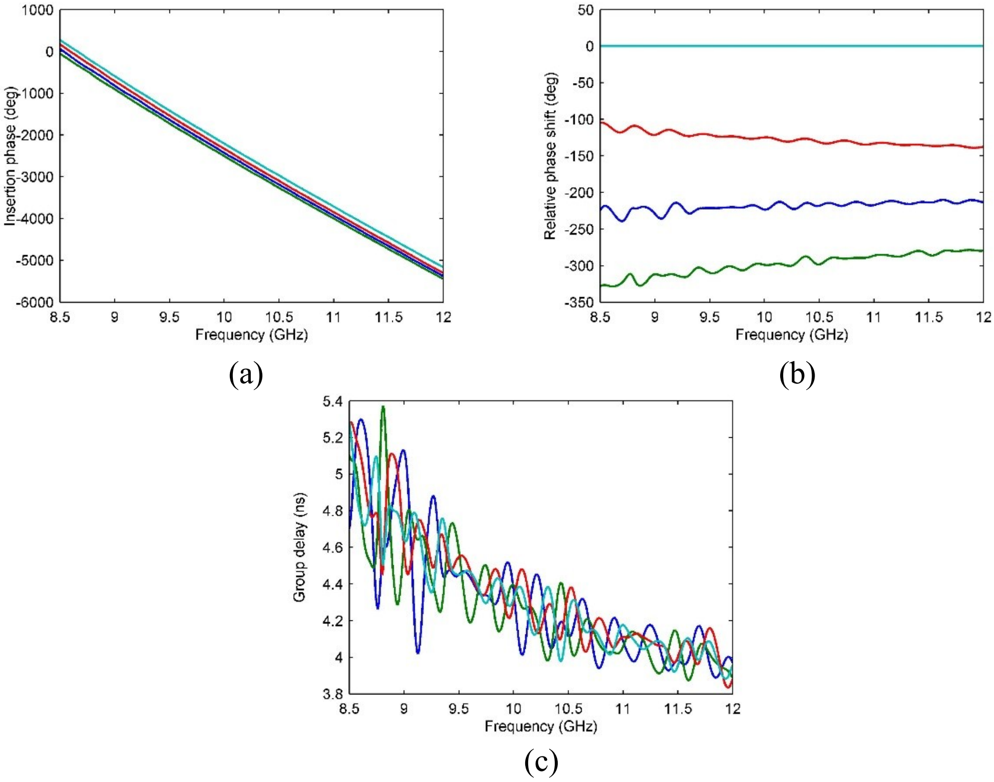

Figure 3.26: Simulated (a) insertion phase, (b) relative phase shift and (c) differential-phase group delay against frequency for the complete phased array antenna feed line system when the maximum progressive phase shift is introduced.

3.4 Conclusions

In this chapter, the design and manufacturing of a fully 3D printed phased array antenna is reported. Simulations indicate that the designed system would be able to steer the beam ±12° by adjusting the dielectric flap angle of the phase shifters. A larger steering angle can be achieved by using multiple phase shifter stages connected in cascade. Nevertheless, the manufacturing process for these more geometrically complex components, with plating in particular, requires improvements in order to obtain a performance comparable to numerical simulations and better yield. Repair the unplated patches with conductive paint was attempted with no success. Figure 3.27 shows an example of a failed 90° bend with bad plating and scarring left by the support material.

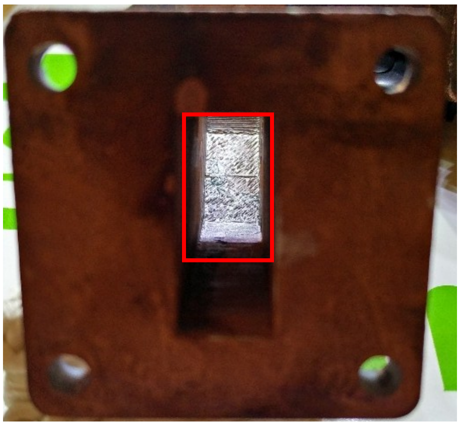

Figure 3.27: Failed plating and residual scarring after the support removal on the internal mitre for a WR-90 90° bend.

CHAPTER 4: LTCC SUSPENDED STRUCTURES

The work reported in this chapter was produced under the IeMRC grant for "3D microwave and Millimetre-wave System-on-substrate using Sacrificial Layers for Printed MEMS Components". This project was conceived, proposed and led by Professor Ian D. Robertson at the Institute of Microwaves and Photonics (IMP), University of Leeds.

4.1 Low temperature co-fired ceramic

Glass-ceramic composite materials, such as Low Temperature Co-fired Ceramics (LTCCs), have been extensively used as substrates for high frequency circuits. This is because of their low dielectric losses (for example, having a loss tangent of the order of 10^{-3} for commercially available LTCC sheets) and as packaging for their resistance to harsh environments (i.e. high temperature or corrosive atmosphere). Although examples of sacrificial material-supported cavities can be found in the open literature, the micromachining of suspended structures for the development of actuators has been widely neglected, because of challenges that this material poses when micromachining small structures.

Green LTCC tape is produced by pouring and casting slurry onto a supporting polyester or polyimide tape. The slurry is composed of a suspension of alumina powder (Al_3O_2), glass powder (SiO_2), organic solvents, binders, functional oxides (and other aggregates). The functional oxides will also influence the sintering temperature, dielectric constant, thermal coefficient of expansion (TCE) and mechanical properties of the fired LTCC. During the firing process, the organic components will outgas, leaving the powder compact ready for the sintering process. After firing, the LTCC will mechanically behave as a sintered ceramic body (hard, brittle and rigid).

For the patterning of green LTCC, two techniques are commonly used: punching and laser machining. The former can form high quality vias, however, it presents several limitations, such as tool wear, slow speed and no possibility of trimming (partial material removal to reduce the substrate thickness). Conversely, laser machining cuts and creates vias in the substrate with a taper angle, is fast, has no tool wear and is capable of trimming. In particular, the trimming ability makes laser machining the method of choice for the machining of suspended structures in LTCC. Moreover, laser cutting can also be used for the singulation of fired LTCC modules.

4.2 LTCC Laser trimming

The aim in the first part of this research project was to realise suspended structures in LTCC by using sacrificial layers and laser micromachining. Suspended structures such as bridges (fixed-fixed beams) or cantilevers (fixed-free beams) are essential for the fabrication of RF MEMS. Particularly, focus was on the manufacturing of thin suspended beams, in order to have a low actuation voltage.

The LTCC sheets used were DuPont 9K7-X [154], with a nominal thickness of 245 μm. Due to the relatively high Young's modulus of the fired LTCC (145 GPa), this thickness proved to be unsuitable for the realization of compact flexible structures. Thus, laser micromachining was employed to reduce the thickness of the LTCC sheet and then to pattern the beam. The laser system used was a LPKF Protolaser 100, equipped with galvo-scanner and a 13 W pulsed solid-state Nd-YAG (1064 nm) laser. Through hands-on collaboration, the manufacturing process was undertaken with the Institute of Microwaves and Photonics (IMP) at the University of Leeds.

The first step to developing a repeatable laser trimming process, which would achieve a thin membrane of LTCC with low roughness, was the study of the ablation of LTCC. The nominal focused laser spot size of our system has a diameter of 25 μm. To have a uniform distribution of energy on the substrate, the relationship between scanning speed and pulse frequency was fixed to obtain a 50% overlap for each pulse giving the following

$$\frac{scanning\ speed\ [\mathrm{mm/s}]}{pulse\ frequency\ [\mathrm{kHz}]} = 12.5\ \ [\mu\mathrm{m}] \tag{4.1}$$

To realize the membrane, the laser beam was raster scanned on the substrate with a scan line interval of 12.5 μm. Experiments were performed on a green (unfired) single 254 μm thick layer of LTCC. Different combinations of power and speed/frequency were tested, as shown in

Table 4.1, to investigate the effect of the parameters on the surface roughness of the machined area. The choice of power range used was based on previous experiments, aimed at evaluating the minimum value that would generate observable ablation and the maximum value that would not cause damage in the surrounding areas after a single scan.

Table 4.1: Test conditions for laser trimming of LTCC.

Test Condition	Power, %	Pulse Frequency, kHz	Scanning Speed, mm/s
1	50	20	250
2	50	40	500
3	50	80	1000
4	60	20	250
5	60	40	500
6	60	80	1000

Figure 4.1 shows micrographs of the machined areas after a single scan under six test conditions. The machining process was repeated one, five and ten times on each individual area. The average measured roughness is reported in Table 4.2. For certain combinations, no result is reported as all the material was removed by laser machining.

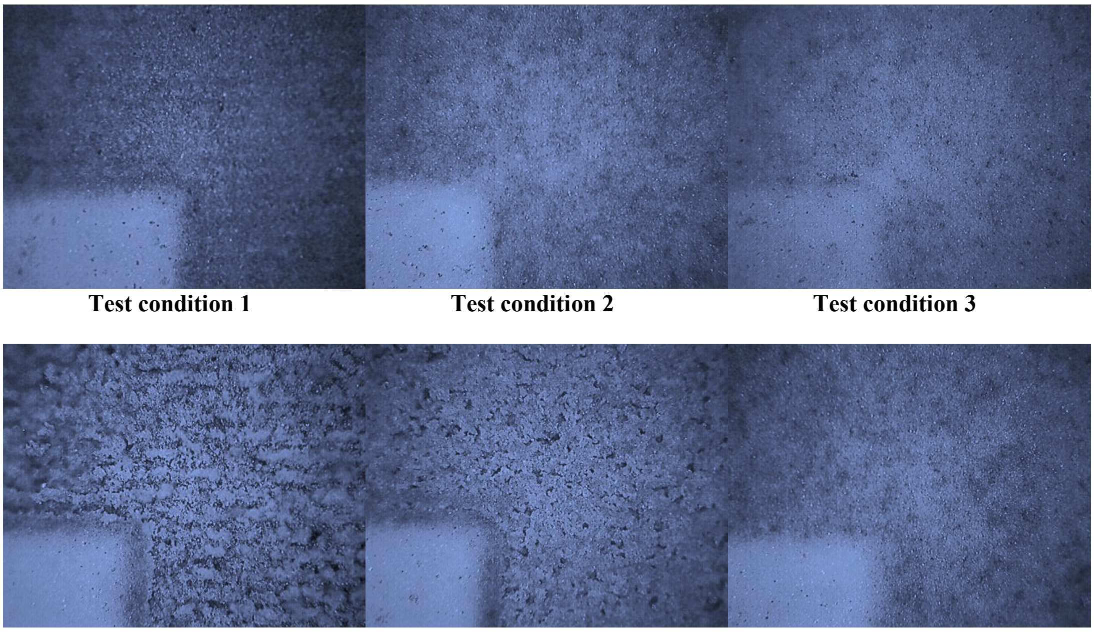
Test condition 1 Test condition 2 Test condition 3

Test condition 4 Test condition 5 Test condition 6

Figure 4.1: Micrographs of the machined area for the six different parameter combinations. The clearer area in the bottom left corner of each micrograph is non-processed LTCC.

Table 4.2: Average surface roughness of the trimmed area under the six different test conditions after one, five and ten machining cycles.

Test Condition	Average Surface Roughness		
	1 cycle, nm	5 cycles, nm	10 cycles, nm
1	361	290	284
2	214	220	224
3	202	178	166
4	1346	N/A	N/A
5	1018	617	N/A
6	202	247	209

N/A indicates that no material is left due to over-machining.

Following the surface roughness experiments, further tests were conducted to measure the etching rate for each machining cycle. During these tests the scanning speed-pulse frequency ratio was kept constant, as in the previous experiments. The results showed that slower scanning speed and higher power leads to higher etching rates. However, this rate was not constant and reduced substantially after the first cycle, slightly increasing as the cycles increased. This can be explained by different conditions of thermal dissipation, as material in the trimmed window decreases.

Table 4.3: Average etch rate per cycle of the laser trimming process under the six different test conditions.

Test Condition	Average etch rate/cycle, nm		
	1 cycle, nm	+4 cycles, nm	+5 cycles, nm
1	3105	550	800
2	2875	250	400
3	2054	500	758
4	75386	N/A	N/A
5	7333	1280	N/A
6	1875	444	500

The etch rate is defined as the average amount of material removed per cycle after the first cycle, after four more cycle and after a further 5 cycles.

Based on the previous experimental results a multi-step process was developed, which combines the high etching rate of low-speed and high-power machining with the low roughness of high-speed and low-power machining. This optimised process is shown in Table 4.4. The results obtained using this recipe show that a thickness of 90 ±3 µm could be obtained with an average surface roughness below 200 nm.

Table 4.4: Optimised process for LTCC trimming from 254 µm to 90 µm.

Cycles	Power, %	Pulse Frequency, kHz	Scanning Speed, mm/s
4	60	40	500
1	60	60	750
1	60	80	1000
30	50	80	1000

<u>Observations on LTCC laser trimming</u>

From the results obtained after extensive laser trimming experiments, it is reasonable to assume that the LTCC underwent physical change during machining. The high amount of localised heat generated by the infrared laser would lead to the evaporation of the organic binders and the sintering of the ceramic powder. This causes an increase in the energy needed for ablation and, therefore, a reduction in the etching rate. Effects of the highly localised heat were noticeable when laser cutting structures out of a trimmed LTCC sheet. Figure 4.2 illustrates that glass beads were formed along the cutting contour line for two cantilevers. These are caused by the concentrated heat at the edge of the cut, which melted the glass matrix of the LTCC. This demonstrates the effect of heat during laser machining and the limits in the maximum power for LTCC laser processing.

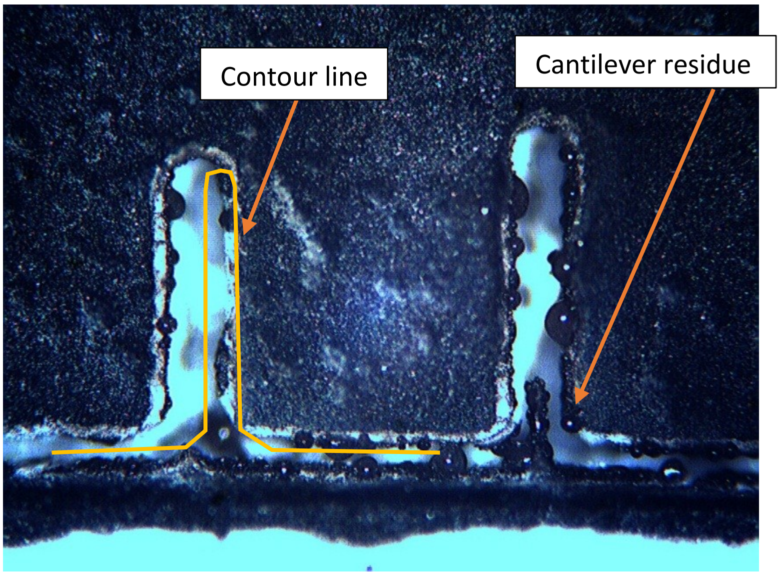

Figure 4.2: Formation of glass beads during laser cutting of two cantilevers in LTCC. The excessive heat form the high laser power destroyed the cantilevers.

4.3 Suspended bridges

After the development of an LTCC laser trimming process, the next step was the laser cutting of the beams. Following the formation of a 90 µm thick 12 x 2 mm membrane in the LTCC sheet, via laser trimming, the contours of the beam suspension were laser-cut. Nine 2 mm long fixed-fixed beams (i.e. bridges) were made with three different configurations (straight, double-beam and folded bridges) and three widths, as illustrated in Figure 4.3. The straight and the folded bridges both have a designed beam width of 50, 100 and 150 µm. The double-beam bridges each have beam widths of 50, 100 and 150 µm, with a separation gap of 25 µm.

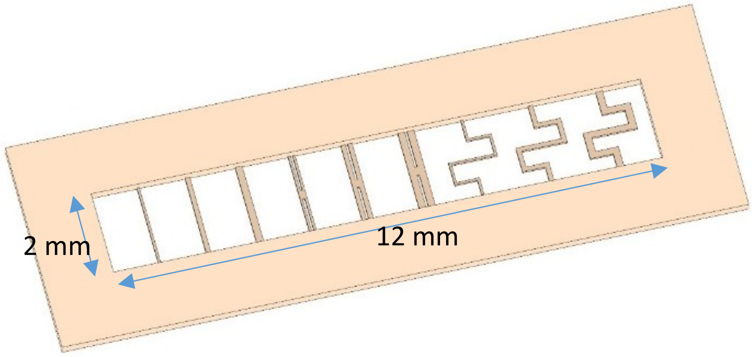

Figure 4.3: CAD drawing of the LTCC bridges, realized by laser trimming and cutting of a 254 µm thick DuPont 9k7-X sheet.

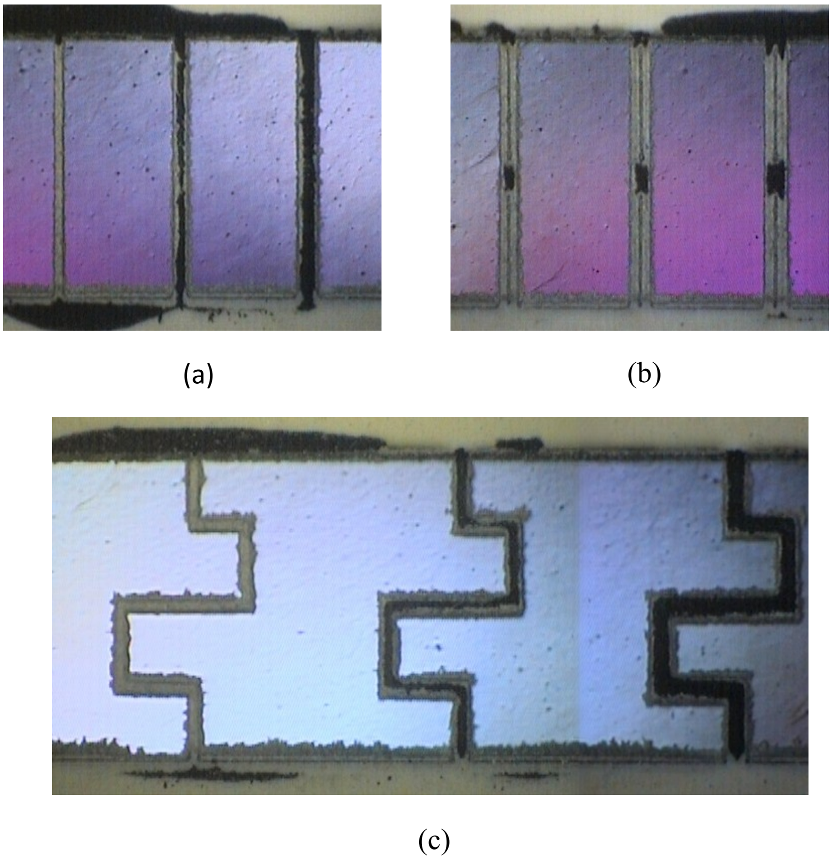

Figure 4.4: Laser machined unfired LTCC bridges with sacrificial graphite-based paste. (a) Straight bridges, (b) double-beam bridges and (c) folded beam bridges.

In order to obtain a truly suspended bridge, the trimmed area was filled with a graphite-based sacrificial paste and the LTCC sheet was dried in an oven at 120°C for 10 minutes before the beam cutting. The beams were cut as described previously and the machined sheet was laminated with another plain sheet in a uniaxial press at 300 psi. Figure 4.4 shows the beams' layer after the application of the sacrificial paste and cutting (before lamination). The obtained block was then fired at 850°C, according to the manufacturer's specifications [155].

From a different design and manufacturing run, Figure 4.5 shows two 4 mm long bridges and a 2 mm length cantilever after firing, demonstrating that suspended structures can be achieved. However, LTCC shrinkage during firing (measured to be 15.75% on average on the *x-y* plane) caused buckling in the suspended bridges. This was more evident for longer bridges.

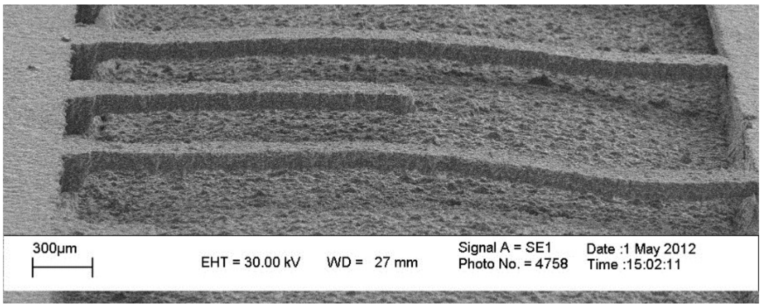

Figure 4.5: SEM micrograph of 4 mm long suspended bridge and 2 mm long cantilever in fired LTCC.

Buckling analysis continued by fabricating straight beams on a single LTCC layer, applying the same laser trimming and cutting process as before. In this case, 4 mm long, 90 μm thick beams having widths of 50, 100 and 150 μm were micromachined and the buckling deformation was measured after firing. The three fabricated beams, illustrated in Figure 4.6 and 4.7, have a measured width of 65, 124 and 165 μm respectively, and show buckling on different planes. The buckling plane is consistent with the direction of minor second moment of area and is caused by differential shrinkage between the laser machined beams and the thicker substrate. For the 165 and 124 µm wide beams, a maximum deflection of 251 and 289 µm is observed, respectively. For the thinner beam in the horizontal plane in-plane buckling is observed, with a maximum deflection of ± 183 µm.

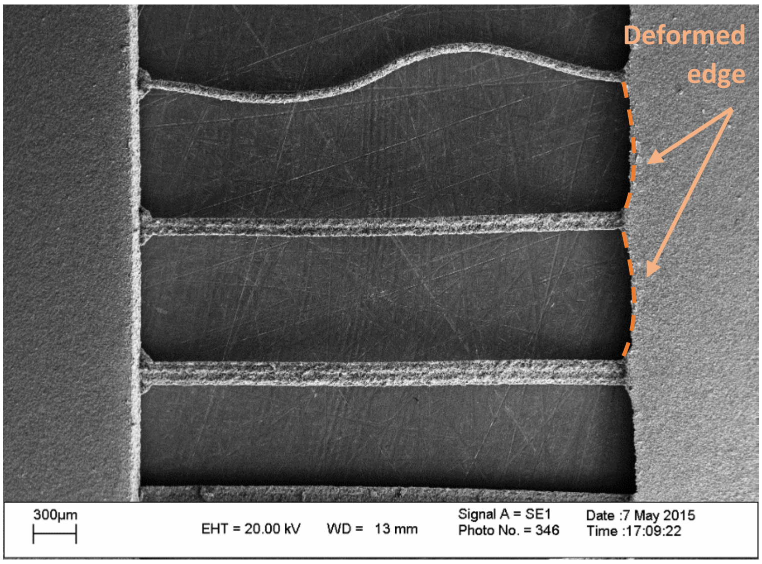

Figure 4.6: Top view of the three 4 mm long bridges showing in-plane buckling. The highlighted curves show the deformation caused by the differential shrinkage, which resulted in the buckled beams.

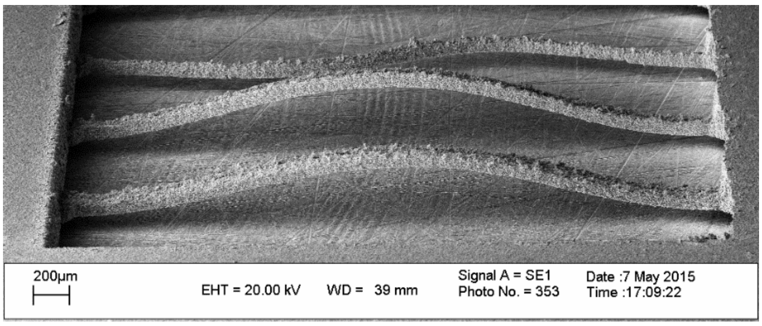

Figure 4.7: Angled view of the three 4 mm long bridges showing out-of-plane buckling.

4.3.1 Beam buckling theory

Before explaining the buckling beam theory, some relevant properties should be introduced. The Young's modulus *E*, also known as elastic modulus and expressed in Pascal (*Pa*), is a mechanical property of linear elastic solid materials defined as the ratio between the tensile stress applied, as force per unit area in [N/m^2], and the extensional strain, as proportional elongation $\Delta L/L_0$. The second moment of area I is a geometrical property of an area and describes how its points are distributed with regard to an arbitrary axis. It is calculated as $\int_A \rho^2 dA$, where A is the area and ρ the distance from the chosen axis and its unit is length to the power of four [m^4]. This geometrical property is of central importance in beam theory.

For a buckled fixed-fixed beam of length L_0 and with distance L between the anchors after buckling, as illustrated in Figure 4.8(a) the displacement v of the beam can be obtained from the solution of the second-order differential equation [156]

$$EIv''(x) + Pv(x) = C_R \tag{4.2}$$

where E is Young's modulus, I is the second moment of area, P [N] is the load and C_R is a coefficient due to the reaction moment at the fixed ends, and has a solution in the form of

$$v(x) = C_1 \sin qx + C_2 \cos qx + C_R \ \text{[m]} \tag{4.3}$$

where $q^2 = P/EI$, and C_1 and C_2 are constants of integration to be evaluated by the boundary and the end conditions of the beam. With the boundary conditions, $v(0) = v(L) = 0$ and $v'(0) = v'(L) = 0$, for a fixed-fixed beam the result is

$$v(x) = 2C_R \sin^2\left(\frac{n\pi x}{L}\right) \ \text{[m]} \tag{4.4}$$

The constant C_R for the fixed-fixed beam can be analytically calculated by solving the line integral along the sinusoidal curve of the buckled beam and equating it to the original length L_0 of the un-bucked beam. Unfortunately, the shrinkage factor of the green tape during firing makes this calculation impractical. However, its value can be empirically found by measuring the maximum displacement.

For a buckled fixed-pinned beam of length L_0 and with distance L between the anchors after buckling, as in Figure 4.8(b), the displacement v of the beam can be obtained from the solution of the second-order differential equation [156]

$$EIv''(x) + Pv(x) = R(L - x) \tag{4.5}$$

where R is the perpendicular reaction at each end and has a solution in the form of

$$v(x) = C_1 \sin qx + C_2 \cos qx + \frac{R}{P}(L - x) \text{ [m]} \tag{4.6}$$

With the boundary conditions, $v(0) = v(L) = 0$ and $v'(0) = 0$ for a fixed-pinned beam the result is

$$v(x) = C_1[\sin(\kappa x) - \kappa L cos(\kappa x) + \kappa(L - x)] \text{ [m]} \tag{4.7}$$

where $\kappa = 4.4934/L$, obtained from the numerical solution of $tan(\kappa L) = \kappa L$ for the boundary condition of $v'(0) = 0$.

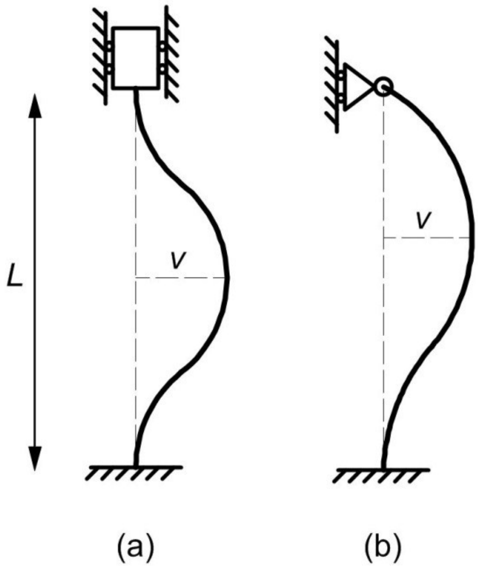

Figure 4.8: Diagram of buckled beams: (a) first-order buckling for a fixed-fixed beam, (b) first-order buckling for a pinned-fixed beam.

4.3.2 Buckled beams measurements

The profiles of the two wider 4 mm long beams were measured with a WYKO Veeco® N9100 optical profiler and the result compared to the curve analytically calculated with (4.4). The results are shown in Figure 4.9 and 4.10.

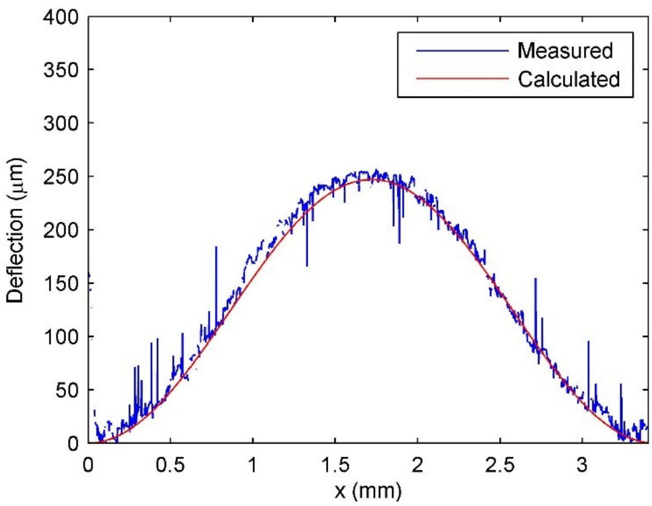

Figure 4.9: Comparison between the measured and calculated profiles for the 164 μm wide buckled beam.

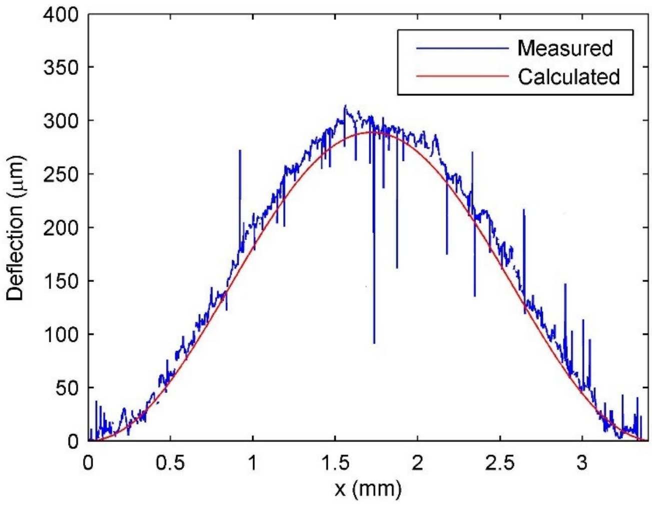

Figure 4.10: Comparison between the measured and calculated profiles for the 124 μm wide buckled beam.

The buckling observed for the thinner beam can only occur for an anti-symmetrical fixed-fixed configuration. In other words, such buckling is obtained if the clamping at both ends has a defect that would force the beam to buckle in opposite directions. The displacement obtained can be analytically evaluated by considering a beam of half the length in a pinned-fixed configuration. Using such an approach, the analytically obtained profile is compared to the measured beam deflection, extracted from the SEM micrograph, and the results shown in Figure 4.11.

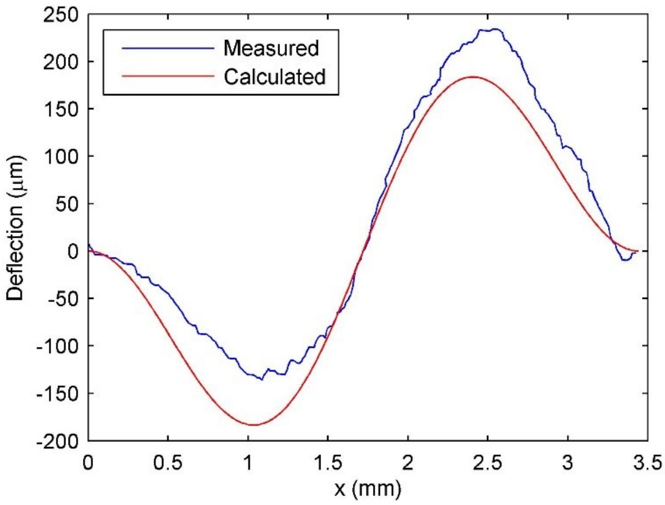

Figure 4.11: Comparison between the measured and calculated profiles for the 65 μm wide buckled beam.

For the buckling of the beams, which occurs during the firing process, the critical minimum load (P_{cr}) to generate buckling in a fixed-fixed beam is given by

$$P_{cr\,f-f} = \frac{4\pi^2 EI}{L^2} \quad [\mathrm{N}] \tag{4.8}$$

While the second moment of area can be easily calculated from the beam cross-section dimensions, the Young's modulus in (4.8) is associated with the LTCC during the sintering process, when shrinkage occurs. Although not feasible to accurately evaluate, it is known that the Young's modulus during sintering is substantially lower than that for the fired LTCC. The reason is that, when shrinkage occurs, the temperature has gone beyond the glass transition point of the material.

Of particular interest is the preferential out-of plane buckling direction, which is in the direction of the laser. This supports the hypothesis that pre-sintering occurs on the trimmed side and shrinkage is limited on the other side of the beam. For clarity, Figure 4.12 illustrates the steps of trimming, shrinkage and buckling of the fired beam. As the darker layer in Figure 4.12(b) is already sintered and cannot shrink further, the shrinkage and compression in the beam can only occur in the lower part, forcing the buckling in the direction of the laser beam.

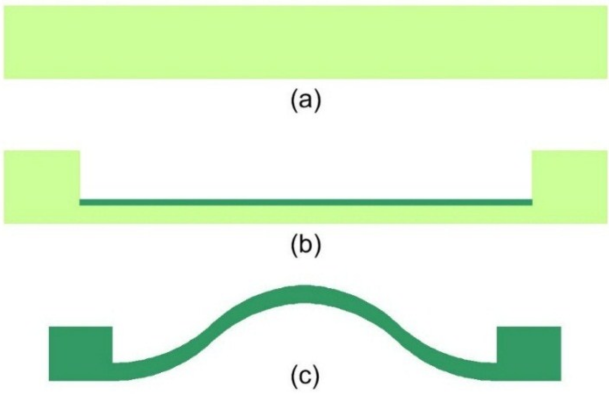

Figure 4.12: Illustration of the LTCC trimming and beam buckling. (a) Full thickness LTCC sheet; (b) trimmed window with layer of pre-sintered LTCC (darker); (c) shrinkage of the LTCC substrate and buckling of the beam.

4.3.3 Stress-releasing designs

With straight bridges only, out-of-plane buckling was observed. Other beams made using the same process demonstrated that stress-releasing structures, such as the folded beams in Figure 4.13, can prevent out-of-plane buckling, but can still be subject to deformation due to spatially non-uniform shrinkage. After the results obtained for the 4 mm (anchor to anchor) long suspended structures, further structures were realized with different shapes to demonstrate possible alternatives for preventing buckling and deformation, as illustrated in Figure 4.14 and Figure 4.15.

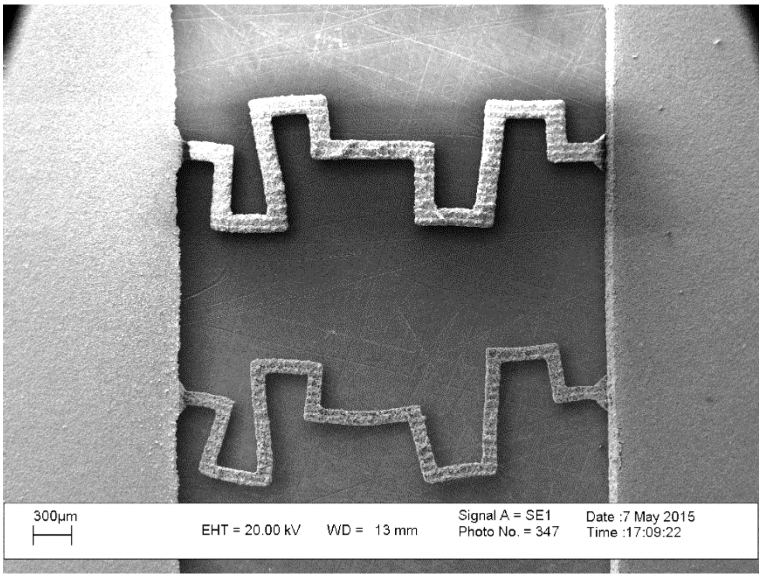

Figure 4.13: Stress-released beams showing distortion due to uneven shrinkage, with no sign of out-of-plane buckling.

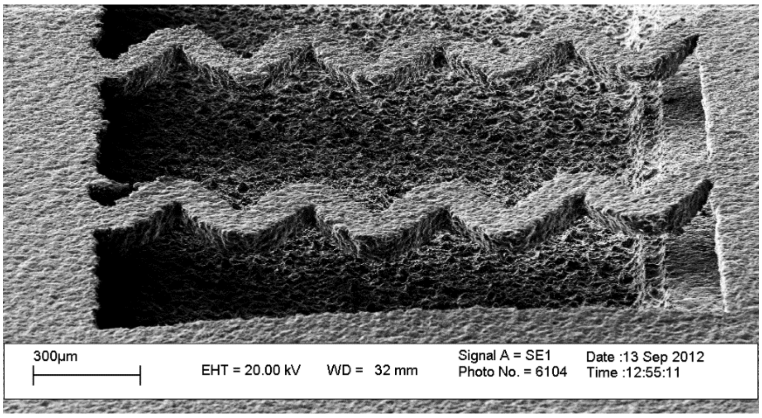

Figure 4.14: SEM micrograph of 2 mm (anchor to anchor) length zig-zag bridge in fired LTCC.

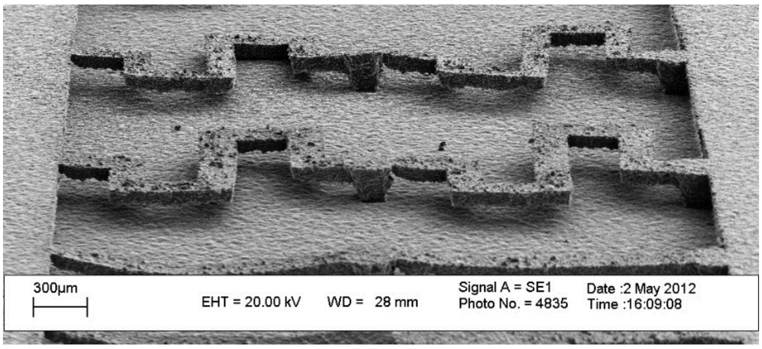

Figure 4.15: SEM micrograph of 4 mm (anchor to anchor) length folded beam bridges with central support in fired LTCC.

4.3.4 Suspended cantilevers intended for actuation

Following the results obtained in the machining of suspended bridges, the next aim was the design and fabrication structures that are intended for actuation. To evaluate the feasibility of fired LTCC suspended beams in electrostatically-actuated MEMS, simulations were performed to predict their actuation voltage as if they were homogeneous materials (this being a gross assumptions, as will be seen later). Cantilevers were chosen, due to their substantially lower spring constant when compared to bridges, requiring a factor of ~8 lower actuation voltage [157].As the measurement equipment available was not able to apply enough pressure to cause a measurable displacement, it was not possible to perform quantitative mechanical tests on the manufactured beams. Therefore, in the numerical simulations, the values of Young’s modulus and Poisson ratio available from the datasheet were used; 145 GPa and 0.25 for the fired LTCC, respectively. A more complete characterization of the material is needed. Because of the brittle nature of sintered ceramic and the large number of grain boundaries, failure by fatigue should also be investigated.

With the LTCC manufacturing process available at Leeds, the smallest gap height was defined by the minimum thickness of 30 µm achievable by the screen printing system. The first suspended structure considered was a cantilever 2 mm long, 100 µm wide and 90 µm thick. From previous productions runs, such cantilever beam showed no evident deformation and, therefore, this was considered as the starting iteration point. For such thin beams, a square top actuation electrode of 0.25 mm^2 (500 x 500 µm) of area at the free end of the cantilever was proposed.

The thickness of the metallization on the actuation pad area was neglected in the numerical simulations, as it would not influence the mechanical behaviour of the beam. The simulated actuation voltage for this structure was impractical at 948 V. Such a high actuation voltage emphasised the need for a larger actuation area and better beam design. After several iterations, the structure with the lowest actuation voltage (within manufacturing limits) was designed as a dual folded beam cantilever with a square actuation top electrode area of 1 mm^2, as illustrated in Figure 4.16. Such a structure has an overall length of 3 mm, a simulated spring constant of 288.54 N/m and a calculated actuation voltage of 372 V.

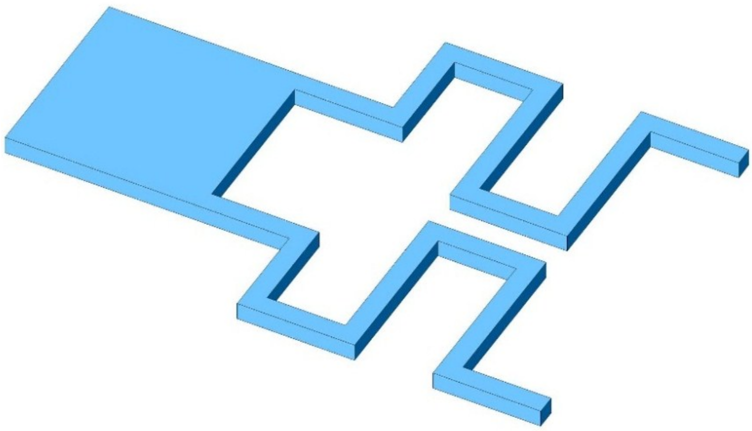

Figure 4.16: Dual folded beam cantilever design.

With all the calculations and simulations, the gap height was considered to be 30 μm. Unfortunately, the extensive fabrication experiments performed by the University of Leeds indicated that it was impossible to control the thickness of the sacrificial paste (which defines the gap) and of the metallisation. Because of this, and the very high actuation voltage, the approach of creating beams from bulk micromachining of LTCC was discarded as a feasible technology for the manufacturing of MEMS.

4.4 Graphite sacrificial paste

In the fabrication process of suspended structures, sacrificial layers play a very important role in supporting the beam and defining its clearance height. In the development of a sacrificial material, several factors need to be taken into account: compatibility with the materials, deposition technique and removal process. In standard LTCC processing, thick film deposition (i.e. screen or stencil printing) represents a common technique for the deposition of materials (i.e. conductive, resistive or dielectric pastes). Indeed, these techniques have been employed for the deposition of sacrificial layers in the form of mineral- or graphite-based pastes [43]–[45]. Of particular interest for their ease of removal during the firing process are graphite-based pastes. The formulation developed and reported by Ryser *et al.* at EPFL [44] contains terpineol and acetone as solvent and dispersant, respectively. When tested on green LTCC, it proved to be very aggressive, dissolving its binder and destroying the substrate if not dried in an oven immediately after deposition. This effect was accentuated when the paste was applied on the trimmed regions. To overcome this, in parallel with the LTCC laser trimming work, a novel formulation was developed using water as solvent and fructose as binder. Water, used in the development process of photoimageable LTCC pastes, (e.g. DuPont Fodel® [158] and Hibridas [159] pastes), does not attack the green LTCC binders. Fructose was used for its very high water solubility and for the way it decomposes at high temperatures. Fructose is a monosaccharide, the simplest form of carbohydrates, and has a chemical composition of $C_6H_{12}O_6$. If fructose is heated in air, at a temperature greater than 600°C, it will decompose into carbon dioxide and water, the reaction being

$C_6H_{12}O_6 + 6O_2 = 6\ CO_2 + 6\ H_2O$. In principle, this leaves no residue on the substrate after the firing process, which reaches a maximum temperature of 850°C. The developed paste is prepared by mixing 2 grams of graphite powder (TIMCAL TIMREX KS10 [160]), with an average particle size of 6 μm and 1 gram of fructose in 10 ml of de-ionised water. The mixture is stirred manually and sonicated at 40°C for 30 minutes in a sealed vial. After application via stencil printing, the paste is dried for 10 minutes on a hotplate at a temperature 80°C. Examples of screen printed graphite paste on LTCC, before and after firing, are shown in Figure 4.17.

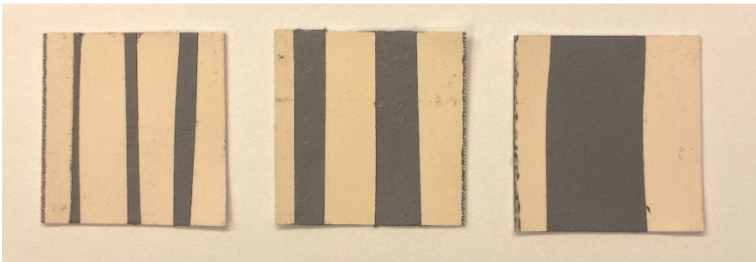

(a)

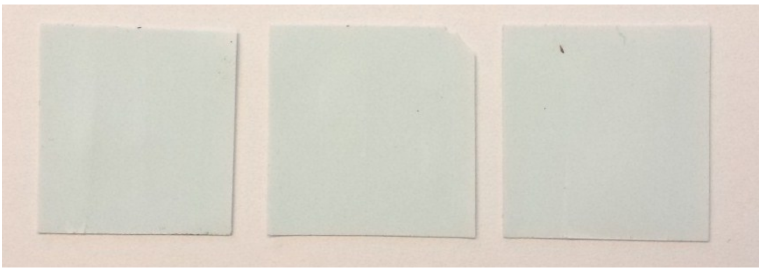

(b)

Figure 4.17: Example of sacrificial graphite paste stencil printed on LTCC (a) before fiding, and (b) after firing.

If the printed paste is further heated at 120°C for 20 minutes, the fructose breaks down and polymerizes, forming longer chains, in the process commonly known as pyrolysis or caramelization in case of saccharides. This procedure would increase the mechanical stability and adhesion of the graphite printed layer, making it also a suitable candidate as a resistive material for the printing of heaters. Experiments were performed by stencil printing tracks of graphite paste on alumina, as shown in Figure 4.18. The resistivity of the layer was measured and for a 50 µm thickness layer an average sheet resistance of 22 Ω/sq was obtained. In Figure 4.19 a fabricated demonstrator heater and its thermal image are shown. The resistance between the two terminals of the stencil printed heater was 134 Ω and tested up to a temperature of 300°C. Although no degradation was observed during measurements, more accurate tests, such as thermal cycling and solvents compatibility, should be performed to evaluate the suitability of the paste for applications in real devices.

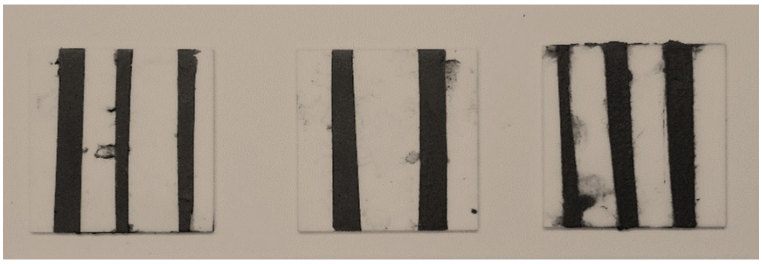

Figure 4.18: Graphite sacrificial paste stencil printed on alumina.

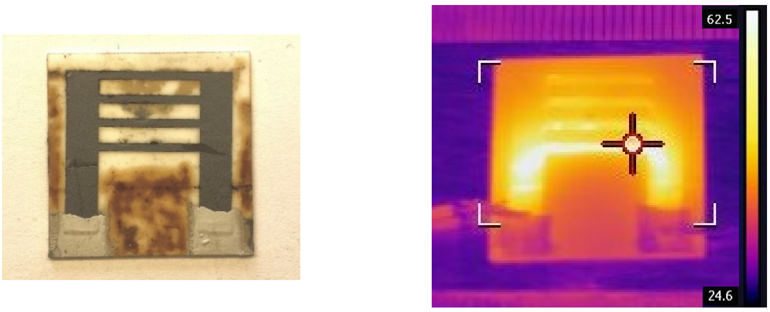

(a) (b)

Figure 4.19: (a) Photograph of the stencil printed heater with contact pads printed with silver paste, and (b) thermal image of the heater. The brown marks on the substrate were caused by the over-heating of the residues of the glue from the adhesive mask used during stencil printing during the curing process on the hotplate.

4.5 Conclusions

In this chapter the laser machining and trimming of green LTCC is studied. Through a multi-step process, feature sizes as small as 65 µm are obtained in the horizontal plane and a repeatable minimum thickness of 90 µm is achieved by laser micro-machining, with surface roughness below 300 nm. After firing, the buckling deformation of the laser machined beams is studied. The results indicate a different shrinkage rate for the beams and the bulk LTCC and show signs of laser-induced pre-sintering. Eventually the formulation of a water-based graphite sacrificial paste is reported. Such paste also showed resistive properties suitable for heating applications.

CHAPTER 5: RF MEMS ELECTROSTATIC ACTUATION

As illustrated in the previous chapter, MEMS employ bridges and cantilevers to enable switches and varactors to be implemented. Different techniques have been used for the actuation of MEMS bridges and cantilevers, including electrostatic and magnetic attraction, thermal expansion, or piezoelectric actuation, to obtain beam displacement [161]–[163]. The most common technique is electrostatic actuation. The reason is that even though high voltages are required, there is almost no current; requiring virtually no control power to hold the structure in its "actuated" state. In this chapter, a new and more accurate model for cantilever electrostatic actuation is presented and compared with the textbook model, showing an improvement prediction in actuation voltage when compared to numerical modelling.

5.1 Cantilever beam spring constant calculation

Before explaining the actuation mechanism, it is important to introduce some basic concepts of beam theory for rectangular cross-section cantilever beams. In particular, the value of spring constant under different load conditions is a fundamental parameter to calculate, as both the beam reaction force and the actuation voltage are a function of spring constant.

The spring constant of a cantilever beam can be derived from its deflection at the tip, through Hooke's law

$$F = k\delta \ \ [\mathrm{N}] \tag{5.1}$$

where F is the applied load, k is the spring constant and δ is the mechanical deflection.

Consider a beam with length l, width w and thickness t loaded at the free end, as illustrated in Figure 5.1, the deflection at any point along this beam is described by [156]

$$\delta(x) = \frac{Fx^2}{6EI}(3l - x) \ \text{[m]} \tag{5.2}$$

where $\delta(x)$ is the deflection at x, E is the Young's modulus of the beam's material and I is the second moment of area, which is defined as

$$I = \frac{wt^3}{12} \ [\text{m}^4] \tag{5.3}$$

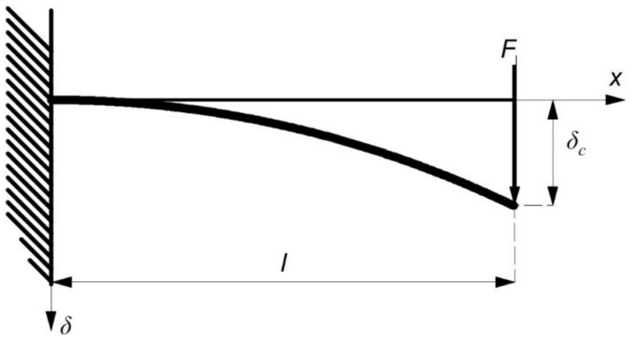

Figure 5.1: Illustration of beam deflection with a concentrated load at the free end.

For $x = l$, (5.2) gives

$$\delta_c = \frac{Fl^3}{3EI} \ \text{[m]} \tag{5.4}$$

where δ_c is the maximum deflection for a concentrated load applied at the free end. When the width of the beam $w > 5t$ the equivalent Young's modulus $E_{eq} = E/(1- v^2)$ should be used, where v is the Poisson ratio.

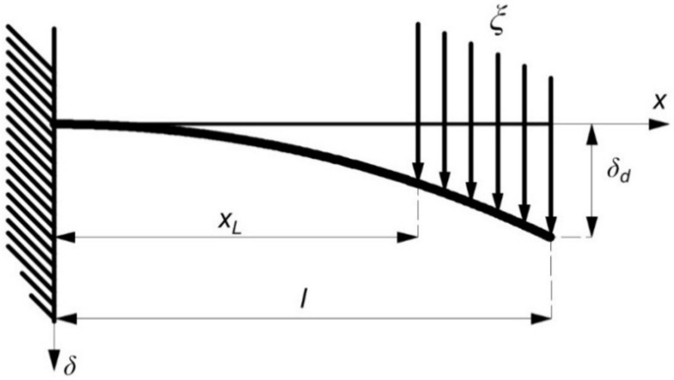

Figure 5.2: Illustration of beam deflection with a distributed load.

For a beam with a distributed load, from x_L to l, as shown in Figure 5.2, the displacement δ_d at the free end can be calculated by integrating (5.2) from x_L to l

$$\delta_d = \int_{x_L}^{l} \frac{\xi x^2(3l - x)}{6EI} dx \quad [\mathrm{m}] \tag{5.5}$$

where ξ represents the load per unit length, giving a total load $F = \xi(l - x_L)$.

In this case, the displacement at the free end is given by

$$\delta_d = \frac{Fl^3}{24EI} \frac{3 - 4(x_L/l)^3 + (x_L/l)^4}{1 - (x_L/l)} \quad [\mathrm{m}] \tag{5.6}$$

Substituting (5.4) and (5.6) into (3.1) gives the spring constant for the concentrated load k_c and distributed load k_d, respectively.

$$k_c = \frac{3EI}{l^3} \quad [\mathrm{N}/\mathrm{m}] \tag{5.7}$$

$$k_d = 8k_c \frac{1 - (x_L/l)}{3 - 4(x_L/l)^3 + (x_L/l)^4} \quad [\mathrm{N}/\mathrm{m}] \tag{5.8}$$

Similarly, for a triangular load distributed along the whole length of the cantilever, shown in Figure 5.3, it can be shown that displacement at any point along the cantilever and the maximum displacement are given by

$$\delta(x) = \frac{Fx^2l^2}{60EI}(20 - 10(x/l) + (x_L/l)^3) \text{ [m]} \tag{5.9}$$

$$\delta_t = \frac{11\mathrm{F}l^3}{60\mathrm{EI}} \text{ [m]} \tag{5.10}$$

where $F = \xi_0 l/2$ and ξ_0 is the maximum load at the free end of the cantilever. The spring constant can then be obtained by

$$k_t = \frac{60EI}{11l^3} \ [\mathrm{N/m}] \tag{5.11}$$

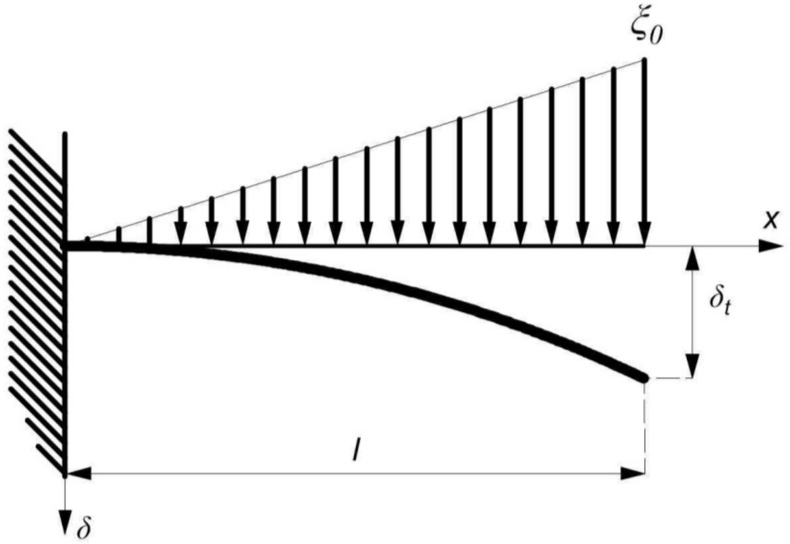

Figure 5.3: Illustration of beam deflection with a triangular load.

5.2 Cantilever beam electrostatic actuation

To calculate the actuation voltage for electrostatically actuated beams, the model described in [28] is commonly used. In this subsection, this model is reproduced and the principles of electrostatic actuation explained. An example of an electrostatically actuated cantilever is illustrated in Figure 5.4.

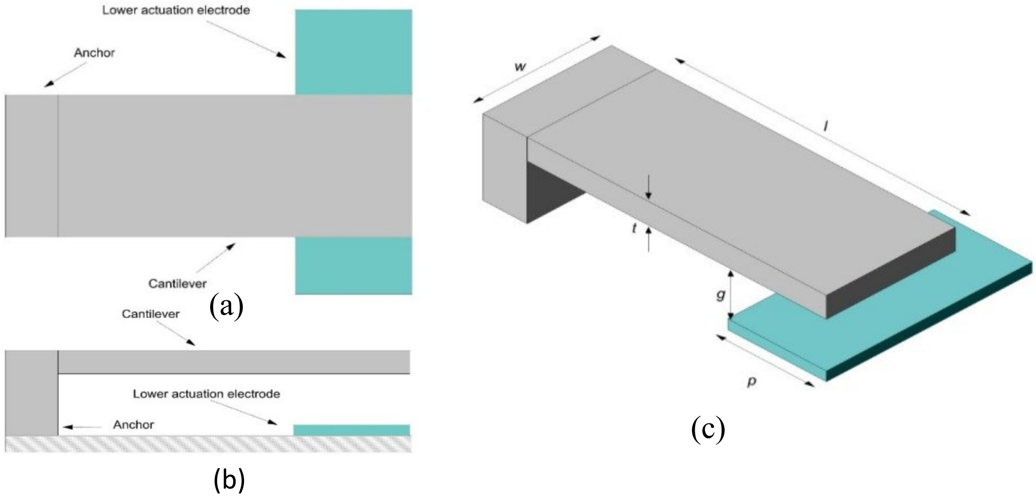

Figure 5.4: (a) Top view, (b) side view and (c) isometric view of a cantilever with fixed actuation electrode.

By applying a potential difference between the fixed actuation electrode and the conducting beam, the resulting electrostatic force F_e that attracts the beam towards the lower electrode on the substrate can be expressed as [17]

$$F_e = \frac{1}{2}V^2\frac{dC(g)}{dg} = -\frac{1}{2}\frac{\varepsilon_0 A V^2}{g^2} \text{ [N]} \tag{5.12}$$

where

$$C(g) = \frac{\varepsilon_0 A}{g} \text{ [F]} \tag{5.13}$$

is the capacitance between the two electrodes, ε_0 is the permittivity of vacuum, $A = wp$ is the overlapping area of the beam and the electrode (as illustrated in Figure 5.4), g and V are the gap height and voltage applied between them, respectively. The ideal electromechanical model used here is of a parallel plate capacitor with fixed and moveable plates, as illustrated in Figure 5.5; fringing field are assumed to be negligible with $g \ll (w, p)$.

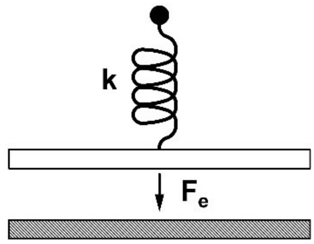

Figure 5.5: Electromechanical model of an electrostatically actuated MEMS.

As the beam moves towards the electrode, it is subject to an increasing electrostatic force, until a balance is obtained between the electrostatic attraction and the beam's restoring force F_r [28], described by

$$F_r = k(g_0 - g) \equiv F_e \tag{5.14}$$

where g_0 is the maximum gap height.

Solving (5.14) for voltage one arrives at the following textbook expression [5]

$$V(g) = \sqrt{\frac{2k}{\varepsilon_0 A} g^2 (g_0 - g)} \quad [\mathrm{V}] \tag{5.15}$$

Figure 5.6 plots gap height against applied voltage, giving two possible beam positions for every applied voltage, caused by the positive feedback of the attraction force F_e. After the gap height reaches $g = (2/3)g_0$, the increase in F_e is higher than the increase in restoring force F_r, which results in the instability of the beam distance and collapse of the actuated state.

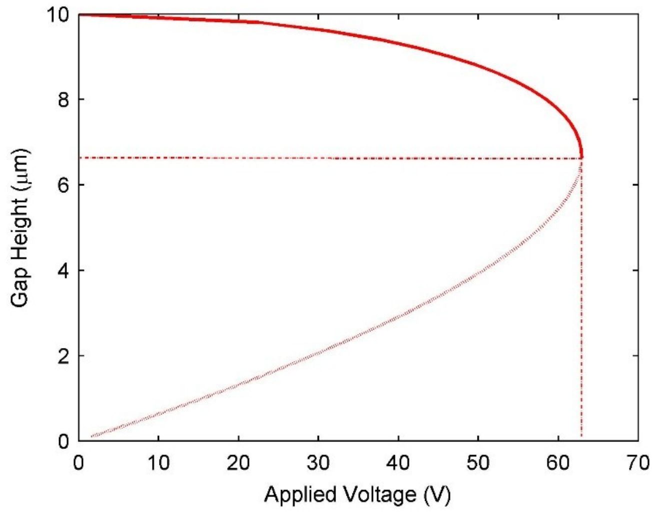

Figure 5.6: Cantilever height versus applied voltage with w = 200 μm, p = 500 μm, g_0 = 10 μm, t = 13 μm, l = 1000 μm and k = 9.74 N/m (for aluminium). Calculated pull-down voltage is 62.9 V. The dotted line represents the unstable region.

The point of instability can be calculated by setting the derivative of (5.15) with respect to the gap g to zero; the value of g at which the instability occurs is found to be exactly two-thirds of g_0. For example, the plot in Figure 5.6 is for an aluminium cantilever (E = 69 GPa). Therefore, the corresponding "pull-down" or "pull-in" voltage is found to be given by the well-known expression

$$V_p = V\left(g = \frac{2g_0}{3}\right) = \sqrt{\frac{8kg_0^3}{27\varepsilon_0 A}} \quad [\mathrm{V}] \tag{5.16}$$

With (1.13), the thickness and permittivity associated with a thin dielectric layer on top of the lower electrode have been neglected. However, if the dielectric layer needs to be considered, the value of capacitance $C(g)$ needs to include the capacitance due to the dielectric in series with the capacitance in air. For a layer of dielectric of thickness d, the associated capacitance is $C_d = \varepsilon_0 \varepsilon_r A/d$, giving a total capacitance value of [164]

$$C(g) = \frac{\varepsilon_0 A}{g + d\left(\frac{1}{\varepsilon_{\mathrm{r}}} - 1\right)} \quad [\mathrm{F}] \tag{5.17}$$

However, for calculating the "hold-down" voltage required to hold the beam in its actuated position, the dielectric needs to be taken into account. There are other factors that should also be considered, such as stiction and the roughness of the electrodes. As a first approximation, a reasonable assumption is that the beam will follow in its fully actuated position if the applied voltage creates a force greater or equal to the beam restoring force [28]. The effect of the fringing field can be included by considering an effective beam width w_{eff} in the calculation of the area A [165].

$$w_{eff} = w + 0.65(g_0 - g) \tag{5.18}$$

The cantilever structure considered here can be used to perform both switch and variable reactor (varactor) functionalities. Indeed, for any applied voltage lower than the actuation threshold (i.e. pull-down voltage), the resulting displacement of the beam causes a change in the capacitance between the electrodes.

5.3 Other models for actuation voltage prediction

Several alternative models have been developed for the derivation of a closed-form equation, for a more accurate prediction of the actuation voltage of cantilevers. In [166] several other different models are employed in the calculation of the capacitance value of the parallel plate capacitor. Ideally, these should include fringing field capacitance, which can include the finite thickness and external faces of the electrodes. However, due to the parallel plate geometry, an arbitrarily chosen correction factor is needed to match the numerical simulations results. In [167] a model involving the cantilever deflection in the calculation of the electrostatic force is reported. This model, which uses a non-uniform distribution of force along overlapping area between the cantilever and the fixed electrode, provides good predictions of the pull-down voltage with an error within 3%. Nevertheless, it makes use of a single empirically determined deflection curve obtained from numerical simulations for all load conditions. In the following subsection a more rigorous approach is considered for the prediction of the pull-down voltage and two cantilever deflection profiles are illustrated for different fixed electrode length and cantilever length ratios.

5.4 Improved model for the actuation voltage calculation

The textbook model represents a good approximation when the length of the cantilever is 2 to 3 orders of magnitude larger than the maximum cantilever displacement. However, when the beam displacement exceeds this amount, the parallel-plate capacitor approximation becomes invalid and the actual profile of the beam has to be taken into account. Having said this, a capacitive membrane switch can be realized by exploiting the low capacitance when there is no actuation voltage and the high capacitance when snap-down occurs. Figure 5.7 shows the structure and variables used for the following calculations.

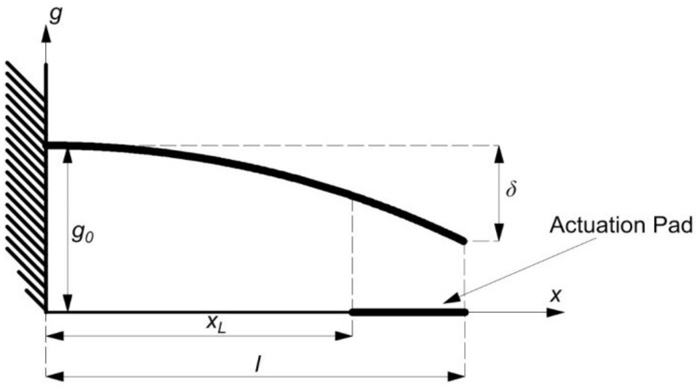

Figure 5.7: Illustration of beam deflection under electrostatic actuation.

In order to obtain a more accurate model, the capacitance between the fixed actuation electrodes has to be calculated according to the deflected shape of the cantilever. Therefore, its profile over the fixed actuation electrode needs to be found. Substituting the spring constant in (5.7) and Hooke's law, with $\delta = \delta_c = (g_0 - g)$, into (5.2), the displacement $\delta(x)$ can be rewritten as

$$\delta(x) = \frac{k_c \delta (3l - x) x^2}{2 k_c l^3} = \frac{(g_0 - g)(3l - x) x^2}{2 l^3} \text{ [m]} \tag{5.19}$$

The displacement along the beam is now independent of the spring constant and expressed only as a function of its length and maximum displacement. With the known profile of the cantilever, the distance $g(x)$ can be obtained as $g(x) = g_0 - \delta(x)$. The function found is then used to calculate the capacitance per unit length as

$$dC = \frac{\varepsilon_0 w}{g(x)} dx \text{ [F]} \tag{5.20}$$

Assuming the dimensions of overlapping surface area of the two electrodes is much larger than the separation gap, the electrostatic force between them can be calculated by integrating the force per unit length

$$F_e = \int_{x_L}^{l} \left(\frac{\varepsilon_0 w}{g(x)} dx\right)^2 \frac{V^2}{2\varepsilon_0 w\, dx} = \int_{x_L}^{l} \frac{\varepsilon_0 w V^2}{2(g(x))^2\, dx} dx \ \text{[N]} \qquad (5.21)$$

The relationship between the applied voltage and gap g can be obtained by combining (5.20) and (5.21) and equating to the reactive force given by Hooke's law.

$$V(g) = \frac{\sqrt{2k_d \varepsilon_0 w(g_0 - g)}}{C(g)} \ \text{[V]} \qquad (5.22)$$

where $C(g)$ is the total capacitance given by the integration dC over the interval (x_L, l) The spring constant k is replaced by the distributed load k_d here, as given in (5.8). In this chapter this model will be regarded as the uniformly distributed load model.

For the same cantilever beam, the results obtained with the textbook and uniformly distributed load models, are compared with those obtained through numerical simulations (using COMSOL Multiphysics®) and shown in Figure 5.8. It shows good agreement between the improved model and the simulation, with a predicted actuation of 76.6 V against the simulated 76.9 V.

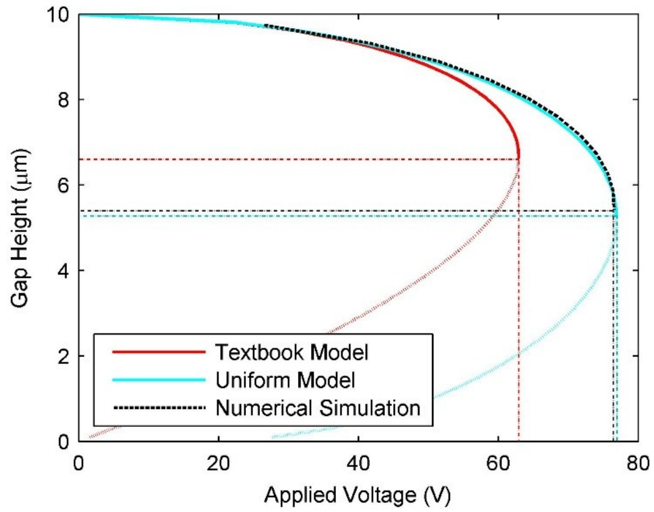

Figure 5.8: Gap height against applied voltage for the standard and the improved model, compared with COMSOL Multiphysics simulation results.

The model derived here gives accurate predictions of the pull-down voltage when the length of the fixed electrode $p < 0.6l$ due to the approximation of the deflection profile, considered as the one for a concentrated load at the tip. When the fixed electrode is longer than 0.6 times l, the model for a triangular distribution of load on the whole length of the cantilever gives a more accurate prediction respect to the previous model. In this case the cantilever profile $g(x)$ obtained from (5.9) and the spring constant k_t in (5.11) will be used.

To prove the validity of the improved uniformly and triangular distributed models, the predicted pull-down voltage when compared to textbook model predictions were compared with numerical simulations for different gap and cantilever length ratios. The results are given in Table 5.1 for an aluminium cantilever with width w = 200 µm, thickness t = 13 µm, gap g_0 = 10 µm and electrode length p = 500 µm.

Table 5.1: Predicted pull-down voltage for different cantilever lengths using the textbook model, the new model and numerical simulations.

Electrode-cantilever length ratio	Cantilever Length, μm	Pull-down Voltage, V			
		Textbook model	Uniform model	Triangular model	Numerical simulation
0.9	550	192.3	272.4	260.4	242
0.77	650	138.7	187.6	180.6	175
0.67	750	105.8	137.9	133.5	132.2
0.5	1000	62.9	76.6	75.1	76.6
0.4	1250	42.8	50.2	49.4	51.7
0.33	1500	31.6	36	35.5	37.4
0.25	2000	19.7	21.7	21.5	22.9

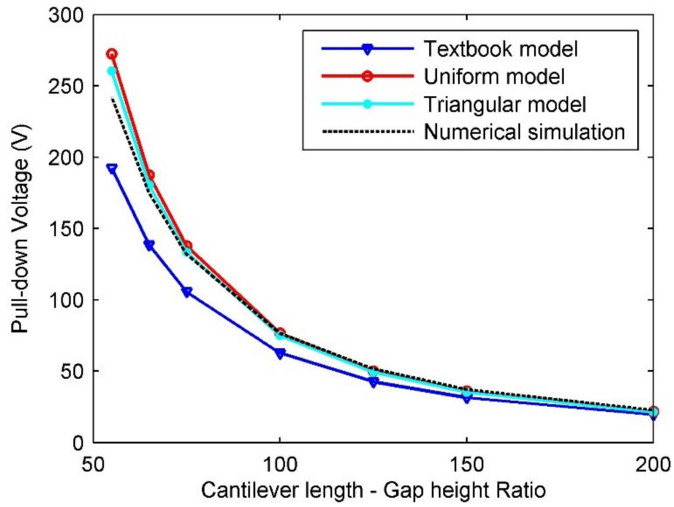

Figure 5.9: Comparison between the predicted pull-down voltage against cantilever length – gap height ratio, using the textbook model, improved model and numerical simulations.

In Figure 5.9, it can be seen that the improved models always provide a better prediction when compared to the textbook model. Across the range considered, the latter provides best-case error of 16%, while one of the triangular distributed model has a worst-case error of 7%, as shown in Figure 5.10. This error can be further reduced if the force is considered to have a trapezoidal distribution on the portion of cantilever above the fixed electrode. However, while being more rigorous, this would only give marginally improved predictions.

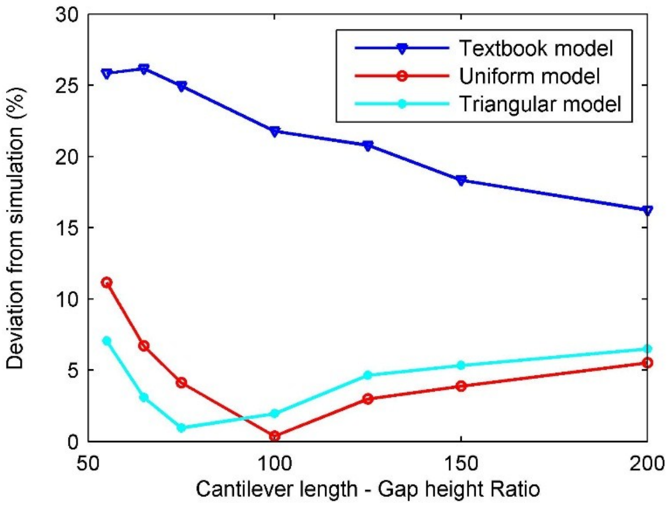

Figure 5.10: Percentage error from the numerical simulation for the textbook and improved models.

This more accurate model provides a powerful tool for the design of cantilever MEMS. The good agreement between the simulation and this closed-form analytical solution demonstrates the validity of this methodology, which only requires a fraction of the computational cost respect to finite element simulation.

The results obtained with the uniformly and triangular distributed load models are then compared to the ones reported in [167]. In this case a cantilever of dimensions l = 200 μm, w = 50 μm and t = 3 μm, with Young's modulus of 57 GPa and Poisson ratio of 0.33 is considered. The maximum gap height is fixed at 2 μm and the length of the fixed electrode varies between 5% and 100% of the length of the cantilever. The comparison results for pull-down voltage and error against numerical simulations are shown in Figure 5.11 and 5.12, respectively, where it can be noticed that the model reported in [167] has a very good fit with the numerical simulation results. The figures also highlight the transition point at an electrode length - cantilever length ratio of 0.6 for the uniform and triangular distributed load models.

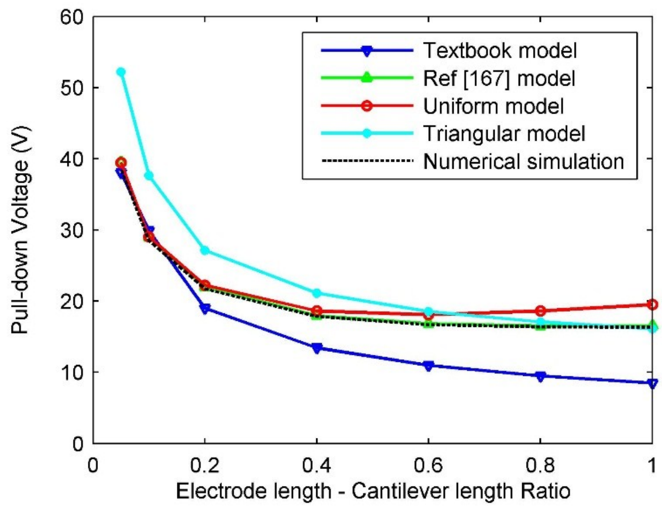

Figure 5.11: Comparison between the predicted pull-down voltage against electrode length - cantilever length ratio, using the textbook model, the two improved models, the model reported in [167] and numerical simulations.

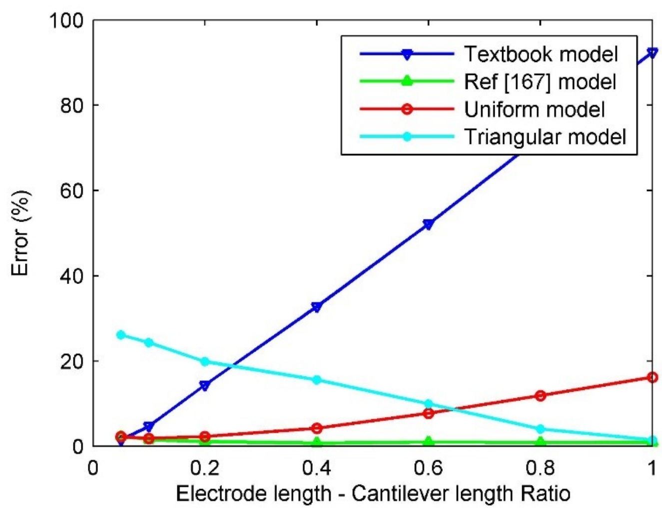

Figure 5.12: Percentage error from the numerical simulation for the textbook model, the two improved models, for the model reposted in [167].

5.5 Conclusions

In this chapter an originally formulated analytical solution in closed form for the calculation of the pull-in voltage for electrostatically actuated cantilevers is reported. The solution proposed, with its related model, is able to give more accurate predictions respect to a widely accepted textbook model with an error lower than 7% respect to numerical simulations for the cases analysed. The developed model and solution are then compared with another model later found in the open literature. This model gives even more accurate results, but it is based on a cantilever deflection profile obtained by numerical simulations. The model here developed, however, is more rigorous and based on beam theory analysis.

CHAPTER 6: HYBRID LTCC-FOIL MEMS

From lessons learnt fabricating structures that could potentially be actuated using micromachined LTCC, it was decided to change materials and assembly processes to implement real electrostatically actuated MEMS on LTCC. In this chapter two approaches for the manufacturing of cantilever MEMS will be considered. These techniques rely on the laser bending of aluminium and thin-film photoresist-based assembly, respectively.

6.1 Laser bent Aluminium foil cantilever MEMS

In standard MEMS technology, the separation gap between the actuation electrodes is defined via a sacrificial layer. However, as explained previously, this approach was not considered viable for integration in LTCC processing. Moreover, the high Young's modulus of LTCC and the minimum thickness repeatably achievable via laser trimming would not allow the manufacturing of a practical switch. In order to solve these problems, aluminium (Al) foil was employed as the cantilever material. The use of laser bending with metals allows the beam to be deformed into the desired shape.

6.1.1 Laser bending

Laser bending technology, also known as laser forming, employs the introduction of thermal-induced stress into the material to cause a controlled deformation of the part; this was originally developed for rapid prototyping applications [168].

This technique, similar to laser surface heat treatment, involves the scanning of a de-focused laser beam on the surface of the object to bend; usually metal foil. An illustration of the process is shown in Figure 6.1.

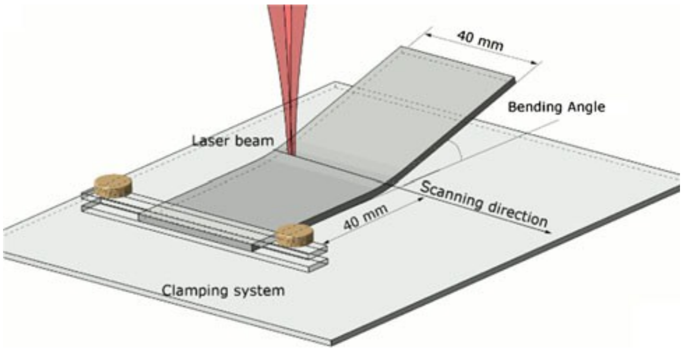

Figure 6.1: Illustration of straight line laser bending process [169].

In the open literature, it is possible to find several studies of this process, such as experimental studies, analytical models, stress, thermal and accuracy analysis [169]–[174]. The use of this process has also been reported for high precision adjustments of silicon micro-cantilevers for sensing applications [175], [176]. While the laser bending is mostly used to create concave bends, as shown in Figure 6.1, it should be noted that, under specific conditions, it is also suitable for the introduction of convex bends (i.e. away from the laser). These conditions include pre-bending, pre-straining or laser-induced buckling of constrained samples [171], [177].

In a study by Ocaña *et al.* laser bending of thin metal foils was suggested as a suitable technique for the manufacturing of MEMS [178] and, more recently, Robben *et al.* developed an active frequency selective surface using stainless steel foil [179] that was laser machined, bent and could be electrostatically actuated.

6.1.2 Laser-bent cantilevers

With laser bending, the conventional structure of a cantilever MEMS can be simplified. Figure 6.2(a) illustrates a conventional cantilever MEMS structure and Figure 6.2(b)-(c) show the laser-bent cantilever MEMS fabrication process. It can be seen that with this alternative manufacturing technique the gap distance is not defined via a sacrificial layer and also the spacer layer at the anchor point is no longer needed.

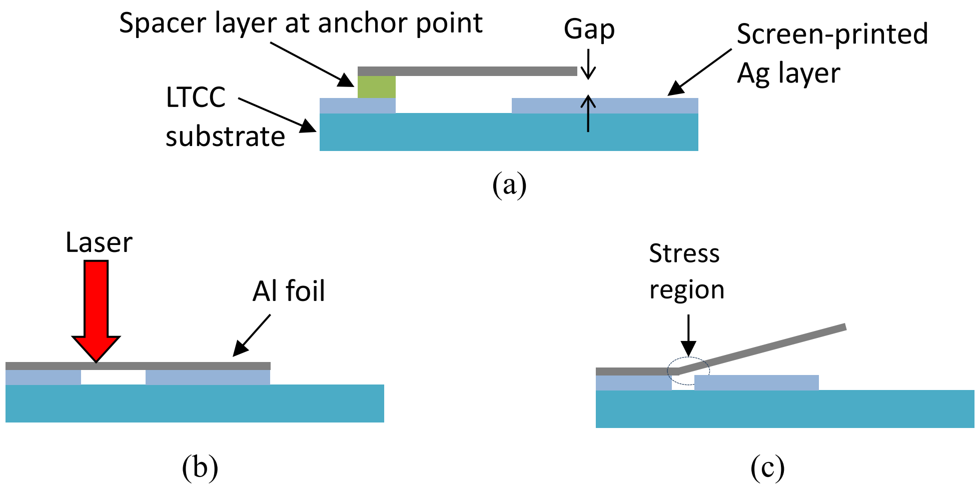

Figure 6.2: (a) Conventional MEMS cantilever; (b) Alternative cantilever structure before laser treatment and (c) post-laser treatment.

In this process the gap distance is defined by the aluminium cantilever bending angle. The actuation voltage is applied between the conducting cantilever and the bottom fixed electrode. Unlike the conventional structure, the gap is not constant along the length of the cantilever and increases progressively. For this reason the minimum gap distance near the edge of the fixed actuation electrode, where the electrostatic actuation force is greater, is particularly important. Any variation in the bending process would cause a change in the bending angle and, therefore, of the gap distance; with increasing error along the length of the cantilever. To reduce the effect of manufacturing tolerances in the bending process, the fixed electrode needs to be as close as possible to the anchor, leaving only the distance needed for the laser bending.

However, once the minimum gap distance is fixed, positioning the bottom actuation electrode closer to the cantilever anchor caused the cantilever to have a steeper bending angle and, therefore, a very large gap distance at its free end. The obvious consequence is an increase in the actuation voltage. For the same reason, having a larger overlapping area, by increasing the length on the cantilever, has only limited advantages. To overcome this issue the spring constant of the cantilever was reduced by removing material in the bending area. Figure 6.3 and 6.4 show the top and side view for the designed laser bent cantilever MEMS, respectively, with all the dimensions.

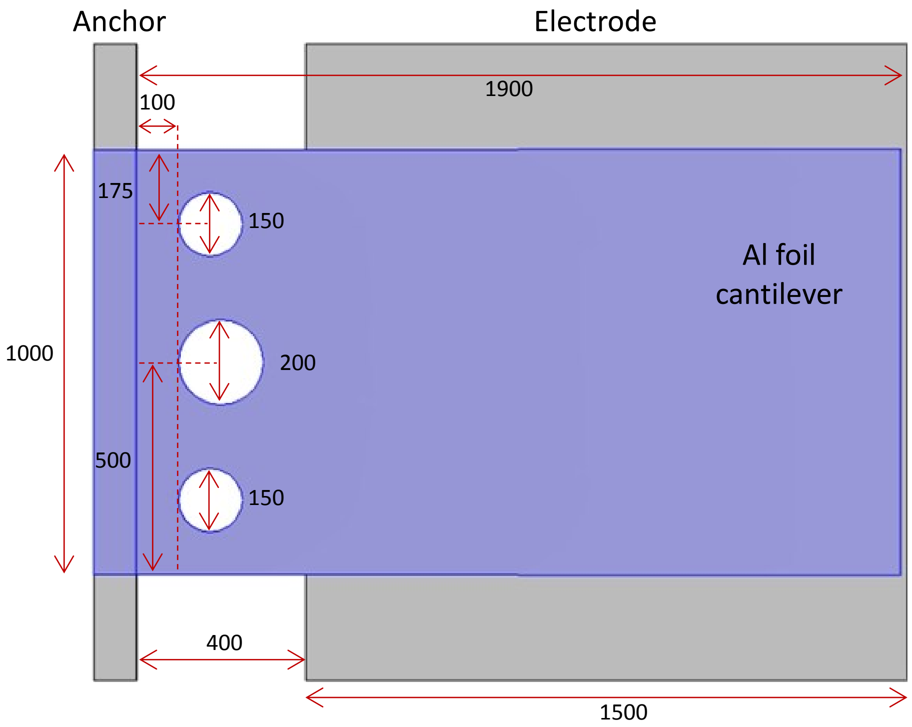

Figure 6.3: Top view of the laser-bent aluminium foil cantilever.

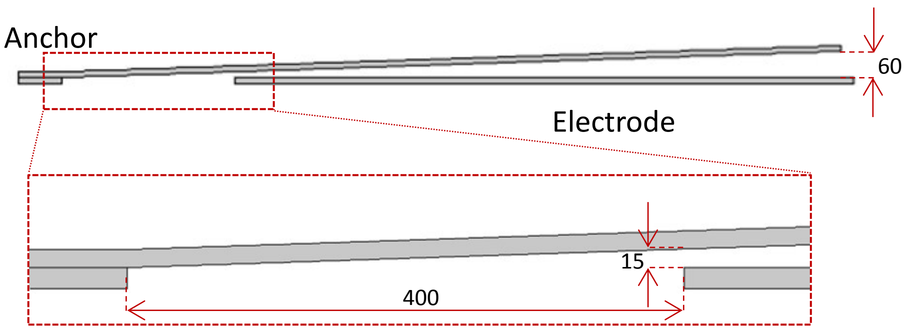

Figure 6.4: Side view of the laser-bent aluminium foil cantilever.

The designed cantilever is 1 mm wide and 1.9 mm long and 13 µm thick, with a bending angle of 1.7° and a bending region 400 µm long, defining a minimum gap height of 15 µm. With this ideal configuration the fixed electrode is 1.5 mm long and at the free end the gap height is 60 µm. Numerical simulations for the designed cantilever show a predicted actuation voltage of 180 V with such a structure. As the aluminium foil is electrically conducting, this cantilever can be used as a switch. In this case, the cantilever MEMS is directly positioned between the ground plane and the signal line on a coplanar waveguide (CPW), to act as an RF shunt switch, as illustrated in Figure 6.5. For such devices, self-actuation (due to high RF signal power levels) is expected to occur above $\frac{(180\,V)^2}{50\,\Omega} = 648\,W$ of power [180]; representing no practical limitation for LTCC.

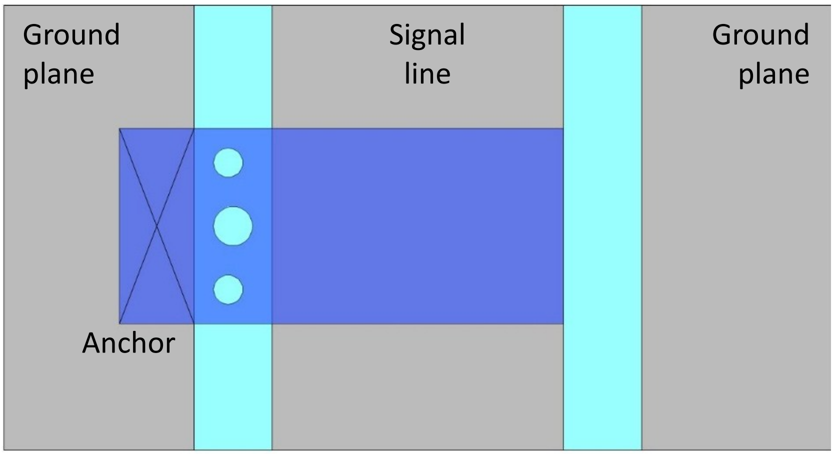

Figure 6.5: Laser-bent cantilever on CPW line in shunt switch configuration.

In this configuration, the actuation voltage is applied between the ground plane and signal line metallization on the LTCC substrate. With this first design iteration, the system does not include the dielectric layer (usually found on the fixed electrode) and the cantilever is acting as an ohmic contact shunt switch. However, such thin dielectric layers can be easily added, without detrimental effects on the behaviour of the switch, which would then act as a capacitive shunt switch.

Further applications include the use of this cantilever as a variable capacitor (varactor). Numerical simulations show a zero-bias capacitance of 456 fF, rising to 565 fF, equivalent to a 24% increase or 11% frequency tuning ratio, for an applied voltage of 175 V. Larger capacitance values can be obtained by increasing the width of the cantilever, without influencing the actuation voltage and, therefore, the tuning voltage or the range percentage.

6.1.3 Fabricated cantilever switches

Based on this design, proof-of-concept samples were fabricated at the University of Leeds. The cantilevers, which were positioned between the ground plane and the signal line of a CPW, as previously illustrated in Figure 6.5, were fixed using ultrasound wedge bonding. The CPW line section was designed to have an impedance of 50 Ω with two tapered transitions at the ends to allow measurements with a 200 μm pitch ground-signal-ground probe. Twelve 10 mm long sections of CPW line, arranged in a 3×4 matrix, were created on a 50×50 mm, four layer thick (~1 mm) LTCC substrate. For the metallization, a 33×33 mm, 30 μm thick square area is screen printed with silver paste (DuPont LL612 [181]) and then the twelve line sections are patterned via laser machining, before firing. The dimensions of the individual CPW line sections are illustrated in Figure 6.6. Note that the wrap-around ground straps were accidentally removed during the manufacturing process.

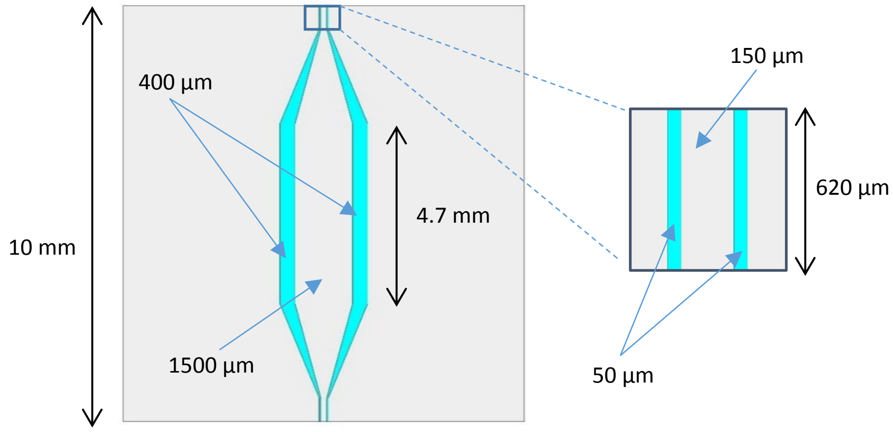

Figure 6.6: CPW line section with dimensions.

On the LTCC substrate, a design variation was also implemented to increase the electrodes overlapping area with little effect on the spring constant, by the introduction of flared cantilevers. With these modified cantilevers, the bent section (representing the major contribution to the spring constant of the cantilever) is only marginally wider. The advantage is an approximately 33% increase in the overlapping area, resulting in an overall predicted actuation voltage reduced by approximately the same percentage. In order to have a greater number of devices to test, and to compensate for the asymmetric nature of the cantilever structure with respect to the CPW, two cantilevers were applied per line section. Moreover, based on these two designs, shorter symmetric cantilever structures were also implemented. Two of the twelve CPW line sections were left empty, to be used as a reference. The designed and manufactured foil cantilevers on CPW are shown in Figure 6.7. From the microscope photographs in Figure 6.8 of the two cantilever designs, it is possible to see the darker laser induced stress region and the wedge bonding spots used to fix the foil to the ground plane.

Unfortunately manufacturing limitations at the University of Leeds prevented the machining of the three holes to increase the cantilever compliance.

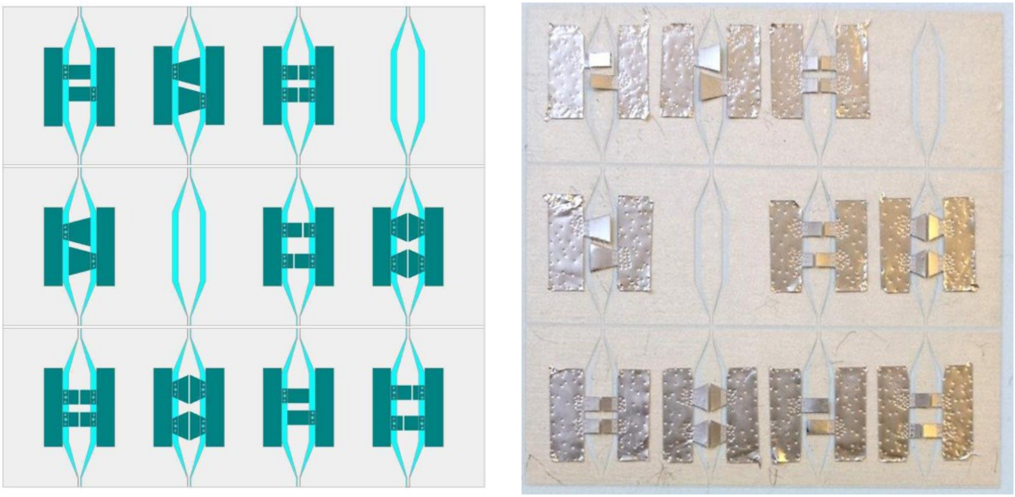

(a) (b)

Figure 6.7: (a) Design layout and (b) fabricated twelve CPW line sections and cantilevers on LTCC.

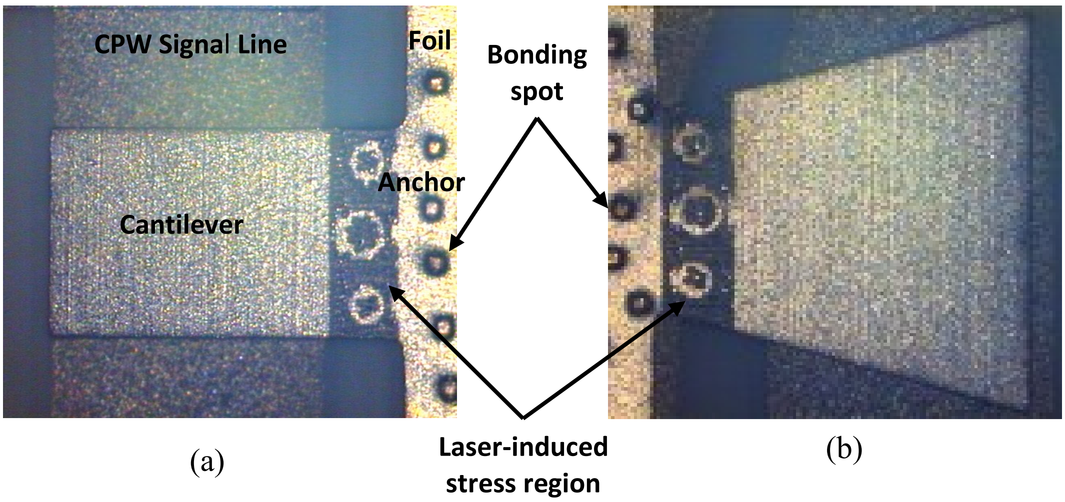

(a) (b)

Figure 6.8: Microscope photograph of (a) a rectangular cantilever and (b) a flared cantilever.

After measurements under the microscope it was found that beyond the missing holes, the fabricated cantilevers did not reflect the designed ones. Irregularities in the anchor area caused an initial gap between the ground plane and cantilever, and the laser-induced stress caused larger bending angles than expected. Both these defects increase the gap between the cantilever and the bottom electrode, therefore, also increasing the actuation voltage. The measured cantilever heights at the anchor (point I), at the end of the laser-induced stress area (point II) and at the free end (point III), as illustrated in Figure 6.9, are reported in Table 6.1. The analysis focused on the full length cantilevers.

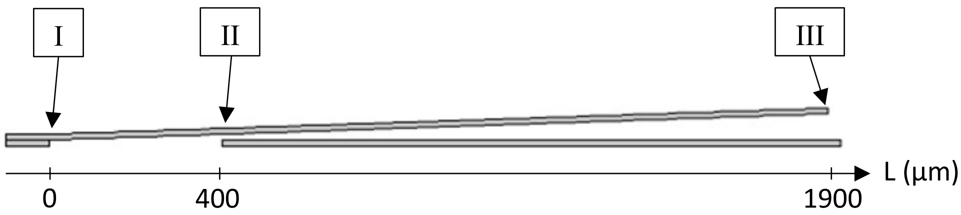

Figure 6.9: Measurement points for the laser-bent cantilevers.

Table 6.1: Cantilever height at the three measurement points.

Cantilever ID	Point I	Point II	Point III
Ideal	0	15	60
1-1 Top (R)	48	98	309
1-1 Bottom (R)	14	47	193
1-2 Top (F)	37	50	156
1-2 Bottom (F)	31	68	254
2-1 Top (F)	58	73	213
2-1 Bottom (F)	43	60	192
3-3 Top (R)	40	81	154
3-3 Bottom (R)	39	65	229

The cantilevers are identified by row and column of the matrix. (R): Rectangular, (F): Flared.

The full length cantilevers were then tested for deflection using a Veeco Dektak® 3ST contact surface profiler. The downward force was applied on the cantilever by the profiler stylus, which was swiped from Point II towards Point III, stopping at a length of 1600 µm, to prevent the profiler stylus from slipping out of the cantilever and hitting the substrate. The acquired data for one of the rectangular cantilevers, normalised to the original un-deformed cantilever profile, is given in Figure 6.10. From the ratio between the force applied and the displacement it was possible to calculate the spring constant of each cantilever and, therefore, the Young's modulus of the aluminium foil.

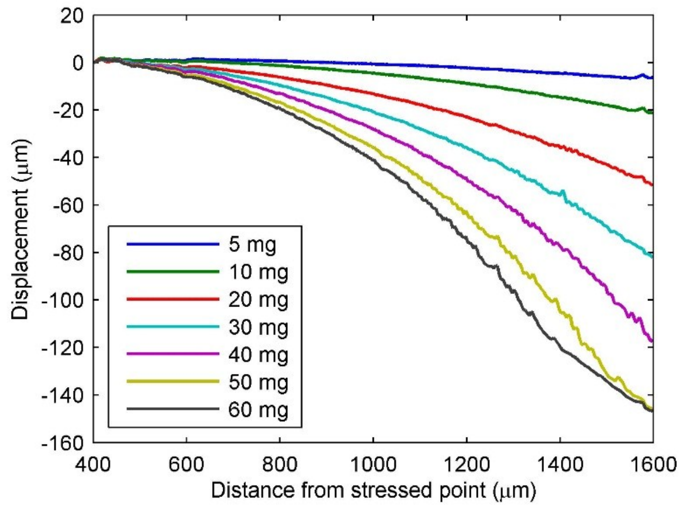

Figure 6.10: Displacement for the 3-3 Bottom rectangular cantilever for different applied loads.

For calculating Young's modulus, the rectangular cantilevers were considered, due to the simplicity of the calculation; in practice it is a property of the material and not related to the shape. As the displacement is measured for the point directly under the load, (5.4) is given for a concentrated load at the free end of a rectangular beam. The average of the calculated Young's moduli for the four rectangular cantilevers, reported in Table 6.2, is 24.35 GPa with a standard deviation of 1.6 GPa.

Table 6.2: Young's moduli for the rectangular full length cantilevers.

Cantilever ID	Young's Modulus (E) GPa
1-1 Top	25.2
1-1 Bottom	21.8
3-3 Top	26.1
3-3 Bottom	24.3

To confirm the measured results, one of the fabricated cantilevers was reproduced in COMSOL Multiphysics® and re-simulated. The good match for the displacement against applied force between the measured and simulated results can be seen in Figure 6.11. It should be noted that the average value of 24.3 GPa for the Young's modulus deviates significantly from the 69 GPa for pure aluminium. This large difference could be associated with the material composition and manufacturing process of the domestic grade kitchen foil used. However, the lower value is beneficial towards lower actuation voltages.

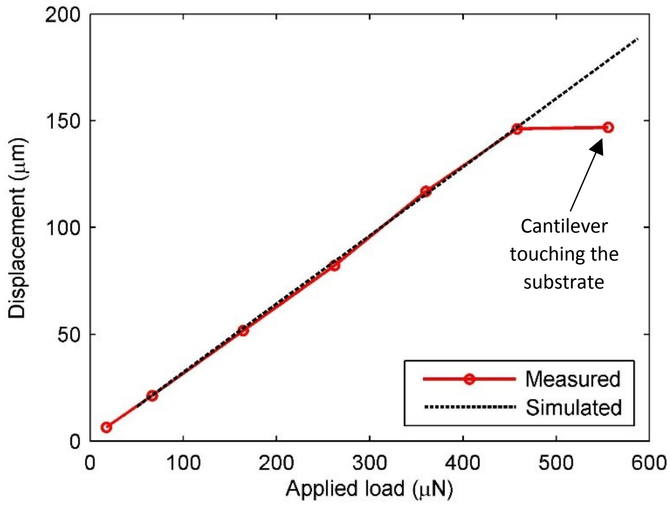

Figure 6.11: Comparison between the measured and simulated (Young's modulus of 24.3 GPa) displacement against applied load, for the top cantilever at location 3-3.

After the mechanical measurements, the cantilevers were tested for electrostatic actuation. The voltage was applied between the signal line and the ground plane of the CPW using DC probe needles. The results are shown in Table 6.3. One of the cantilevers (2-1 Top Flared) was tested up to 630 V, however breakdown occurred and no actuation was observed. Moreover, from the measured results, it can be seen that the actuation voltage substantially deviates from the expected value; mostly due to the poor repeatability of the fabrication process. Further problems found include the high tendency of sparking for the flared cantilevers, due to the higher charge accumulation at the sharp corners and, in general, stiction of the cantilever to the bottom fixed electrode; probably due to micro-welding. Fortunately, most of the cantilevers could be released from their 'actuated' state and tested again. The cycle lifetime for these cantilever switches varied between 1 and 18 actuations.

Table 6.3: Average actuation voltage for the full length rectangular and flared cantilevers.

Cantilever ID	Actuation Voltage, V	Cycle Lifetime
Ideal	180	-
1-1 Top (R)	515	4
1-1 Bottom (R)	430	1
1-2 Top (F)	330	2
1-2 Bottom (F)	324	18
2-1 Top (F)	No Actuation	-
2-1 Bottom (F)	415	2
3-3 Top (R)	505	7
3-3 Bottom (R)	405	8

Because of the issues found in this approach, most importantly the lack of control of the bending process, the laser bent cantilever structure was abandoned in favour of a simpler topology with a more controllable fabrication process.

6.2 Aluminium foil cantilevers on photoresist

With the results obtained from the laser-bent cantilevers, two remaining challenges were a consistent definition of the gap height and the micro-welding of the cantilever after actuation. The solution to both problems was identified to be the use of spin-coated photoimageable polymer (i.e. SU-8 photoresist in our case) to define the gap height at the anchor point and to create a thin dielectric layer on the bottom actuation electrode. In contrast to thick film deposition techniques (i.e. screen and stencil printing), spin coating allows a highly controlled deposition of layers.

In the new design the foil cantilevers are still laser-cut, but no bending is introduced. In this case, a dual-folded cantilever is considered. The newly adapted design is illustrated in Figure 6.12, with dimensions reported in Table 6.1. With this design, a uniform gap height of 10 µm is defined by the thickness of the spin-coated SU-8. Because of the reduced distance between the cantilever and the CPW signal line, the dimensions of the latter were also reduced, in order to decrease the OFF-state capacitance. The dimensions of the CPW signal line and spacing were limited by the minimum feature size that the laser can pattern on the screen-printed silver paste, which is 50 µm. In order to have a characteristic impedance of 50 Ω, with a CPW spacing of 50 µm, the line width was set to 190 µm. With these dimensions, the OFF-state capacitance was calculated as 45.47 fF and the on-state as 1.68 pF, considering parallel plate model with a 1 µm thick dielectric passivation SU-8 layer with a dielectric constant of 4.2 [182].

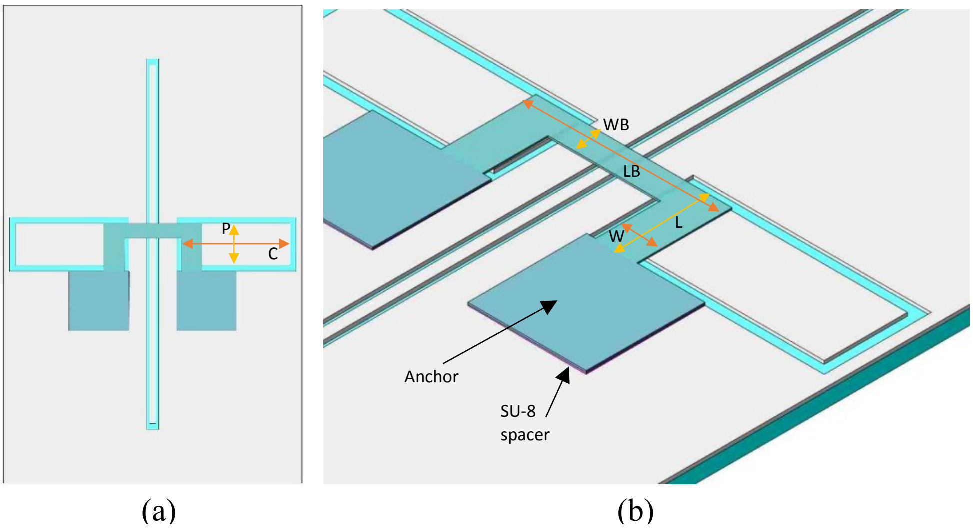

Figure 6.12: (a) Top and (b) isometric view of the CAD model for the folded foil cantilever.

Table 6.4: Dimensions for the newly designed dual folded cantilever.

Dimension	Description	µm
P	Bottom electrode length	600
C	Bottom electrode width	1800
L	Cantilever freestanding length	700
W	Cantilever width	350
LB	Bridge length	1650
WB	Bridge width	250

The main advantage of this structure, over the previous one, is that now the actuation voltage is applied between the ground plane and an isolated electrode, eliminating the need of the bias Tees to isolate the measurement equipment from the high actuation voltages. Also, the risk of self-actuation from very high RF signal power levels is avoided in practice.

This structure was designed to have an actuation voltage of 90V. Here, (5.22) for a triangular force distribution was used to define its length. Numerical simulations using COMSOL Multiphysics®, shown in Figure 6.13, confirm this prediction, with an actuation voltage of 89 V.

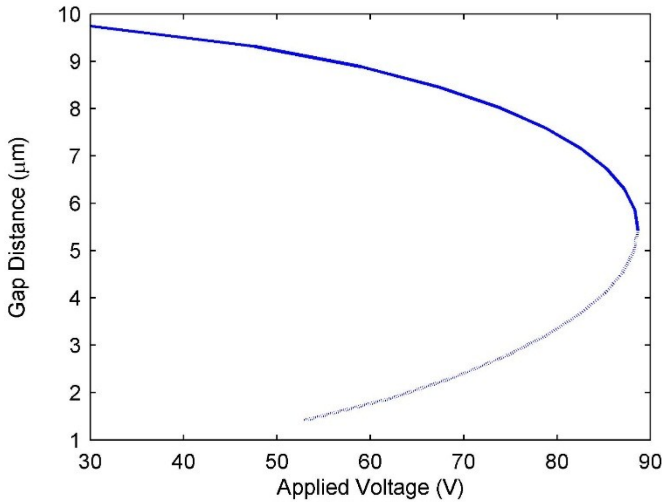

Figure 6.13: Numerical simulation for the actuation voltage of the designed folded beam cantilever.

6.2.1 Fabricated cantilevers

A prototype design was submitted for fabrication. The University of Leeds subsequently delivered variations of this design. These devices were arranged in pairs, having a cantilever length of 700, 800, 900 and 1000 μm, as shown in Figure 6.14. The bottom actuation electrode length was adapted accordingly.

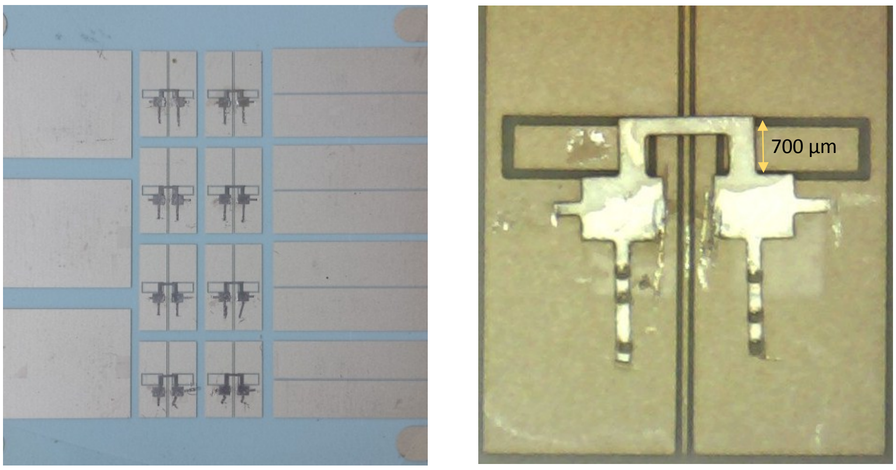

(a) (b)

Figure 6.14: (a) Photograph of the set of eight folded cantilevers fabricated and (b) micrograph of a 700 μm long cantilever.

The fabrication process flow, illustrated in Figure 6.15 (provided by the University of Leeds), consists of: (i) multiple spin-coating and soft baking of SU-8 to form the dielectric and spacer layers, (ii) positioning of the laser machined foil cantilevers, (iii) hard baking and (iv) ultrasound wedge bonding for the cantilever electrical connection to the CPW ground plane. According to the process described, the agreed 10 µm separation gap was changed to 5 µm.

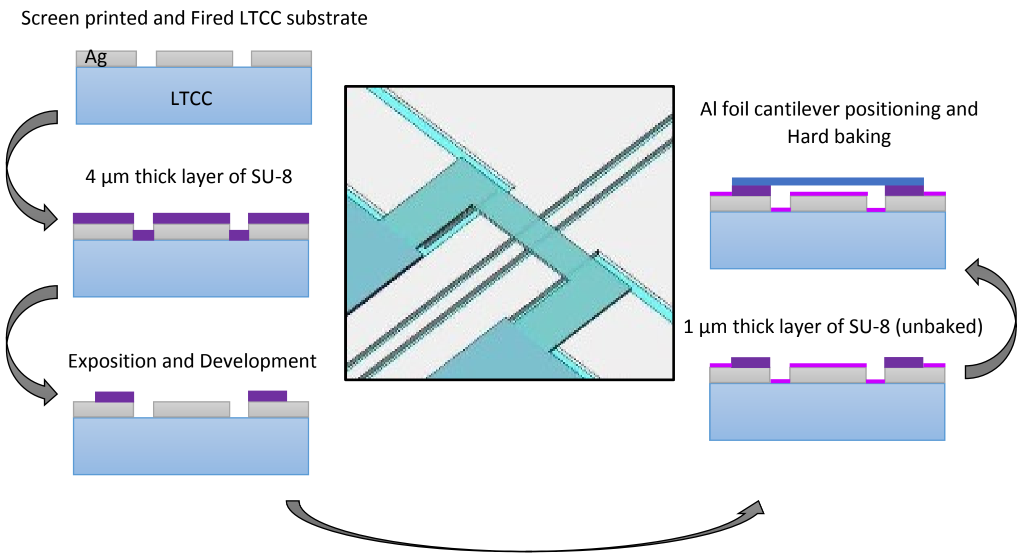

Figure 6.15: Suspended cantilever fabrication process flow.

Geometrical measurements were recorded at the five key point using the Veeco Wyko® N9100 optical profiler, as shown in Figure 6.16, and the results reported in Table 6.5.

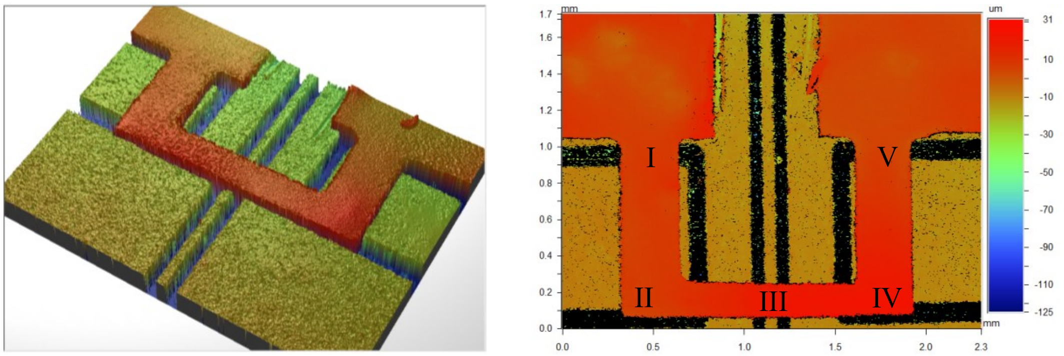

(a) (b)

Figure 6.16: (a) Isometric 3D view of a measured cantilever and (b) top view indicating the five measurement points.

Table 6.5: Measurement results (in microns) from the optical surface profiler for the five key points. The cantilever is identified by their length and the position on the sample.

Cantilever ID	Point I	Point II	Point III	Point IV	Point V
Ideal	10	10	10	10	10
700-Lx	12	19	20	34	6
700-Rx	7	8	7	8	6
800-Lx	6	3	5	2	2
800-Rx	8	27	6	24	6
900-Lx	9	6	10	13	4
900-Rx	3	10	3	6	6
1000-Lx	4	15	20	14	4
1000-Rx	5	4	19	25	6
Average	6.75	11.5	11.25	15.75	5

Consideration after the geometrical measurements

After observing the devices under a microscope and optical profiler, several deviations from the original design could be identified. Even though the cantilever dimensions appear correct, the gap height, which was changed from 10 µm to 5 μm, is inconsistent across the devices and between the two sides within the same cantilever. The gap height tends to increase from the anchor points (Points I and V) to the free end (Points II and IV), where it mostly matters in defining the actuation voltage. The average gap height across the fabricated device is relatively close to the designed value. Moreover, the signal line width of the CPW was changed and the wrap-around ground tracks at the ends of the line were omitted.

6.2.2 Actuation tests

After recording all the geometrical parameters, the values at points II and VI were averaged for every device and the actuation voltage predicted using the model described in Chapter 5; the same as the one used in the design. The cantilevers were then tested for actuation. The voltage was applied between the CPW ground plane and the two actuation electrodes. Although, after visual inspection under a microscope, no electrical connection was observed between the ground plane or cantilever and the actuation electrodes, five of the fabricated devices resulted short-circuits. Moreover, dielectric charging effects had to be taken into account during measurements; the applied voltage polarity had to be frequently reversed. Eventually, despite a reported breakdown voltage of 433 ± 16 V/μm for SU-8 [183], every actuation resulted in a short circuit – indicating that the passivation layer was either missing, defective or contaminated with conductive materials. Stiction was not observed for these devices and none of the cantilevers could be actuated more than three times before losing functionality.

The values of the average gap height, predicted and measured actuation voltage are reported in Table 6.6.

Table 6.6: Predicted actuation voltage for the eight fabricated cantilevers.

Cantilever ID	Avg. gap height, µm	Predicted actuation voltage, V	Avg. measured actuation voltage, V
Ideal	10	90	-
700-Lx	26.5	389	Short
700-Rx	8	65	Short
800-Lx	2.5	9	Short
800-Rx	25.5	280	310
900-Lx	9.5	51	80
900-Rx	8	39	Short
1000-Lx	14.5	77	93
1000-Rx	14.5	77	Short

6.3 Conclusions

In this chapter, two approaches for the manufacture of low-cost cantilever MEMS on LTCC are proposed and its limitations evaluated. Since some of the devices could actuate, this indicates the validity of the concept. The greatest obstacle to overcome is the establishment of a reliable and repeatable fabrication and assembly process. Such process would require automated equipment that can avoid the tolerances associated with hand assembly and would most likely be suitable for large-scale manufacturing. With these conditions, both solutions presented could represent a promising technology for the integration of low-cost MEMS on LTCC.

CHAPTER 7: LASER MICROMACHINING FOR SILICON MEMS RAPID PROTOTYPING

7.1 Overview

MEMS fabrication using conventional techniques such as reactive ion etching (RIE) and wet etching requires expensive equipment setups and the process can take up to several weeks between completion of design and device fabrication. These challenges can be a major limitation for designers of such devices when it comes to fabricating functional prototypes. Laser machining has found widespread application for wafer dicing, particularly for thin substrates, and research has been focused on improving ablation rate, cutting speed and edge quality [184]–[186]. In recent years laser micromachining has further become the subject of ongoing study in MEMS rapid prototyping research. Existing literature on silicon laser micromachining has focused mainly on three aspects: (i) the influence of laser system factors (i.e. wavelength, power and pulse energy) [187]–[190]; (ii) the influence of laser system-independent machining strategies (i.e. marking speed, pulse overlap, focusing) [187], [189], [191]–[193]; (iii) the effect of ambient conditions, such as pressure, assist gases or under-water machining [188], [194], [195]. Most studies have focused on improving ablation rate and machining time, only occasionally assessing the cutting quality, by evaluating metrics such as cut wall verticality and surface roughness. However, the fabrication high quality, high aspect ratio silicon structures using laser micromachining has hardly been addressed in the open literature. In particular, laser micromachining of beam structures, which are essential structural elements in MEMS, has been largely neglected in the literature until now. In this chapter the fabrication of high quality, high aspect ratio silicon beam structures using a diode pumped solid state (DPSS) UV laser system is investigated.

In this study the Taguchi design of experiment (DOE) method is used to evaluate the effect of selected influencing factors on the fabrication time, the beam sidewall surface roughness and the sidewall verticality.

7.2 Materials and methods

7.2.1 Experimental Setup

The laser machining setup used in this study consisted of a Spectra-Physics Talon solid state UV laser with a wavelength of 355 nm and a pulse width of 30 ns [196], a SCANLAB hurrySCAN II® galvo-scanner with a telecentric f-Theta scanning lens with 50×50 mm working area and 140 mm working distance, and an ASI MS-2000 XYZ motorized stage. The setup is illustrated in Figure 7.1.

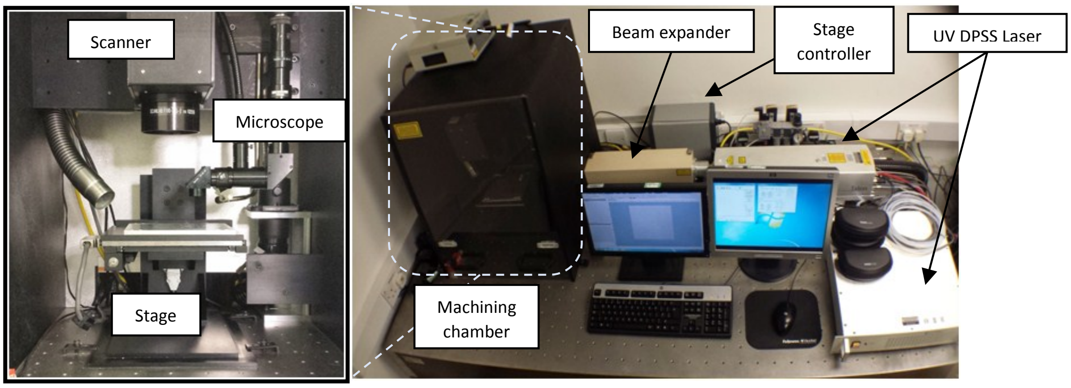

Figure 7.1: Photo of the laser micromachining setup indicating all its components.

The laser machining system was completed with a microscope, an air blower, an extractor and a beam expander, with all the components being assembled in a purposely designed enclosure. A frame grabber with graphical user interface was also developed, providing calibration and measurement capabilities.

The laser and the scanner are controlled through the SCANLAB laserDESK® software. Laser power measurements were obtained by placing an Ophir Nova-Display laser power meter with 10A-V1 detector head in the beam path after the scanner. An overview of the measured laser power over the relevant pulse repetition frequency range for representative values of laser diode current is provided in Figure 7.2. Note that the linear characteristic of the power versus pulse frequency indicates a constant pulse energy throughout the frequency range.

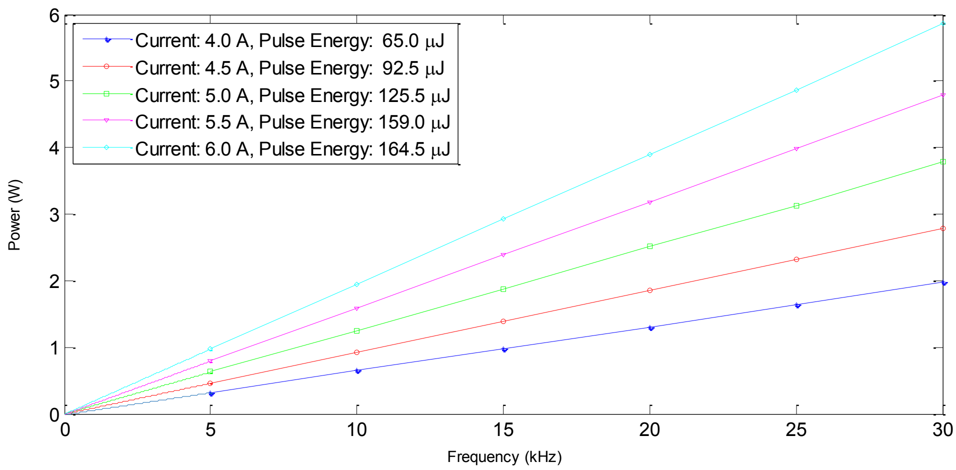

Figure 7.2: Graph of the measured laser power against pulse frequency for different diode currents and pulse energies.

7.2.2 Test methodology

<u>*Taguchi design of experiment method*</u>

The Taguchi DOE provides an efficient way of optimizing the performance of a product or process. This efficiency is accomplished through the use of orthogonal arrays, which allow the tester to conduct fewer experiments than in a full factorial study (i.e. one in which all parameter combinations are tested). This is especially beneficial as the number of factors to be studied increases, or when tests are time consuming or expensive. The underlying optimization approach of the Taguchi method is twofold: the design is optimized to achieve a performance which is closer to the target and to reduce variability of the performance [197].

Performance metrics and machining factors

In this study the performance metrics to be optimized were the machining time and the average surface roughness R_a and verticality of the beam side walls. Machining time is a metric to quantify the rapid prototyping potential, while surface roughness and sidewall verticality influence the mechanical behaviour of the structure. A total number of five influencing factors were studied which comprise laser and cutting strategy parameters: (A) pulse frequency, (B) diode current, (C) pulse overlap, (D) number of patterns, and (E) gap size. The pulse overlap PO is a function of marking speed v, frequency f and laser spot size ss on the Si wafer. The relationship is given in (7.1).

$$v = f \cdot ss \cdot (1 - PO) \tag{7.1}$$

The spot size, defined as the diameter of the laser-damaged region on the substrate, was measured to be an average of 32 μm on the Si for shallow machining lines and single-pulse exposures. This was considered constant for the following experiments, since no significant variation was noticed over the range of diode current investigated. The “number of patterns” parameter refers to the number of cut lines parallel to the contour cut line and “gap size” being the distance between them. These parameters will be explained in details in section 7.2.3, with Figure 7.3.

In preliminary tests the upper and lower thresholds for each machining factor were determined. These threshold values were chosen for each factor so that a reproducible through-wafer cut could be obtained with any combination. The range found for each factor was then divided into four levels in order to obtain a meaningful representation of said range, while maintaining a feasible number of required test runs. An overview of the factor levels is given in Table 7.1.

Table 7.1: Influencing factors and corresponding levels.

Symbol	Factor Name	Factor Level			
		Level 1	Level 2	Level 3	Level 4
A	Frequency (kHz)	5	10	15	20
B	Diode Current (A)	4.5	5	5.5	6
C	Pulse Overlap (%)	60	70	80	90
D	Number of Patterns	3	4	5	6
E	Gap Size (μm)	15	20	25	30

<u>*Orthogonal array*</u>

To be able to select a suitable orthogonal array for this experiment with five 4-level factors, the total degree of freedom (DOF) was calculated. The orthogonal array dimension, which represents the minimum number of tests and comparisons that has to be made to be able to determine the optimum level, has to be greater than the DOF of the process [198]. The DOF of a factor *X* can be calculated with

$$DOF_X = Number\ of\ Levels - 1 \quad (7.2)$$

The total DOF of the experiment will not only depend on the number of levels and factors, but also on interactions between factors, if present. In the first part of this study factor interactions were neglected as no correlation effects that could influence the results could be identified *a priori*. Furthermore, following Taguchi's recommendation to "*dig wide, not down*" [197] it was decided to rather study more individual factors than factor interactions.

When interactions between the factors are assumed to be non-existent, the total DOF is found by adding the factor DOFs and, with five 4-level factors, this results in a total DOF = 15. The minimum orthogonal array dimension is found as (DOF + 1). In our case the L`16 (modified L16) orthogonal array was selected for the experiment (Table 7.2). Noise factors, which are influencing factors hard or too expensive to control such as ambient conditions (e.g. atmospheric pressure and humidity), are not considered in this study. If controlled, their effect can be taken into account by considering an additional orthogonal array, defined as the "outer array".

Table 7.2: L'16 orthogonal array.

Orthogonal Array					
Test Condition	Factors and Levels				
	A	B	C	D	E
1	1	1	1	1	1
2	1	2	2	2	2
3	1	3	3	3	3
4	1	4	4	4	4
5	2	1	2	3	4
6	2	2	1	4	3
7	2	3	4	1	2
8	2	4	3	2	1
9	3	1	3	4	2
10	3	2	4	3	1
11	3	3	1	2	4
12	3	4	2	1	3
13	4	1	4	2	3
14	4	2	3	1	4
15	4	3	2	4	1
16	4	4	1	3	2

7.2.3 Test procedure

In order to study the effects of laser parameters on the performance metrics, fixed-fixed beams were laser machined from bulk silicon. Two vertically aligned rectangles were cut as shown in Figure 7.3 to obtain the double-sided clamped beam structure. A beam design with a width of 100 μm and a length of 10 mm, was chosen. The length of 10 mm was chosen because considered to be in excess what required for a device. The width was chosen to be comparable with the spot size, but large enough to ensure ease of handling and survival after machining. Thinner beams showed increased level damage, particularly in the middle, and breaking.

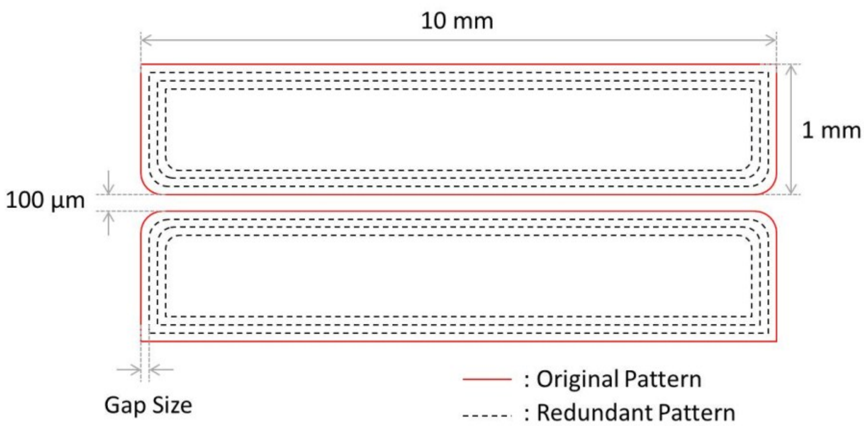

Figure 7.3: Figure illustrating the original and the redundant patterns used for the laser machining of a 10 mm long, 100 µm wide fixed-fixed beam out of a 525 µm thick silicon wafer.

Based on the results obtained in previous work [199], between 2 and 5 redundant patterns were added to the original pattern. Redundant patterns are scaled-down copies of the original pattern. These offset cuts allow for a wider trench. By adding these redundant patterns a through-wafer cut and full release of the rectangles can be ensured. The spacing between the patterns, in the following defined as "gap size", is uniform around the perimeter. One repetition consisted of first machining all lines of the lower rectangle and then those of the upper one, starting from the innermost pattern and proceeding outwards.

All experiments were conducted at atmospheric pressure and a temperature of 20°C. The set of 16 tests was repeated three times, yielding a total of 48 beams machined to be analysed. The experiments for each of the three test sets were performed in a different order to randomize the experiment.

7.2.4 Test post-processing

Cleaning

After machining, residual debris was observed, in the form of a white powder, in the area surrounding the beam and on the cut sidewalls. After observations under an SEM microscope and X-ray spectroscopy, the debris was confirmed to be silicon dioxide (SiO_2). Although loosely attached, due to the very delicate nature of the structures, cleaning techniques such as ultrasound could not be employed; therefore, a more selective, less aggressive technique had to be adopted.

Prior to the analysis, the machined wafers were cleaned in a hydro-fluoric acid (HF) solution (20 ml of 50% HF, 400 ml H_2O). The cleaning procedure consisted of a five minute immersion in the HF solution followed by rinsing the wafer with de-ionized water and drying with a nitrogen air gun.

Analysis of silicon beams

After manufacturing the machining time was recorded and, after cleaning, the sidewall verticality and surface roughness were measured.

Machining time, measured as the time from the beginning of the machining process until both rectangles (Figure 7.3) have been fully cut through, was obtained from the SCANLAB laserDESK® software as the time interval between the beginning of the machining process and the interrupt signal invoked by the observer.

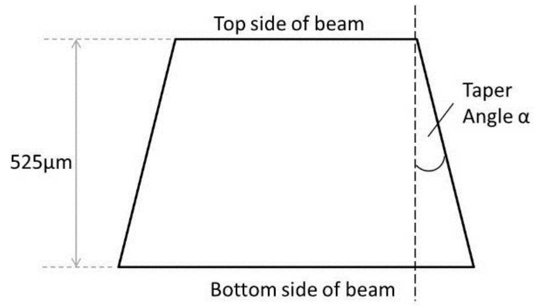

Figure 7.4: Symmetrical trapezoidal cross section of the laser machined beam used for the calculation of the taper angle.

For the analysis of the verticality of the beams it was assumed that the shape of the beam cross section was a symmetric trapezoid as shown in Figure 7.4. Microscope images of the beam at both clamped end, from the top (machining side) and bottom were taken and the beam width measured. Under the assumption of a uniform and symmetrical slope, the taper angle of the trapezoid was then calculated using the measured top and bottom widths of the beam. The average of the two measurements taken was considered for the further analysis. The surface roughness of the beam side wall was analysed using a surface profiler.

Three 1.3 mm length scan lines along the beam were recorded (top, middle, bottom of the side wall) for each beam and, from the 2D plot obtained, the mean profile roughness was calculated. An example for the surface roughness measurement is shown in Figure 7.5.

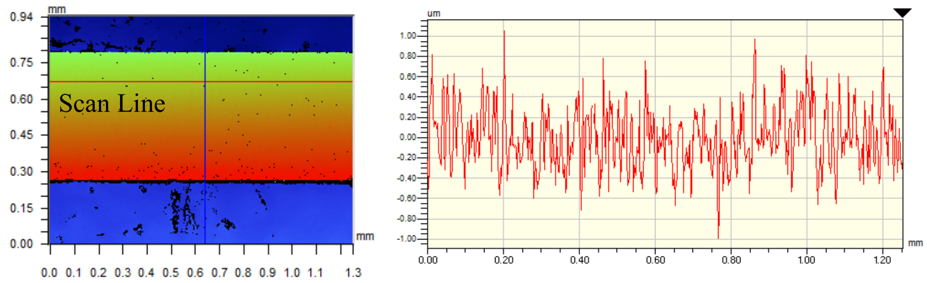

Figure 7.5: Example for the surface roughness measurement process from the data collected by the optical profiler.

<u>Calculation of S/N ratio</u>

Following the Taguchi method, the experimental results were analysed based on their signal-to-noise (S/N) ratio. By using S/N ratios, the optimum factor level, which is the level that shows the least variation around the target as well as an average result closest to the target, can easily be determined [197]. Furthermore, S/N ratio analysis indicates the effect a factor has on the performance metric. Essentially, the S/N ratio represents the mean square deviation (MSD) of the observations converted to a logarithmic scale. When calculating the MSD it is possible to choose between three quality characteristics: Smaller-is-better, Larger-is-better and Nominal-is-best. As the desired value for all performance metrics is preferred as small as possible, in this experiment the Smaller-is-better quality characteristic was used and the MSD was calculated by

$$MSD = \frac{1}{N}\sum_{i=1}^{N} y_i^2 \qquad (7.3)$$

where y_i is the measured value and N the number of observations per parameter, 4 in this case. The S/N ratio therefore is obtained by

$$S/N = -10\log_{10}(MSD) \tag{7.4}$$

The experimental results as well as the corresponding S/N ratio for each test condition are shown in Table 7.3**.** Because the experimental layout is considered orthogonal, the effect of each factor on the quality metric could be extracted from the data. This was done by calculating the mean S/N ratio for each level of a factor. For example, the mean S/N ratio for 'Frequency' at Level 1 was calculated by taking the mean of the calculated S/N ratios for test condition 1-4. Likewise, the S/N ratios for test conditions 5-8, 9-12 and 13-16 were considered for level 2, 3 and 4 respectively. Using these results the effect graphs for each performance metric were obtained.

Table 7.3: Mean of test results and calculated S/N ratio for the L'16 orthogonal array.

Test Condition	Results					
	Mean Surface Roughness (μm)	Mean Taper Angle (deg)	Mean Machining Time (s)	S/N Ratio for Surface Roughness (dB)	S/N Ratio for Taper Angle (dB)	S/N Ratio for Machining Time (dB)
1	0.44	2.92	1235	6.969	-9.311	-61.832
2	0.44	3.46	946	7.115	-10.797	-59.517
3	0.72	3.38	688	1.742	-10.688	-56.775
4	2.01	2.96	495	-6.145	-9.493	-53.906
5	0.66	5.53	670	3.395	-15.051	-56.996
6	0.43	6.33	527	7.336	-16.036	-54.449
7	0.37	2.52	352	8.684	-8.043	-50.947
8	0.50	3.19	301	6.037	-10.082	-49.572
9	0.38	4.81	474	8.162	-13.640	-53.522
10	0.71	3.47	291	2.107	-10.822	-49.288
11	0.88	4.90	226	0.032	-13.954	-47.089
12	0.43	3.08	226	7.073	-9.795	-47.070
13	0.61	4.70	291	4.090	-13.456	-49.268
14	0.46	3.04	192	6.691	-9.827	-49.676
15	0.63	4.41	204	4.032	-12.898	-46.179
16	0.50	4.84	193	5.955	-13.713	-45.699

7.2.5 Performance prediction and validation tests

Based on the results obtained from the data analysis, the performance of the machining process at optimal factor levels can be estimated for each of the performance metrics. An estimate of the S/N ratio at optimal levels (η) can be calculated by

$$\eta = \bar{\eta} + \sum_{i=1}^{m} (\eta_i - \bar{\eta}) \quad \textbf{(7.5)}$$

where $\bar{\eta}$ is the mean of the S/N ratio of all 16 test conditions, η_i the mean S/N ratio at optimal level for the i^{th} factor and m the number of influencing factors, which is 5 for this experiment. The obtained value for η is in decibel and it can be converted to the corresponding metric's unit (i.e. seconds, degree or μm) by first substituting it into (7.4) to obtain the MSD, and then taking its square root.

7.3 Results and discussion

In this section the means S/N ratios for each parameter, relative to the machining time and the sidewall verticality and surface roughness, are shown in Figure 7.6, 7.7 and7.8, respectively. The optimum level for a factor can be identified as being the one with the highest mean S/N ratio. Furthermore, the factor which displays the greatest range of mean S/N ratios is the one with the greatest effect on the performance of the process. Conversely, a factor with a small range has little effect on the performance. From these results, an optimised recipe and performance are predicted. Finally, in Table 7.4, the results of the optimised recipe are compared to the best and worst results from the Taguchi orthogonal array.

7.3.1 Machining time

The results for machining time, shown in Figure 7.6, indicate that the optimal condition for minimizing processing time is: Frequency = 20 kHz, Diode Current

= 6 A, Pulse Overlap = 90%, Number of patterns = 4, Gap Size = 30µm. Moreover, it was found that the factor Frequency (Factor A) has the largest effect on the machining time. These results also show that, within the investigated range of the factors, high pulse energy and high fluence are desired for a short machining process. The results for gap size suggest that a larger distance between the patterns decreases the machining time. It appears that as the gap size approaches the laser spot size (32 µm) the laser energy is used more and more efficiently in the ablation process, leading to a faster cut. In validation tests it was shown that using the optimal condition the average machining time is 102 s (see Table 7.4), while previously, the best result had been 192 s (Test condition 14). Comparing the result of the optimal condition with the worst result of the orthogonal array test conditions – 1235 s obtained with Test condition 1 – demonstrates the performance improvement that can be obtained. Moreover, it was shown that the experimental results for the optimal condition even outperform the estimated 125 s obtained from (7.5) (shown in the right hand column of Table 7.4).

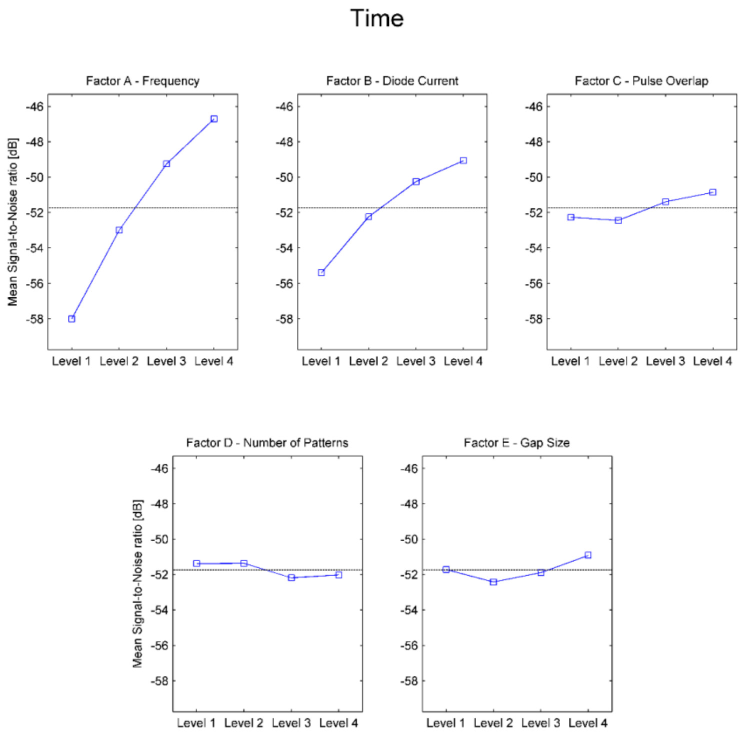

Figure 7.6: Mean S/N ratio effect graph for machining time. The dashed line represents the total mean S/N ratio (Appendix I-C).

7.3.2 Taper angle

The predicted optimal condition for minimizing taper angle was found to be: Frequency = 5 kHz, Diode Current = 6 A, Pulse Overlap = 90%, Number of patterns = 3, Gap Size = 15 μm. The dominating effect for this performance characteristic is the number of redundant patterns (Factor D), as illustrated in Figure 7.7. The results for diode current, pulse overlap and gap size show a clear trend towards high fluence being beneficial for reducing the taper angle. Furthermore, the fact that low frequency is paired with high pulse overlap indicates that slow marking speed is desired in achieving a small taper angle. Referring to Table 7.4 and comparing the estimated performance from (7.5) (1.66°) to the experimentally obtained values when using the suggested optimal condition (2.56°), it appears that the theoretical estimation over-estimates the achievable performance. Moreover, it was found that the best condition of the orthogonal array (Test condition 7) yields similar results to those of the optimal condition suggesting two optima. Both of these findings indicate a possible correlation between the factors, which was neglected in this study.

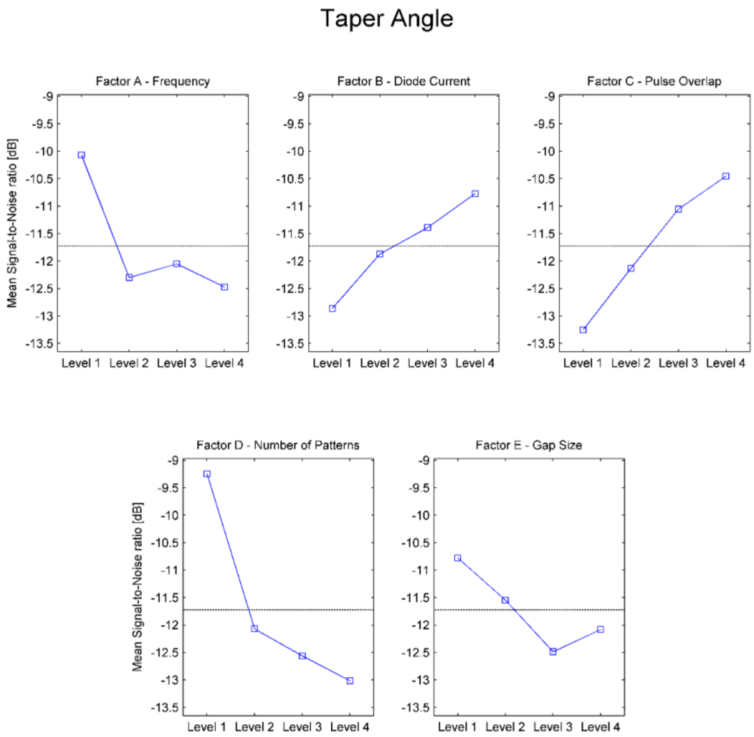

Figure 7.7: Mean S/N ratio effect graph for taper angle. The dashed line represents the total mean S/N ratio (Appendix I-D).

7.3.3 Surface roughness

Surface roughness is expected to be minimized for the following condition: Frequency = 10 kHz, Diode Current = 5 A, Pulse Overlap = 80%, Number of patterns = 3, Gap Size = 20 μm. From Figure 7.8 it can be seen that the dominating factor for this performance metric is the gap size (Factor E). Similar to the findings for taper angle the average result of the experimental validation tests did not show good agreement between the predicted optimal condition of 0.44 μm and the estimated performance from (7.5) of 0.19 μm. While the optimal condition yields a surface roughness which is able to compete with the best result obtained it was found that several test conditions of the orthogonal array from Table 7.2 (i.e. condition 1, 2, 6, 7, 9 and 12) yield similar results to or even outperform the optimal condition. Again, this behaviour is thought to be due to correlation between factors. Table 7.4 compares the achieved surface roughness using the optimal condition with the best (Test Condition 7) and worst (Test Condition 4) results of the orthogonal array test conditions. A prospective view for the beam surface roughness obtained with the optical surface profiler for these three beams is shown in Figure 7.9.

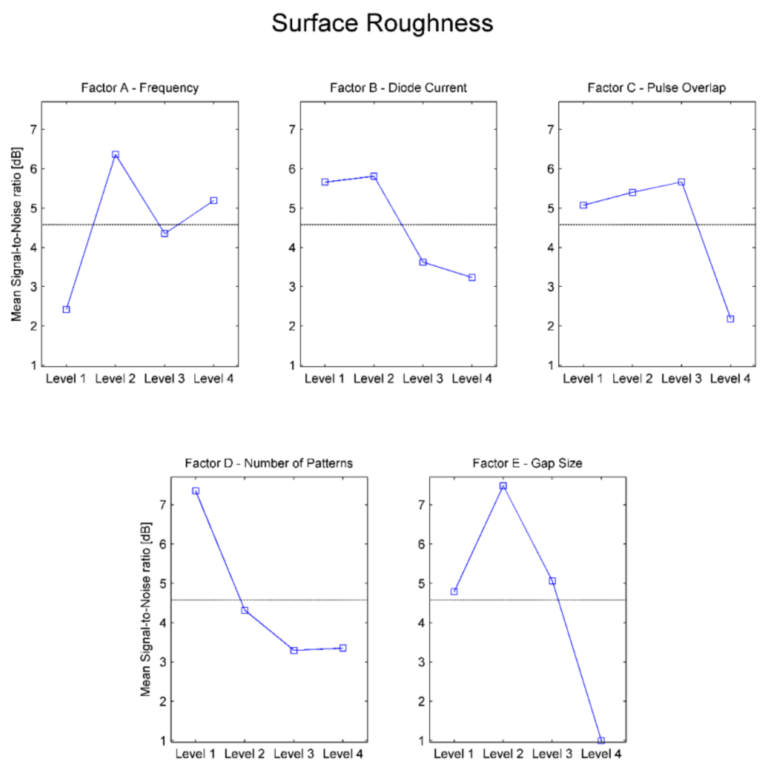

Figure 7.8: Mean S/N ratio effect graph for surface roughness. The dashed line represents the total mean S/N ratio (Appendix I-E).

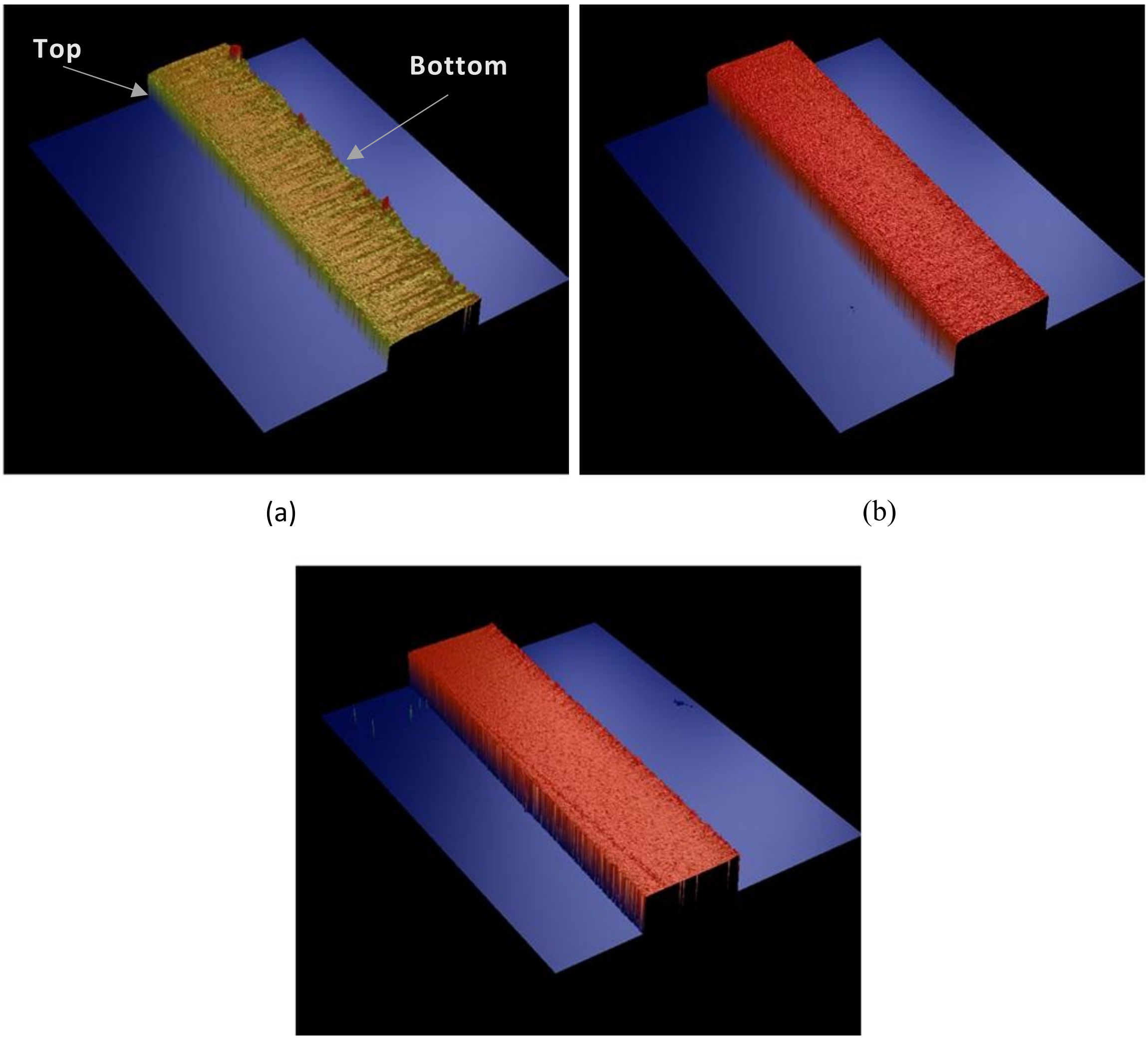

(a) (b)

(c)

Figure 7.9: Veeco 2D scans showing the sidewall surface profiles of the laser machined beams for (a) test condition 4, (b) test condition 7, and (c) predicted optimal condition. The best result was obtained for test condition 7. In all the pictures the bottom side of the beam to the right.

Table 7.4: Experimental results of the optimal condition and estimated performance compared to the best and worst result of the orthogonal array test conditions from Table 7.2.

Performance Metric	Test Condition Name	Test Condition Code	Result 1	Result 2	Result 3	Mean	Estimated Performance
Taper Angle (deg)	Taguchi Optimal Condition	A1/B4/C4/D1/E1	2.64	2.56	2.49	2.56	1.66
	Test Condition 7 (Best)	A2/B3/C4/D1/E2	2.41	2.63	2.53	2.52	
	Test Condition 6 (Worst)	A2/B2/C1/D4/E3	6.59	6.21	6.21	6.33	
Surface Roughness (μm)	Taguchi Optimal Condition	A2/B2/C3/D1/E2	0.41	0.43	0.48	0.44	0.19
	Test Condition 7 (Best)	A2/B3/C4/D1/E2	0.32	0.39	0.39	0.37	
	Test Condition 4 (Worst)	A1/B4/C4/D4/E4	1.60	2.09	2.33	2.01	
Machining Time (s)	Taguchi Optimal Condition	A4/B4/C4/D2/E4	102	102	102	102	125
	Test Condition 14 (Best)	A4/B2/C3/D1/E4	182	190	204	192	
	Test Condition 6 (Worst)	A1/B1/C1/D1/E1	1206	1246	1252	1235	

7.4 Improved Taguchi DOE with interactions

Although the results obtained with the previously shown analysis are relatively satisfactory, further investigation was needed to understand the possible effect of factor interactions on the performance metrics. In order to obtain such information, an analysis of variance (ANOVA) study was performed on the samples.

The ANOVA is a statistical inference procedure for determining the degree of internal variability between two or more groups of data. This method is usually applied on experimental data to determine the impact that independent variables have on the dependent variable (i.e. how relevant is a parameter on a process outcome). It also helps to understand if the collected data follows a trend (the data is meaningful), or not (the data is noisy or random). The noise in the collected data can be evaluated by the error term in the ANOVA results. For example, a high value for error term indicates noisy data.

In our case the ANOVA highlighted that interactions were most likely between gap size, pulse overlap and frequency for the surface roughness. For the taper angle interactions were most likely between number of patterns, pulse overlap and frequency (Appendix I-F). As the results for the machining time already outperformed the predictions, further investigation on this performance metric was not performed.

With this newly acquired knowledge, two new orthogonal arrays were developed to perform a Taguchi DOE which took into account the effect of interactions. The two arrays were designed to optimise the surface roughness and taper angle, respectively. In this case, due to the increased DOF, the L27 array (i.e. twenty-seven tests) was chosen. The set of 27 experiments was performed twice for each of the two performance metrics under analysis, giving a total of 108 fabricated and measured beams. While the value range for each factor was not changed, with this new array only three levels were used. For the number of patterns, values three to five were chosen, as, during the previous tests, six lines yielded worse results.

After the measurements, the mean S/N ratio was calculated for each array. The results for the surface roughness and taper angle are reported in Figure 7.10 and 7.11, respectively.

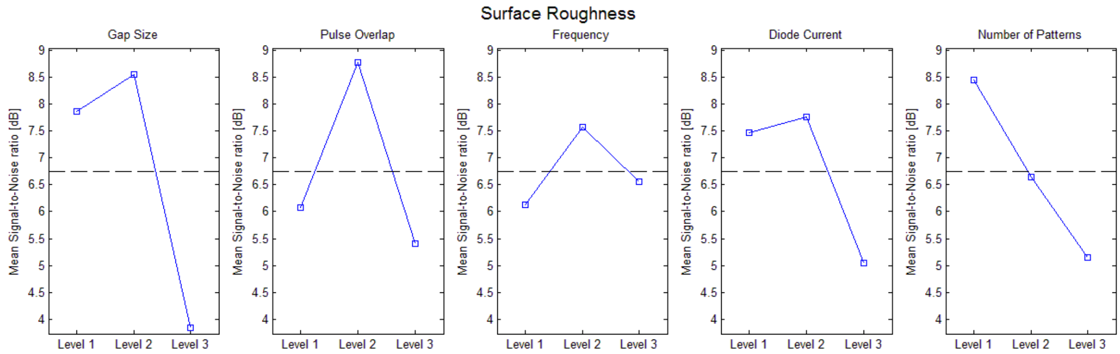

Figure 7.10: Mean S/N ratio effect graph for surface roughness for the improved DOE. The dashed line represents the total mean S/N ratio (Appendix II-A).

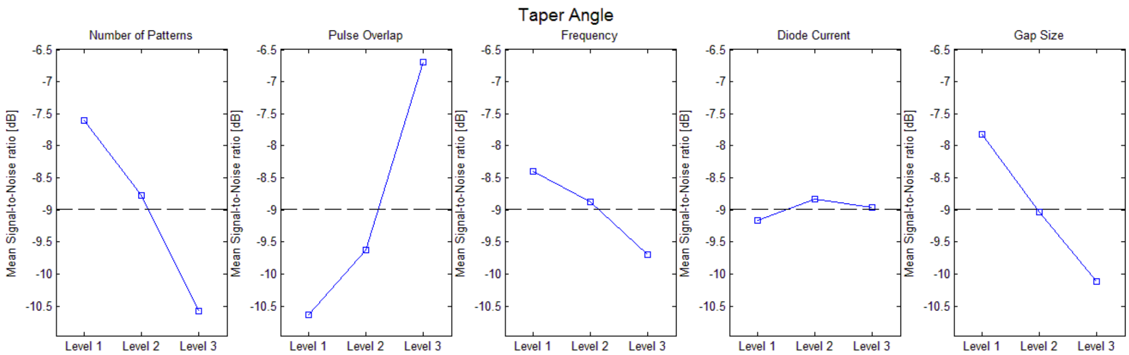

Figure 7.11: Mean S/N ratio effect graph for taper angle for the improved DOE. The dashed line represents the total mean S/N ratio (Appendix II-B).

An ANOVA test was eventually performed on these new sets of results to understand the contribution of each factor and interactions on the machining process. The results for the surface roughness and taper angle are reported in Table 7.5.

Table 7.5: ANOVA results indicating the contribution, in percentage, for each of the factors and interactions towards a good surface roughness and taper angle. Negative percentages are a mathematical artefact and are related to factors with little to no contribution.

Factor	Contribution (%)	
	Surface Roughness	Taper Angle
A – Pulse frequency	1.26	-1.29
B – Diode current	8.94	-4.81
C – Pulse overlap	13.33	31.64
D – Number of patterns	11.25	14.57
E – Gap size	28.27	6.50
Interaction A C	11.85	-2.99
Interaction A D	N/A	-2.89
Interaction A E	10.72	N/A
Interaction C E	-2.20	N/A
Interaction D E	N/A	-6.55
Error	16.58	65.82
Total	100	100

From the results it can be seen that the taper angle ANOVA has a very high error. This can be associated with the curved profile for the side wall cross section. Indeed, some of the but beams did not show a trapezoidal cross section, as shown in Figure 7.4, but have a flared cross section, with a curved wall profile. It is supposed that this introduced further uncertainty in the measurement and, therefore, the high error.

Although the ANOVA results indicate relatively high error percentages, the factors with higher contributions are still clearly indicated and agree with the values of the mean S/N ratio. From the obtained results, predictions for an optimised recipe could be obtained. For the surface roughness the predicted optimised recipe is: Frequency = 12.5 kHz, Diode current = 5.25 A, Pulse overlap = 75%, Number of patterns = 3, Gap size = 22.5 µm. For the taper angle the predicted optimised recipe is: Frequency = 5 kHz, Diode current = 5.25 A, Pulse overlap = 90%, Number of patterns = 3, Gap size = 15 µm.

Confirmation test beams were then laser machined to prove the validity of these new recipes. The predicted surface roughness and taper angle for the confirmation tests are 0.22 µm and 1.23°, respectively. For the surface roughness recipe a value of R_a = 0.27 µm was measured, while for the taper angle a value of 2° was found. Although the values obtained are not better than some of the results obtained during the array measurements, they are comparable with the best results obtained and the predictions. During measurements values as low as 0.25 µm for the surface roughness and 1.5° for taper angle were obtained. As the obtained and predicted values are relatively close, the measurements uncertainty can be considered to have relevant impact on the predicted recipes. Moreover, factors that were not included in the Taguchi DOE could have influenced the results. In later tests it was noticed that a low air flow from the blower during machining has adverse effects on the wall verticality. This may be related to the debris accumulating in the laser machined trench and cause loss of repeatability in high precision laser machining.

Finally, it should be remembered that the Taguchi DOE not only aims at finding an optimal recipe, but also at developing a reliable and repeatable process. Indeed, the obtained beams, although not optimal, were of very good quality.

7.5 Laser machined beams for devices

For the development of micromechanical devices, the cross section was considered the most relevant factor for the mechanical properties a beam. Therefore, the recipe optimised for taper angle was employed in the development of thin beams. The beam design used in the tests had a depth of 525 μm (silicon wafer thickness) and a nominal design width of 100 μm, giving an average top width of 70 μm. This value is consistent with the design width of 100 μm less 32 μm laser spot size. The beam width in the design was progressively reduced from 100 μm to 40 μm, eventually leading to a beam with a top width of only 13 μm and a bottom width of 26 μm, equivalent to a taper angle of 1.4°. The improved taper angle might be associated with the design width reduction. As the beam width changes, the thermal mass of the ablated structure is reduced and the ablation process increases in efficiency, leading to a greatly improved taper angle. It should be noted that the reported dimensions and taper angle are comparable with the typical feature size and taper angle achievable with DRIE. A micrograph of the beam is shown in Figure 7.12.

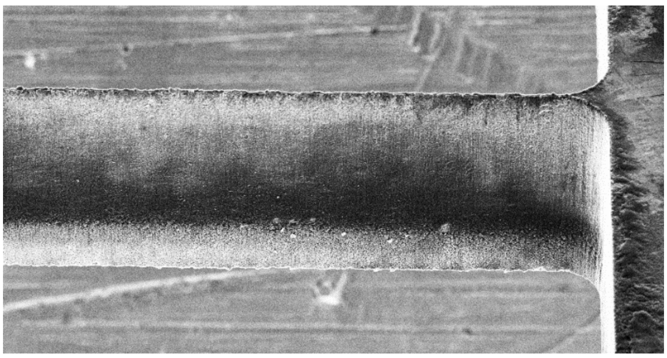

Figure 7.12: SEM micrograph of a 13-26 μm wide beam laser machined using the optimal condition for taper angle, resulting in an average aspect ratio of 26.9.

After the laser machining of such thin beams, damages could be observed in the central part of the beam. This damage is associated with vibrations caused by the laser etching process. Indeed, during laser machining the laser pulses make the beams vibrate and the resulting deflection puts the beam in the path of the laser. To overcome this issue the silicon substrate was glued to a glass carrier. A mixture of 2:1 water and commercial washable PVA glue was used, due to its ease of release in hot water.

Based on this beam dimensions, a double folded suspension with micro-grippers was designed and machined. The design and the manufactured device are shown in Figure 7.13.

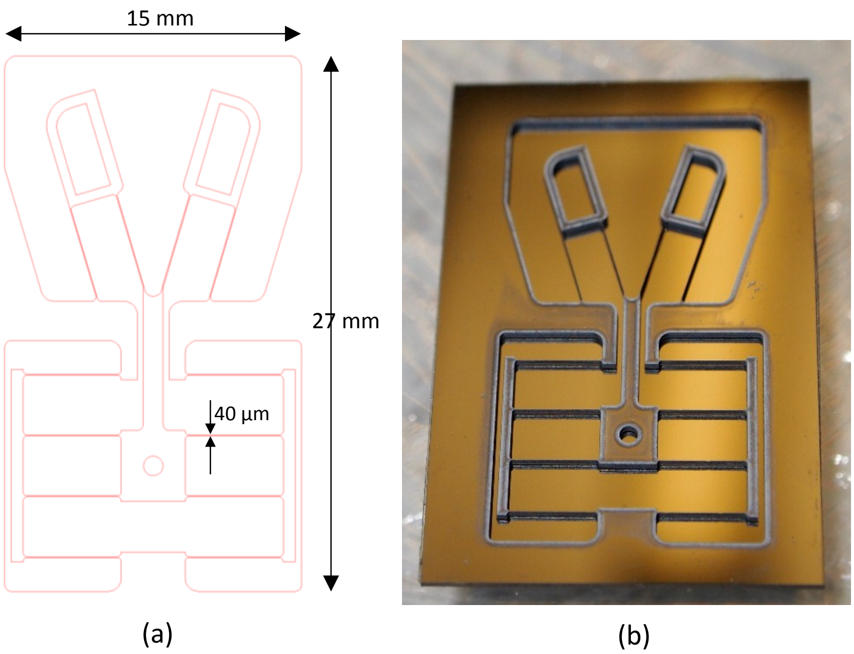

Figure 7.13: (a) CAD drawing and (b) laser machined double folded suspension micro grippers.

While clamped-clamped beams are inherently stable structures, the release of the device from the surrounding silicon posed some challenges. To help the water penetrate through the cut lines, the gaps remaining after fabrication were widened by further laser machining of the redundant patterns only. However, the surface tension of the water was still sufficient to make separation of the device from the surrounding silicon. Therefore, after release from the glass carrier, the water was removed and the device, still sitting on the carrier, immersed in isopropyl alcohol. The surface tension of the alcohol, being approximately three times smaller, considerably helped the release of the device without damage. Eventually the suspension frame was glued on a silicon carrier substrate using 50 μm thick double sided tape.

7.6 Conclusions

In this study the influence of some of the most relevant laser machining factors on machining time, surface roughness and verticality of thin silicon beams was analysed using the Taguchi design of experiment method and ANOVA. After preliminary results were obtained, the interactions between factors were taken into account and optimised factor combinations were predicted and tested in validation tests. The measured values were compared to the theoretically predicted results. As shown in this study, machining of the test structure can be accomplished in 102 seconds using the optimized machining settings, indicating the influence of high pulse energy and fluence in rapid machining. Although high verticality through-wafer cutting can be associated with the same machining conditions, the time for a full cut increases sixfold. This indicates that a compromise between cut verticality and processing time is theoretically possible by increasing the pulse frequency and scanning speed accordingly, keeping the same pulse overlap.

With the developed process sidewall surface roughness and verticality of the silicon beam can be significantly improved to reach 0.27 μm and 2°, respectively. Although it could not be established that the obtained best values for surface roughness, verticality and aspect ratio represent the optimum, the obtained results are considered satisfactory. Indeed, the obtained recipes led to the fabrication of very high aspect ratio beams and a complete mechanical device, demonstrating the feasibility of this technology for MEMS prototyping.

CHAPTER 8: CONCLUSIONS

8.1 3D Printing of microwave and millimetre-wave passive components

3D printed and electroless plated metal-pipe rectangular waveguides in FDM and SLA technology have been demonstrated in the first part of this thesis. With a performance comparable to commercially available components, the 3D printed alternative offer a low-cost lightweight alternative to standard technology. This advantage is further enhanced when considering the 3D printed high performance W-band sixth-order inductive iris bandpass filter presented in Chapter 2. To demonstrate the flexibility of this technology, in Chapter 3 an X-band dielectric flap phase shifter is reported. Four of such shifters were then used to develop a fully 3D printed phased antenna array. For this system, all the components were designed, simulated and 3D printed. These included power splitters, bends and bespoke waveguides and flanges. Such components and possibly more complex ones, which are usually associated to high costs, can be fabricated with no additional manufacturing costs.

Although the performance of some components or parts thereof (i.e. X-band power splitter and W-band flanges) are in need of improvements, with these technologies a design iteration can be performed in a short time and the performance improved.

Future work

In the thesis, the main issue identified with the fabrication of 3D printed waveguides was related to the fabrication of high quality flanges. This problem becomes more prominent as the waveguide cross-section dimensions reduce. Beyond the flange alignment, the building material compresses and deforms under the pressure of the fastening bolts. This introduces undesired reliability issues into waveguide connections. Further work should be undertaken to improve the flange design and improve the quality of connection. Alternative designs, possibly involving choke rings, would remove the need for high torque tightening of the fastening bolts. Moreover, bespoke flanges can be designed to improve connection between 3D printed waveguides and a hybrid metal-to-plastic adapter to connect a 3D printed system to a standard flanged.

Further investigation will also be undertaken to fully characterise each component of the 3D printed phased antenna array and its radiation pattern.

8.2 RF-MEMS on LTCC

In the more speculative (high risk) second part of this thesis, the design and fabrication of RF MEMS for integration with LTCC technology is reported. Three approaches are considered, based on LTCC bulk micromachining, aluminium foil laser bending and hybrid thin/thick-film technology. In Chapter 4, a study of the shrinkage induced bucking of fixed-fixed LTCC beams is presented. A model for the prediction of actuation voltage in cantilever MEMS is reported in Chapter 5. This model is more accurate than the widely accepted textbook formulas and much less computation intensive than numerical simulations.

In Chapter 6, two enabling technology are presented for the fabrication of cantilever MEMS using aluminium foil. With the first, laser bending is employed to deform the cantilever beams and define the gap height. For the second, thin-film technology is employed, via spin coating of photoresist, to define the gap height. With the former, the gap height increases progressively with the length of the cantilever, with the latter the gap height is constant and minimized. This sensibly reduces the actuation voltage and values as low as 80 V were achieved.

Although no useful devices could be fabricated, both solutions showed potential for the integration into LTCC technology. With a more controllable and repeatable fabrication process, as available in industry, both technologies could potentially be employed for large-scale integration of low-cost RF MEMS in LTCC multilayer circuits.

Future work

Further investigation is required to improve the repeatability of the manufacturing process for both the aluminium foil technologies presented. This work can be carried out with further simulations and research of alternative materials (e.g. metal foils) and characterization of such materials. With a stable process, it will be possible to design and fabricate a demonstrator for the devices, such as true time delay phase shifters.

8.3 Laser machining for MEMS rapid prototyping

In the third part of this thesis the Taguchi design of experiment and ANOVA are used to improve the laser machining process for high aspect ratio structures in silicon. This study takes into account significant parameters interactions and enables a through-wafer machining with minimum features and verticality comparable to DRIE machining. Thin beams, having an average aspect ratio of 26.9, are then employed to build a double-folded suspension with micro-grippers.

Although the surface roughness quality of the fabricated beams represents a limit in the maximum deflection before fracture, it should be noticed that the processing time for this large device is less than 1.5 hours. Moreover, the equipment costs associated with the laser machining used are approximately one order of magnitude lower than standard DRIE silicon processing.

Future work

The fabrication process developed achieved in fabricating high aspect ratio beams, but a complete characterisation of the manufactured beams needs to be carried out. After the characterisation of the beams, the fabricated device should also be fully measured. The first issue that can be addressed in future work is the reduction of the side-wall surface roughness for the fabricated beams, as this can represent a severe limitation for the functionality of the beams. Chemical polishing can be taken into consideration for this part. Further investigation can also be carried out to understand the level of defects introduced by laser machining, which could cause failure for fatigue. Thermal annealing will be considered for this step. Eventually, combining multi-step laser machining with improved adhesives could also be employed to improve the original beam quality. After a full optimisation and characterisation of the beams, more complex technology demonstrators, with included actuation, can be designed and fabricated.

8.4 List of publications

The following conference and journal papers are the result of the work presented in this thesis:

1. D'Auria M., Sunday A., Hazell J., Robertson I. D., Lucyszyn S., "Enabling technology for ultra-low-cost RF MEMS switches on LTCC," in *Proc. RF & Microwave Society (ARMMS) Conference*, Milton Common, 2013.

2. Rathnayake-Arachchige, D., Hutt, D.A.; Conway, P.P., D'Auria, M., Lucyszyn, S., Lee, R.M., Robertson, I.D., "Patterning of electroless copper deposition on low temperature co-fired ceramic," in *Proc. IEEE 15th Electronics Packaging Technology Conference (EPTC 2013)*, Singapore, 2013, pp. 630-634.

3. D'Auria M., Tolou N., "UV-Laser cutting for silicon MEMS prototyping: improving etching rate and quality," in *Proc. 14th euspen International Conference*, Dubrovnik, Croatia, 2014, vol. 2, pp. 275.

4. Pusch T. P., D'Auria M., Tolou N. Holmes A., "Laser micromachining of thin beams for silicon MEMS: optimization of cutting parameters using the Taguchi method", in *Proc. ASME 2015 International Design Engineering Technical Conferences & Computers and Information in Engineering Conference (IDETC/CIE 2015)*, Boston, USA, 2015

5. D'Auria, M., Otter, W.J., Hazell, J., Gillatt, B.T.W., Long-Collins, C., Ridler, N.M., Lucyszyn, S., "3-D printed metal-pipe rectangular waveguides," *IEEE Transactions on Components, Packaging and Manufacturing Technology (CPMT)*, vol. 5, no. 9, pp.1339-1349, Sep. 2015

REFERENCES

1] S. S. Crump, "Modeling apparatus for three-dimensional objects," U.S. Patent 5 340 433, 08-Jun-1992.

[2] C. W. Hull, "Apparatus for production of three-dimensional objects by stereolithography," U.S. Patent 4 575 330, 08-Aug-1984.

[3] C. R. Deckard, "Method and apparatus for producing parts by selective sintering," U.S. Patent 4 863 538, 17-Oct-1986.

[4] "FDM 3D Printing," *ValinTech Inc.* [Online]. Available: http://www.valintech.com/index.php?m=5. [Accessed: 17-Sep-2015].

[5] "Stereolithography," *Wikipedia*. [Online]. Available: https://en.wikipedia.org/wiki/Stereolithography. [Accessed: 17-Sep-2015].

[6] "Selective laser sintering," *Wikipedia*. [Online]. Available: https://en.wikipedia.org/wiki/Selective_laser_sintering. [Accessed: 17-Feb-2015].

[7] C. R. Garcia, J. Correa, D. Espalin, J. H. Barton, R. C. Rumpf, R. Wicker, and V. Gonzalez, "3D printing of anisotropic metamaterials," *Progress in Electromagnetics Research (PIER) Letters*, vol. 34, pp. 75–82, Jul. 2012.

[8] Y. Urzhumov, N. Landy, T. Driscoll, D. Basov, and D. R. Smith, "Thin low-loss dielectric coatings for free-space cloaking," *Optics Letters*, vol. 38, no. 10, pp. 1606–1608, May 2013.

[9] N. Delhote, D. Baillargeat, S. Verdeyme, C. Delage, and C. Chaput, "Ceramic layer-by-layer stereolithography for the manufacturing of 3-D

millimeter-wave filters," *IEEE Transactions on Microwave Theory and Techniques*, vol. 55, no. 3, pp. 548–554, Mar. 2007.

[10] Y. Huang, X. Gong, S. Hajela, and W. J. Chappell, "Layer-by-layer stereolithography of three-dimensional antennas," in *IEEE Antennas and Propagation Society International Symposium*, 2005, vol. 1A, pp. 276–279.

[11] B. Liu, X. Gong, and W. J. Chappell, "Applications of layer-by-layer polymer stereolithography for three-dimensional high-frequency components," *IEEE Transactions on Microwave Theory and Techniques*, vol. 52, no. 11, pp. 2567–2575, Nov. 2004.

[12] J. W. Allen and B.-I. Wu, "Design and fabrication of an RF GRIN lens using 3D printing technology," *SPIE Terahertz, RF, Millimeter, and Submillimeter-Wave Technology and Applications VI*, vol. 8624, pp. 1–7, Mar. 2013.

[13] M. Liang, W. Ng, K. Chang, K. Gbele, M. E. Gehm, and H. Xin, "A 3-D Luneburg lens antenna abricated by polymer jetting rapid prototyping," *IEEE Transactions on Antennas and Propagation*, vol. 62, no. 4, pp. 1799–1807, Apr. 2014.

[14] N. Yudasari, D. Vogt, J. Anthony, and R. Leonhardt, "Hollow core terahertz waveguide fabricated using a 3D printer," in *39th International Conference on Infrared, Millimeter, and Terahertz waves (IRMMW-THz)*, 2014, vol. 2.

[15] Z. Wu, W.-R. Ng, M. E. Gehm, and H. Xin, "Terahertz electromagnetic crystal waveguide fabricated by polymer jetting rapid prototyping.," *Optics*

Express, vol. 19, no. 5, pp. 3962–72, Feb. 2011.

[16] S. Pandey, B. Gupta, and A. Nahata, "Terahertz plasmonic waveguides created via 3D printing.," *Optics Express*, vol. 21, no. 21, pp. 24422–24430, Oct. 2013.

[17] G. M. Rebeiz, "RF MEMS switches: status of the technology," in *12th International Conference on Solid-State Sensors, Actuators and Microsystems*, 2003, vol. 2, pp. 1726–1729.

[18] S. Pranonsatit, G. Hong, A. S. Holmes, and S. Lucyszyn, "Rotary RF MEMS Switch Based on the Wobble Motor Principle," in *19th IEEE International Conference on Micro Electro Mechanical Systems*, 2006, no. January, pp. 886–889.

[19] S. Lucyszyn and S. Pranonsatit, "RF MEMS for Antenna Applications," in *7th European Conference on Antennas and Propagation*, 2013, pp. 1988–1992.

[20] M. Kim, J. B. Hacker, R. E. Mihailovich, and J. F. Denatale, "A DC-to-40 GHz Four-Bit RF MEMS True-Time," *IEEE Microwave and Wireless Components Letters*, vol. 11, no. 2, pp. 56–58, 2001.

[21] C. L. Goldsmith, A. Malczewski, Z. J. Yao, S. Chen, J. Ehmke, D. H. Hinzel, R. S. Corporation, N. C. Expressway, and M. S. Dallas, "RF MEMs Variable Capacitors for Tunable Filters," *International Journal of RF and Microwave Computer-Aided Engineering*, no. 4, pp. 362–374, 1999.

[22] X. Li, Y. Xia, J. Liu, L. Yin, Y. Liu, D. Fang, and H. Zhang, "Tunable RF MEMS capacitor for wireless communication," *International Conference*

on Optical Instruments and Technology, vol. 7510, pp. 1–9, 2009.

[23] R. Mahameed, M. a El-Tanani, and G. M. Rebeiz, “A zipper RF MEMS tunable capacitor with interdigitated RF and actuation electrodes,” *Journal of Micromechanics and Microengineering*, vol. 20, 2010.

[24] A. Oz and G. K. Fedder, “RF CMOS-MEMS capacitor having large tuning range,” in *12th International Conference on Solid-State Sensors, Actuators and Microsystems*, 2003, pp. 412–415.

[25] V. M. Lubecke, B. Barber, E. Chan, D. Lopez, M. E. Gross, and P. Gammel, “Self-assembling MEMS variable and fixed RF inductors,” *IEEE Transactions on Microwave Theory and Techniques*, vol. 49, no. 11, pp. 2093–2098, 2001.

[26] I. Zine-El-Abidine, M. Okoniewski, and J. G. McRory, “RF MEMS tunable inductor,” in *15th International Conference on Microwaves, Radar and Wireless Communications*, 2004, vol. 3, pp. 612–614.

[27] D. Fang, H. Zhang, and N. C. Tien, “A review of the tunable microinductors,” *Micronanoelectronic Technology*, no. March, 2010.

[28] G. M. Rebeiz, *RF MEMS: Theory Design and Technology*. Hoboken, NJ: John Wiley & Sons, Inc., 2003.

[29] S. Pranonsatit and S. Lucyszyn, “Self-assembled screen-printed microwave inductors,” *Electronics Letters*, vol. 41, no. 23, pp. 23–24, 2005.

[30] R. R. A. Syms, “Surface tension powered self-assembly of 3-D micro-optomechanical structures,” *Journal of Microelectromechanical Systems*,

vol. 8, no. 4, pp. 448–455, 1999.

[31] G. W. Dahlmann, E. M. Yeatman, P. R. Young, I. D. Robertson, and S. Lucyszyn, "MEMS high Q microwave inductors using solder surface tension self-assembly," *IEEE MTT-S International Microwave Sympsoium Digest*, vol. 1, pp. 329–332, 2001.

[32] A. Hobby, "Screen printing for the industrial user," *DEK*, 1997. .

[33] "Screen Printing as a Manufacturing Process." PDS International Limited.

[34] S.-J. Kim, C.-Y. Kang, J.-W. Choi, D.-Y. Kim, M.-Y. Sung, H.-J. Kim, and S.-J. Yoon, "Properties of piezoelectric actuator on silicon membrane, prepared by screen printing method," *Materials Chemistry and Physics*, vol. 90, no. 2–3, pp. 401–404, Apr. 2005.

[35] B. Dziurdzia, "Photoimageable Thick-Films in Microwaves," *Advancing Microelectronics*, vol. 29, no. 2, 2002.

[36] D. Stopel, K.-H. Drue, S. Humbla, M. Mach, T. Mache, a. Rebs, G. Reppe, G. Vogt, M. Hein, and J. Muller, "Fine-line structuring of microwave components on LTCC substrates," *3rd Electronics System Integration Technology Conference ESTC*, pp. 1–6, Sep. 2010.

[37] J.-P. Bertinet, E. Leleux, J.-P. Cazenave, J.-P. Ganne, M. Pate, R. Lebourgeois, E. Mueller, and F. Bechtold, "Filtering capacitors embedded in LTCC substrates for RF and microwave applications," *Microwave Journal*, vol. 50, no. 11, pp. 72–88, Nov. 2007.

[38] R. Kulke, M. Rittweger, P. Uhlig, and C. Gunner, "LTCC - multilayer

ceramic for wireless and sensor applications," *Produktion von Leiterplatten und Systemen (PLUS)*, no. 12, pp. 2131 – 2136, Dec. 2001.

[39] M. Hrovat, D. Belavic, J. Cilensek, S. Drnovsek, J. Holc, and M. Jerlah, "Investigation of sacrificial layers for 3D LTCC structures and some preliminary results," in *32nd International Spring Seminar on Electronics Technology*, 2009, pp. 1–6.

[40] M. Hintz and A. Albrecht, "Advanced LTCC processes using pressure assisted sintering," in *SMTA Pan Pacific Symposium*, 2004, pp. 1–6.

[41] L. E. Khoong, Y. M. Tan, and Y. C. Lam, "Overview on fabrication of three-dimensional structures in multi-layer ceramic substrate," *Journal of the European Ceramic Society*, vol. 30, no. 10, pp. 1973–1987, Aug. 2010.

[42] F. Lautzenhiser and E. Amaya, "HeraLock TM 2000 Self-constrained LTCC Tape," in *International Conference on Advanced Packaging and Systems (ICAPS)*, 2002, pp. 143–149.

[43] H. Birol, T. Maeder, and P. Ryser, "Preparation and application of minerals-based sacrificial pastes for fabrication of LTCC structures," in *4th European Microelectronics and Packaging Symposium*, 2006, vol. 3, pp. 57–60.

[44] H. Birol, T. Maeder, and P. Ryser, "Application of graphite-based sacrificial layers for fabrication of LTCC (low temperature co-fired ceramic) membranes and micro-channels," *Journal of Micromechanics and Microengineering*, vol. 17, no. 1, pp. 50–60, Jan. 2007.

[45] H. Birol, T. Maeder, C. Jacq, G. Corradini, R. Passerini, Y. Fournier, S.

Straessler, and P. Ryser, “Fabrication of LTCC micro-fluidic devices using sacrificial carbon layers,” *Journal of Applied Ceramic Technology*, no. 2, pp. 345–354, 2005.

[46] I. Wolff, “From Antennas to Microwave Systems - LTCC as an Integration Technology for Space Applications -,” in *3rd European Conference on Antennas and Propagation*, 2009, pp. 3–8.

[47] B. Hunt, “Ultra High temperature operating electronics for high reliability harsh environment applications,” in *IMAPS-UK CirciT*, 2013.

[48] P. Uhlig, C. Günner, S. Holzwarth, J. Kassner, R. Kulke, A. Lauer, and M. Rittweger, “LTCC short range radar sensor for automotive applications at 24 GHz,” in *37th International Symposium on Microelectronics (IMAPS)*, 2004, pp. 14–18.

[49] K. Wu, “Integration and interconnect techniques of planar and non-planar structures for microwave and millimeter-wave circuits - current status and future trend,” in *Asia-Pacific Microwave Conference (AMPC)*, 2001, pp. 411–416.

[50] M. F. Shafique and I. D. Robertson, “Laser machining of microvias and trenches for substrate integrated waveguides in LTCC technology,” in *Proceedings of the 39th European Microwave Conference*, 2009, pp. 272–275.

[51] L. Jin, R. M. A. Lee, and I. Robertson, “Analysis and design of a novel low-loss hollow substrate integrated waveguide,” *IEEE Transactions on Microwave Theory and Techniques*, vol. 62, no. 8, pp. 1616–1624, Aug.

2014.

[52] R. M. A. Lee, L. Jin, I. Robertson, and A. Farzamnia, “Integrated waveguide slot antenna and cavity filter using hollow SIW in LTCC technology,” in *1st International Conference on Telematics and Future Generation Networks (TAFGEN)*, 2015, pp. 82–85.

[53] M. F. Shafique, K. Saeed, D. P. Steenson, and I. D. Robertson, “Laser prototyping of microwave circuits in LTCC technology,” *IEEE Transactions on Microwave and Techniques*, vol. 57, no. 12, pp. 3254–3261, 2009.

[54] C. H. Newborn, J. M. English, and D. J. Coe, “LTCC Fabrication for a Leaf Spring Vertical Actuator,” *International Journal of Applied Ceramic Technology*, vol. 3, no. 1, pp. 61–67, Jan. 2006.

[55] M. A. Fonseca, J. M. English, M. von Arx, and M. G. Allen, “Wireless micromachined ceramic pressure sensor for high-temperature applications,” *Journal of Microelectromechanical Systems*, vol. 11, no. 4, pp. 337–343, Aug. 2002.

[56] K. Vaed, J. Florkey, S. a. Akbar, M. J. Madou, J. J. Lannutti, and S. S. Cahill, “An additive micromolding approach for the development of micromachined ceramic substrates for RF applications,” *Journal of Microelectromechanical Systems*, vol. 13, no. 3, pp. 514–525, Jun. 2004.

[57] H. Sedaghat Pisheh, Y. Komijany, S. Mohajerzadeh, M. Shahabadi, and M. Araghchini, “Design, simulation, and fabrication of on-chip conical spiral antennas for millimeter-wave wireless communications,” *2005 Joint 30th*

International Conference on Infrared and Millimeter Waves and 13th International Conference on Terahertz Electronics, vol. 2, pp. 553–554, 2005.

[58] J. L. Ocaña, M. Morales, J. A. Porro, O. Garcia, C. Molpeceres, and M. Holgado, "Short pulse laser shock microforming of thin metal MEMS components," in *Lasers and Electro-Optics 2009 and the European Quantum Electronics Conference*, 2009.

[59] S. Yoshioka, T. Miyazaki, T. Misu, R. Oba, and M. Saito, "Laser forming of thin foil by a newly developed sample holding method," *Journal of Laser Applications*, vol. 15, no. 2, p. 96, May 2003.

[60] M. M. Michaelis and A. Forbes, "Laser propulsion : a review," *South African Journal of Science*, vol. 102, no. July, pp. 289–295, 2006.

[61] G. Bergstue and R. L. Fork, "Beamed energy for ablative propulsion on near earth space," in *62nd International Astronautical Congress*, 2011.

[62] B. Richerzhagen, R. Housh, F. Wagner, J. Manley, W. San, and J. Ave, "Water Jet Guided Laser Cutting: a Powerful Hybrid Technology for Fine Cutting and Grooving," *Synova*.

[63] M. Kumagai, N. Uchiyama, E. Ohmura, R. Sugiura, K. Atsumi, and K. Fukumitsu, "Advanced dicing technology for semiconductor Wafer - Stealth dicing," *IEEE Transactions on Semiconductor Manufacturing*, vol. 20, no. 3, pp. 259–265, Aug. 2007.

[64] X. Zhao, B. Zhou, R. Zhang, and Z. Chen, "Research on Laser Trimming of Silicon MEMS Vibratory Gyroscopes," *Integrated Ferroelectrics*, vol. 1,

no. 129, pp. 37–44, 2011.

[65] S. Lucyszyn, H. Q. Wang, and I. D. Robertson, “0.1 THz rectangular waveguide on GaAs semi-insulating substrate,” *IEE Electronics Letters*, vol. 31, no. 9, pp. 721–722, Apr. 1995.

[66] S. Lucyszyn, D. Budmir, H. Q. Wang, and I. D. Robertson, “Design of compact monolithic dielectric-filled metal-pipe rectangular waveguides for millimetre-wave applications,” *IEE Proceedings – Microwaves, Antennas and Propagation*, vol. 143, no. 5, pp. 451–453, Oct. 1996.

[67] M. S. Aftanasar, P. R. Young, I. D. Robertson, J. Minalgiene, and S. Lucyszyn, “Photoimageable thick-film millimetre-wave metal-pipe rectangular waveguides,” *IEE Electronics Letters*, vol. 37, no. 18, pp. 1122–1123, Aug. 2001.

[68] S. Papantonis, N. M. Ridler, and S. Lucyszyn, “Rectangular waveguide enabling technology using holey surfaces and wire media metamaterials,” *Sensors and Actuators A: Physical*, vol. 209, pp. 1–8, Mar. 2014.

[69] Y. Zhou and S. Lucyszyn, “Modelling of reconfigurable terahertz integrated architecture (RETINA) SIW structures,” *Progress in Electromagnetics Research (PIER) Journal*, vol. 105, pp. 71–92, Jun. 2010.

[70] H. Uchimura, T. Takenoshita, and M. Fujii, “Development of the laminated waveguide,” *IEEE MTT-S International Microwave Symposium*, vol. 3, pp. 1811–1814, Jun. 1998.

[71] D. Stephens, P. R. Young, and I. D. Robertson, “Millimeter-wave substrate integrated waveguides and filters in photoimageable thick-film

technology," *IEEE Transactions on Microwave and Techniques*, vol. 53, no. 12, pp. 3832–3837, Dec. 2005.

[72] R. Moro, M. Bozzi, A. Collado, A. Georgiadis, and S. Via, "Plastic-based Substrate Integrated Waveguide (SIW) Components and Antennas," in *42nd European Microwave Conference*, 2012, pp. 1007–1010.

[73] F. Parment, S. Member, A. Ghiotto, and S. Member, "Air-Filled Substrate Integrated Waveguide for Low-Loss and High Power-Handling Millimeter-Wave Substrate Integrated Circuits," *IEEE Transactions on Microwave Theory and Techniques*, vol. 63, no. 4, pp. 1228–1238, Apr. 2015.

[74] I. Stil, A. L. Fontana, B. Lefranc, A. Navarrini, P. Serres, and K. F. Schuster, "Loss of WR10 waveguide across 70-116 GHz," in *22nd International Symposium on Space Terahertz Technology*, 2012.

[75] P. J. Chou and R. Siemann, "Measurements of losses in EDMed waveguides and in first W-band structure," *ARDB Tech. Note 99*, Jun. 1997.

[76] W. R. McGrath, C. Walker, M. Yap, and Y.-C. Tai, "Silicon micromachined waveguides for millimeter-wave and submillimeter-wave frequencies," *IEEE MIicrowave and Guided Wave Letters*, vol. 3, no. 3, pp. 61–63, Mar. 1992.

[77] S. Lucyszyn, "The future of on-chip terahertz metal-pipe rectangular waveguides implemented using micromachining and multilayer technologies," in *IEE Colloquium on Terahertz Technology and Its Applications*, 1997, pp. 10/1–10/10.

[78] K. M. K. H. Leong, K. Hennig, C. Zhang, R. N. Elmadjian, Z. Zhou, B. S. Gorospe, P. P. Chang-Chien, V. Radisic, and W. R. Deal, "WR1.5 silicon micromachined waveguide components and active circuit integration methodology," *IEEE Transactions on Microwave Theory and Techniques*, vol. 60, no. 4, pp. 998–1005, Apr. 2012.

[79] E. Episkopou, P. Stergios, and S. Lucyszyn, "Optically-controlled plasma switch for integrated terahertz applications," in *IEEE International Conference on Plasma Science (ICOPS)*, 2012, p. 3P–43.

[80] T. J. Reck, C. Jung-Kubiak, J. Gill, and G. Chattopadhyay, "Measurement of silicon micromachined waveguide components at 500-750 GHz," *IEEE Transactions on Terahertz Science and Technology*, vol. 4, no. 1, pp. 33–38, Jan. 2014.

[81] S. W. Moon, C. M. Mann, B. J. Maddison, I. C. E. Turcu, R. Allot, S. E. Huq, and N. Lisi, "Terahertz waveguide components fabricated using a 3D x-ray microfabrication technique," *Electronics Letters*, vol. 32, no. 19, pp. 1794–195, Sep. 1996.

[82] C. E. Collins, B. M. Towlson, L. S. Karatzas, G. M. Parkhurst, J. M. Chamberlain, J. W. Bowen, R. D. Pollard, R. E. Miles, D. P. Steenson, D. A. Brown, and N. J. Cronin, "Integrated micro-machined antenna for 200 GHz operation," *IEEE MTT-S International Microwave Symposium*, vol. 2, pp. 561–564, Jun. 1997.

[83] C. E. Collins, R. E. Miles, J. W. Digby, G. M. Parkhurst, R. D. Pollard, J. M. Chamberlain, and D. P. Steenson, "Micro-machined 'snap-together'

rectangular waveguide for terahertz circuits," in *IEEE Sixth International Conference on Terahertz Electronics*, 1998, pp. 176–178.

[84] J. W. Digby, C. E. McIntosh, G. M. Parkhurst, B. M. Towlson, S. Hadjiloucas, J. W. Bowen, J. Martyn Chamberlain, R. D. Pollard, R. E. Miles, D. Paul Steenson, L. S. Karatzas, N. J. Cronin, and S. R. Davies, "Fabrication and characterization of micromachined rectangular waveguide components for use at millimeter-wave and terahertz frequencies," *IEEE Transactions on Microwave Theory and Techniques*, vol. 48, no. 8, pp. 1293–1302, Aug. 2000.

[85] S. Hadjiloucas, B. M. Towlson, L. S. Karatzas, S. T. G. Wootton, N. J. Cronin, S. R. Davies, C. E. McIntosh, J. M. Chamberlain, R. E. Miles, and R. D. Pollard, "Micromachined waveguide antennas for 1.6 THz," *Electronics Letters*, vol. 42, no. 15, pp. 842–843, Jul. 2006.

[86] C. H. Smith, A. Sklavonuos, and N. Scott Barker, "SU-8 micromachining of millimeter and submillimeter waveguide circuits," *IEEE MTT-S International Microwave Symposium Digest*, pp. 961–964, Jun. 2009.

[87] N. A. Murad, M. J. Lancaster, P. Gardner, M. L. Ke, and Y. Wang, "Micromachined H-plane horn antenna manufactured using thick SU-8 photoresist," *IET Electronics Letters*, vol. 46, no. 11, p. 743, May 2010.

[88] X. Shang, M. L. Ke, Y. Wang, and M. J. Lancaster, "Micromachined WR-3 waveguide filter with embedded bends," *IET Electronics Letters*, vol. 47, no. 9, pp. 545–547, Apr. 2011.

[89] X. Shang, M. L. Ke, Y. Wang, and M. J. Lancaster, "WR-3 band

waveguides and filters fabricated using SU8 photoresist micromachining technology," *IEEE Transactions on Terahertz Science and Technology*, vol. 2, no. 6, pp. 629–637, Nov. 2012.

[90] X. Shang, Y. Tian, M. J. Lancaster, and S. Singh, "A SU8 micromachined WR-1.5 band waveguide filter," *IEEE Microwave and Wireless Components Letters*, vol. 23, no. 6, pp. 300–302, May 2013.

[91] F. Sammoura, Y.-C. Su, Y. Cai, C.-Y. Chi, B. Elamaran, L. Lin, and J.-C. Chiao, "Plastic 95-GHz rectangular waveguides by micro molding technologies," *Sensors and Actuators, A: Physical*, vol. 127, no. 2, pp. 270–275, Mar. 2006.

[92] F. Sammoura, Y. Cai, C.-Y. Chi, T. Hirano, L. Lin, and J.-C. Chiao, "A micromachined W-band iris filter," in *13th International Conference on Solid State Sensors and Actuators and Microsystems*, 2005, vol. 1, pp. 1067–1070.

[93] C. Reilly, W. J. Chappell, J. Halloran, K. Sarabandi, J. Volakis, N. Kikuchi, and L. P. B. Katehi, "New fabrication technology for ceramic metamaterials," in *IEEE Antennas and Propagation Society International Symposium*, 2002, vol. 2, pp. 376–379.

[94] W. J. Chappell, C. Reilly, J. Halloran, and L. P. B. Katehi, "Ceramic synthetic substrates using solid freeform fabrication," in *IEEE Transactions on Microwave Theory and Techniques*, 2003, vol. 51, no. 3, pp. 752–760.

[95] X. Gong, B. Liu, L. P. B. Katehi, and W. J. Chappell, "Layer-by-layer stereolithography (SL) of complex medium," in *IEEE Antennas and*

Propagation Society International Symposium, vol. 1, pp. 325–328.

[96] B. Liu, X. Gong, and W. J. Chappell, "Layer-by-layer polymer stereolithography fabrication for three-dimensional RF components," *IEEE MTT-S International Microwave Symposium Digest*, vol. 2, pp. 481–484, Jun. 2004.

[97] X. Gong, A. Margomenos, B. Liu, W. J. Chappell, and L. P. B. Katehi, "High-Q evanescent-mode filters using silicon micromachining and polymer stereolithography (SL) processing," *IEEE MTT-S International Microwave Symposium Digest*, vol. 2, pp. 433–436, Jun. 2004.

[98] A. Buerkle, K. Brakora, and K. Sarabandi, "Fabrication of a DRA array using ceramic stereolithography," *IEEE Antennas and Wireless Propagation Letters*, vol. 5, no. 1, pp. 479–482, Dec. 2006.

[99] K. Brakora, J. Halloran, and K. Sarabandi, "Design of 3-D monolithic MMW antennas using ceramic stereolithography," *IEEE Transactions on Antennas and Propagation*, vol. 55, no. 3, pp. 790–797, Mar. 2007.

[100] K. Brakora, J. Halloran, and K. Sarabandi, "Subwavelength periodic lattices for the design of MMW components using ceramic stereolithography," in *IEEE Antennas and Propagation Society International Symposium*, 2006, pp. 4511–4514.

[101] K. Brakora and K. Sarabandi, "Integration of single-mode photonic crystal clad waveguides with monolithically constructed ceramic subsystems," *IEEE Antennas and Wireless Propagation Letters*, vol. 8, pp. 433–436, Aug. 2008.

[102] K. Brakora and K. Sarabandi, “Integration of single-mode photonic crystal waveguides to monolithic MMW subsystems constructed using ceramic stereolithography,” in *IEEE Antennas and Propagation Society International Symposium*, 2007, pp. 2550–2553.

[103] N. Delhote, D. Baillargeat, S. Verdeyme, C. Delage, and C. Chaput, “Narrow Ka bandpass filters made of high permittivity ceramic by layer-by-layer polymer stereolithography,” in *36th European Microwave Conference (EuMC)*, 2006, pp. 510–513.

[104] T. Chartier, C. Duterte, N. Delhote, D. Baillargeat, S. Verdeyme, C. Delage, and C. Chaput, “Fabrication of millimeter wave components via ceramic stereo- and microstereolithography processes,” *Journal of the American Ceramic Society*, vol. 91, no. 8, pp. 2469–2474, Jul. 2008.

[105] N. T. Nguyen, N. Delhote, M. Ettorre, D. Baillargeat, L. Le Coq, and R. Sauleau, “Design and characterization of 60-GHz integrated lens antennas fabricated through ceramic stereolithography,” *IEEE Transactions on Antennas and Propagation*, vol. 58, no. 8, pp. 2757–2762, 2010.

[106] a. H. Khalil, N. Delhote, S. Pacchini, J. Claus, D. Baillargeat, S. Verdeyme, and H. Leblond, “3-D pyramidal and collective Ku band pass filters made in Alumina by ceramic stereolithography,” *IEEE MTT-S International Microwave Symposium Digest*, vol. 4, no. 1, pp. 4–7, 2011.

[107] Y. Lee, X. Lu, Y. Hao, S. Yang, R. Ubic, J. R. G. Evans, and C. G. Parini, “Rapid prototyping of ceramic millimeterwave metamaterials: simulations and experiments,” *Microwave and Optical Technology Letters*, vol. 49, no.

9, pp. 895–896, Sep. 2007.

[108] L. Schulwitz and A. Mortazawi, “A compact millimeter-wave horn antenna array fabricated through layer-by-layer stereolithography,” in *IEEE Antennas and Propagation Society International Symposium*, 2008, pp. 1–4.

[109] P. T. Timbie, J. Grade, D. Van Der Weide, B. Maffei, and G. Pisano, “Stereolithographed MM-wave corrugated horn antennas,” in *36th International Conference on Infrared, Millimeter, and Terahertz Waves*, 2011, pp. 11–13.

[110] W. G. Whittow, C. C. Njoku, and J. C. Vardaxoglou, “Patch antennas with heterogeneous substrates and reduced material consumption enabled by additive manufacturing techniques,” in *IEEE Antennas and Propagation Society International Symposium*, 2012.

[111] W. G. Whittow, S. S. Bukhari, L. A. Jones, and I. L. Morrow, “Applications and future prospects for microstrip antennas using heterogeneous and complex 3-D geometry substrates,” *Progress in Electromagnetics Research (PIER)*, vol. 144, pp. 271–280, 2014.

[112] B. Sanz-Izquierdo and E. A. Parker, “3-D Printing of elements in frequency selective arrays,” *IEEE Transactions on Antennas and Propagation*, vol. 62, no. 12, pp. 6060–6066, Dec. 2014.

[113] Z. Wu, J. Kinast, M. E. Gehm, and H. Xin, “Rapid and inexpensive fabrication of terahertz electromagnetic bandgap structures,” *Optics Express*, vol. 16, no. 21, pp. 16442–16451, Oct. 2008.

[114] P. Nayeri, M. Liang, R. A. Sabory-garc, M. Tuo, F. Yang, M. Gehm, H. Xin, and A. Z. Elsherbeni, "3D printed Dielectric Reflectarrays: Low-Cost High-Gain Antennas at Sub-Millimeter Waves," *IEEE Transactions on Antennas and Propagation*, vol. 62, no. 4, pp. 2000–2008, Apr. 2014.

[115] A. Macor, E. de Rijk, S. Alberti, T. Goodman, and J.-P. Ansermet, "Note: Three-dimensional stereolithography for millimeter wave and terahertz applications," *Review of Scientific Instruments*, vol. 83, no. 4, p. 046103, Apr. 2012.

[116] A. von Bieren, E. de Rijk, J.-P. Ansermet, and A. Macor, "Monolithic Metal-Coated Plastic Components for mm-Wave Applications," in *39th International Conference on Infrared, Millimeter and Terahertz waves (IRMMW-THz)*, 2014, vol. 1.

[117] "Swiss to 12 - Metal Coated Plastics." [Online]. Available: http://www.swissto12.com/Products/Metal Coated Plastics/index.html. [Accessed: 08-May-2015].

[118] J. S. Chieh, B. Dick, S. Loui, and J. D. Rockway, "Development of a Ku - band corrugated conical horn using 3-D print technology," *IEEE Antennas and Propagation Letters*, vol. 13, pp. 201–204, Jan. 2014.

[119] C. Guo, X. Shang, M. J. Lancaster, and J. Xu, "A 3-D printed lightweight X-band waveguide filter based on spherical resonators," *IEEE Microwave and Wireless Components Letters*, vol. 25, no. 7, pp. 442–444, Jul. 2015.

[120] N. Hopkinson and P. Dickens, "Analysis of rapid manufacturing — Using layer manufacturing process for production," *Proc. Inst. Mech. Eng., Part*

C: J. Mechanical Engineering Science, vol. 217, no. 1, pp. 31–39, Apr. 2003.

[121] A. Weber, “Case study: Kelly Manufacturing Company - A turn for the better,” *Stratasys*, Aug-2013. [Online]. Available: http://www.stratasys.com/resources/case-studies/aerospace/kelly-manufacturing.

[122] G. Schmidt and U. Eidenschink, “Case study: BMW Refensburg - Rapid manufacturing with FDM in jig & fixture construction,” *Stratasys*, Jul-2013. [Online]. Available: http://www.stratasys.com/resources/case-studies/automotive/bmw.

[123] A. Rutter and V. Sharma, “Type A Machines - Low volume, agile, additive manufacturing and capital costs,” *Type A Machines*, Nov-2014. [Online]. Available: http://www.typeamachines.com/pages/white-paper.

[124] A. Kreemer and Z. H. Moe, “Rapid manufacturing using FDM systems,” in *Handbook of Manufacturing Engineering and Technology*, A. Nee, Ed. London, UK: Springer, 2014, pp. 1–11.

[125] G. O. Mallory and J. B. Hajdu, *Electroless Plating: Fundamentals and Applications*. Orlando, FL: American Electroplaters and Surface Finishers Society, 1990.

[126] “Waveguide loss.” [Online]. Available: http://www.microwaves101.com/encyclopedias/waveguide-loss. [Accessed: 15-May-2015].

[127] “Accura Xtreme Plastic datasheet.” [Online]. Available:

www.3dsystems.com/products/datafiles/datasheets/SLA/DS_Accura_Xtreme_US.pdf. [Accessed: 19-Feb-2015].

[128] "Assessment of surface texture. Guidance and general information," *British Standard BS 1134*. 2010.

[129] G. F. Engen and C. a. Hoer, "Thru-Reflect-Line: an improved technique for calibrating the dual six-port automatic network analyzer," *IEEE Transactions on Microwave Theory and Techniques*, vol. 27, no. 12, pp. 987–993, Dec. 1979.

[130] A. Rumiantsev and N. M. Ridler, "VNA calibration," *IEEE Microwave Magazine*, vol. 9, no. 3, pp. 86–99, Jun. 2008.

[131] N. M. Ridler, "News in RF impedance measurements," in *XXVIIth General Assembly of the International Union of Radio Science (URSI)*, 2002.

[132] N. M. Ridler, "A review of existing naional measurement standards for RF and microwave impedance parameters in the UK," *IEE Colloquium Digest*, no. 0008, pp. 6/1–6, Feb. 1999.

[133] F. L. Warner, "Attenuation Measurement," in *Microwave Measurements*, 2nd ed., A. E. Bailey, Ed. London: IEE, 1989, pp. 132–134.

[134] "DuPont 6143 - Pd/Ag Post-fire Conductor." Technical datashet.

[135] C. E. Chrisostomidis and S. Lucyszyn, "On the theory of chained-function filters," *IEEE Transactions on Microwave Theory and Techniques*, vol. 53, no. 10, pp. 3142–3151, Oct. 2005.

[136] GWT, "WG Filter Tool - Iris Filter." [Online]. Available:

http://www.guidedwavetech.com/wgchoose.htm.

[137] A. Poithier and T. Vaha-Heikkila, "Impedance tuners and tuneable filters," in *Advanced RF MEMS*, S. Lucyszyn, Ed. Cambridge: Cambridge University Press, 2010, pp. 271–306.

[138] E. Brookner, "Phased-array radars," *Scientific American*, vol. 252, pp. 94–102, 1985.

[139] H. T. Friis and C. B. Feldman, "A multiple unit steerable antenna for short-wave reception," *Proceedings of the Institute of Radio Engineers*, vol. 25, pp. 841–917, 1937.

[140] P. V. Brennan, "Low cost phased array antenna for land-mobile satcom applications," *IEE Proceedings – Microwaves, Antennas and Propagation*, vol. 138, pp. 131–136, 1991.

[141] C. Alakija and S. P. Stapleton, "A mobile base station phased array antenna," in *IEEE International Conference on Wireless Communications*, 1992, pp. 118–121.

[142] R. Schneider and J. Wenger, "System aspects for future automotive radar," in *IEEE MTT-S International Microwave Symposium*, 1999, vol. 1, p. 269.

[143] I. Gresham, A. Jenkins, R. Egri, C. Eswarappa, F. Kolak, R. Wohlert, J. Bennett, and J. P. Lanteri, "Ultra wide band 24GHz automotive radar front-end," in *IEEE MTT-S International Microwave Symposium*, 2003, vol. 1, pp. 369–372.

[144] J. Wenger, "Automotive radar - status and perspectives," in *IEEE*

Compound Semiconductor Integrated Circuit Symposium, 2005, p. 4.

[145] D. M. Pozar, "Ferrite phase shifters," in *Microwave Engineering*, 4th ed., John Wiley & Sons, 1997, pp. 482–487.

[146] G. F. Bland and A. G. Franco, "Phase shift characteristics of dielectric loaded waveguide," in *PGMTT National Symposium Digest*, 1961, vol. 62, no. 1, pp. 112–118.

[147] C. T. M. Chang, "Partially dielectric-slab-filled waveguide phase shifter," *IEEE Transactions on Microwave Theory and Techniques*, vol. 22, no. 5, pp. 481–485, May 1974.

[148] F. Arndt, J. Bornemann, and R. Vahldieck, "Design of Multisection Impedance-Matched Dielectric-Slab Filled Waveguide Phase Shifters," *IEEE Transactions on Microwave Theory and Techniques*, vol. 32, no. 1, pp. 34–39, 1984.

[149] F. Arndt, A. Frye, M. Wellnitz, and R. Wirsing, "Double dielectric-slab-filled waveguide phase shifter," *IEEE Transactions on Microwave Theory and Techniques*, vol. 33, no. 5, pp. 373–381, May 1985.

[150] M. Jeong, V. Kazmirenko, Y. Poplavko, B. Kim, and S. Baik, "Electrically tunable phase shifters with air-dielectric sandwich structure," *Materials Research Society Symposium Proceedings*, vol. 720, no. H3.12, 2002.

[151] R. S. Rao, "Phase shifters," in *Microwave Engineering*, New Delhi: PHI, 2012, pp. 258–259.

[152] S. K. Koul, "Dielectric-insert phase shifter," in *Microwave and Millimeter*

Wave Phase Shifters - Vol. 1, S. K. Koul and B. Bhat, Eds. Boston: Artech House, 1991, pp. 72–73.

[153] P. I. Deffenbaugh, R. C. Rumpf, and K. H. Church, “Broadband microwave frequency characterization of 3-D printed materials,” *IEEE Transactions on Components, Packaging and Manufacturing Technology*, vol. 3, no. 12, pp. 2147–2155, Dec. 2013.

[154] “DuPont Green Tape Material System Design and Layout Guidelines.”

[155] “Green Tape 9K7 - low temperature co-fired ceramic system,” *DuPont*. Technical datasheet.

[156] J. M. Gere and S. P. Timoshenko, *Mechanics of material*, 4th SI. Cheltenham: Stanley Thornes, 1999.

[157] S. Lucyszyn, “Review of radio frequency microelectromechanical systems technology,” *IEE Proceedings – Science, Measurement and Technology*, vol. 151, no. 2, pp. 93–103, Mar. 2004.

[158] “DuPont Fodel 5989 - Photoimageable Thick-Film Paste.” Technical datasheet.

[159] S. Muckett and J. Minalgene, “‘Hibridas’ photoimageable thick film process and materials for microwave and sensor component applications,” in *2nd 1998 IEMT/IMC Symposium*, 1998, pp. 154–160.

[160] “TIMCAL TIMREX KS10 Primary Synthetic Graphite.” Technical datasheet.

[161] Z. Feng, H. Zhang, K. C. Gupta, W. Zhang, V. M. Bright, and Y. C. Lee,

"MEMS-based series and shunt variable capacitors for microwave and millimeter-wave frequencies," *Sensors and Actuators*, vol. 91, no. 3, pp. 256–265, Jul. 2001.

[162] I. Cho, T. Song, S. Baek, and E. Yoon, "A low-voltage and low-power RF MEMS series and shunt switches actuated by combination of electromagnetic and electrostatic forces," *IEEE Transactions on Microwave Theory and Techniques*, vol. 53, no. 7, pp. 2450–2457, Jul. 2005.

[163] J. Y. Park, H. C. Lee, and J. U. Bu, "Low Voltage Operated Piezoelectric RF MEMS Switches for Advanced Handset Applications," in *34th European Microwave Conference*, 2004, pp. 1437–1440.

[164] D. Elata and V. Leus, "Electromechanical modelling of electrostatic actuators," in *Advanced RF MEMS*, S. Lucyszyn, Ed. Cambridge: Cambridge University Press, 2010, pp. 23–27.

[165] S. Pamidighantam, R. Puers, K. Baert, and H. A. C. Tilmans, "Pull-in voltage analysis of electrostatically actuated beam structures with fixed-fixed and fixed-free end conditions," *Journal of Micromechanics and Microengineering*, vol. 12, no. 4, pp. 458–464, Jun. 2002.

[166] K. A. Ramakrishnan and H. T. Srinivasan, "Closed form models for pull-in voltage of electrostatically actuated cantilever beams and comparative analysis of cantilevers and microgripper," *Journal of Electrical Engineering*, vol. 63, no. 4, pp. 242–248, Jul. 2012.

[167] C. Do, M. Lishchynska, K. Delaney, and M. Hill, "Generalized closed-form

models for pull-in analysis of micro cantilever beams subjected to partial electrostatic load," *Sensors and Actuators, A: Physical*, vol. 185, pp. 109–116, Jul. 2012.

[168] T. Hennige, S. Holzer, F. Vollertsen, and M. Geiger, "On the working accuracy of laser bending," *Journal of Materials Processing Technology*, vol. 71, no. 3, pp. 422–432, Apr. 1997.

[169] F. Lambiase, "An analytical model for evaluation of bending angle in laser forming of metal sheets," *Journal of Materials Engineering and Performance*, vol. 21, no. 10, pp. 2044–2052, Feb. 2012.

[170] M.-L. Chen, J. Jeswiet, P. J. Bates, and G. Zak, "Experimental study on sheet metal bending with medium-power diode laser," *Proceedings of the Institution of Mechanical Engineers, Part B: Journal of Engineering Manufacture*, vol. 222, no. 3, pp. 381–389, Nov. 2008.

[171] H. Arnet and F. Vollertsen, "Extending laser bending for the generation of convex shapes," *Proceedings of the Institution of Mechanical Engineers, Part B: Journal of Engineering Manufacture*, vol. 209, no. 6, pp. 433–442, Jul. 1995.

[172] G. Chen, X. Xu, C. C. Poon, and a. C. Tam, "Experimental and numerical studies on microscale bending of stainless steel with pulsed laser," *Journal of Applied Mechanics*, vol. 66, no. 3, pp. 772–779, Sep. 1999.

[173] W. Shichun and Z. Jinsong, "An experimental study of laser bending for sheet metals," *Journal of Materials Processing Technology*, vol. 110, no. 2, pp. 160–163, May 2001.

[174] B. S. Yilbas and S. S. Akhtar, “Laser bending of metal sheet and thermal stress analysis,” *Optics & Laser Technology*, vol. 61, pp. 34–44, Sep. 2014.

[175] E. Gärtner, J. Frühauf, U. Löschner, and H. Exner, “Laser bending of etched silicon microstructures,” *Microsystem Technologies*, vol. 7, no. 1, pp. 23–26, Apr. 2001.

[176] X. R. Zhang and X. Xu, “Laser bending for high-precision curvature adjustment of microcantilevers,” *Applied Physics Letters*, vol. 86, no. 2, Sep. 2005.

[177] W. Li and Y. L. Yao, “Buckling based laser forming process: concave or convex,” in *ICALEO 2000: Laser Materials Processing Conference*, 2000.

[178] J. L. Ocaña, M. Morales, C. Molpeceres, O. García, J. a. Porro, and J. J. García-Ballesteros, “Short pulse laser microforming of thin metal sheets for MEMS manufacturing,” *Applied Surface Science*, vol. 254, no. 4, pp. 997–1001, Sep. 2007.

[179] D. Robben, S. F. Peik, T. Henning, M. Becker, and K. Froehner, “Laser machined microsystems for active frequency selective surfaces,” *IEEE MTT-S International Microwave Symposium Digest*, pp. 12–14, Jun. 2012.

[180] I. De Wolf, “Reliability,” in *Advanced RF MEMS*, S. Lucyszyn, Ed. Cambridge: Cambridge University Press, 2010, pp. 109–139.

[181] “DuPont LL612 - Co-fired silver conductor.” Technical datasheet.

[182] J. R. Thorpe, D. P. Steenson, and R. E. Miles, “High frequency transmission line using micromachined polymer dielectric,” *Electronics*

Letters, vol. 34, no. 12, pp. 1237–1238, Jun. 1998.

[183] J. Melai, C. Salm, S. Smits, J. Visschers, and J. Schmitz, “The electrical conduction and dielectric strength of SU-8,” *Journal of Micromechanics and Microengineering*, vol. 19, no. 6, pp. 065012.1–7, May 2009.

[184] D. Karnakis, G. Rutterford, and M. R. H. Knowles, “High power DPSS laser micro-machining of stainless steel and silicon for device singulation,” *Oxford Lasers Ltd.*, 2005.

[185] J. M. Bovatsek and R. S. Patel, “Highest-speed dicing of thin silicon wafers with nanosecond-pulse 355nm q-switched laser source using line-focus fluence optimization technique.,” *SPIE Proceedings: Laser-based Micro- and Nanopackaging and Assembly IV*, vol. 7585, Feb. 2010.

[186] L. Migliore, K. Lee, K. Jeong-moog, and C. Byung-kew, “Advances in laser singulation of silicon,” in *ICALEO*, 2006, pp. 237–242.

[187] C. T. Pan, Y. M. Hwang, and C. W. Hsieh, “Fast fabrication of silicon based microstructures using 355 nm UV laser,” *Materials Science and Technology*, vol. 21, no. 11, pp. 1344–1348, 2005.

[188] E. W. Kreutz, R. Weichenhain, and A. Horn, “Nd : YAG laser micromachining of SiC precision structures for MEMS,” *SPIE Proceedings: MEMS Design, Fabrication, Characterization, adn Packaging*, vol. 4007, pp. 109–118, Nov. 2001.

[189] J. P. Desbiens and P. Masson, “ArF excimer laser micromachining of Pyrex, SiC and PZT for rapid prototyping of MEMS components,” *Sensors and Actuators, A: Physical*, vol. 136, no. 2, pp. 554–563, 2007.

[190] C. Molpeceres, S. Lauzurica, J. J. García-Ballesteros, M. Morales, and J. L. Ocaña, "Advanced 3D micromachining techniques using UV laser sources," *Microelectronic Engineering*, vol. 84, no. 5, pp. 1337–1340, 2007.

[191] M. Kagerer, F. Irlinger, and T. C. Lueth, "Laser source independent basic parameters in micro-cutting," in *IEEE/ASME International Conference on Advanced Intelligent Mechatronics (AIM)*, 2011, pp. 391–396.

[192] M. Kagerer, F. Irlinger, and T. C. Lueth, "Laser source independent basic parameters - Focus position, pulse overlap, track overlap - in laser micro milling using as rapid manufacturing process," in *IEEE/ASME International Conference on Advanced Intelligent Mechatronics (AIM)*, 2012, pp. 135–140.

[193] D. H. Kam, L. Shah, and J. Mazumder, "Femtosecond laser machining of multi-depth microchannel networks onto silicon," *Journal of Micromechanics and Microengineering*, vol. 21, no. 4, p. 045027, 2011.

[194] M. El-Bandrawy and M. C. Gupta, "Femtosecond laser micromachining of silicon for MEMS," *SPIE Proceedings: Photon Processing in Microelectronics and Photonics II*, vol. 4977, pp. 219–225, 2003.

[195] K. L. Choo, Y. Ogawa, G. Kanbargi, V. Otra, L. M. Raff, and R. Komanduri, "Micromachining of silicon by short-pulse laser ablation in air and under water," *Materials Science and Engineering: A*, vol. 372, pp. 145–162, 2004.

[196] "Spectra-Physiscs Talon DPSS UV Laser." Technical datasheet.

[197] R. K. Roy, *A primer on the Taguchi method*, 2nd ed. Dearborn, MI, USA: Society of Manufacturing Engineers, 2010.

[198] R. K. Roy, *Design of Experiments using the Taguchi method*. New York, NY, USA: John Wiley & Sons, 2001.

[199] M. D'Auria and N. Tolou, "UV-Laser Cutting for Silicon MEMS Prototyping : Improving Etching Rate and Quality," in *14th euspen International Conference*, 2014, vol. 2, pp. 275–279.

APPENDIX I

A: Influencing factors and corresponding levels for the first iteration of the Taguchi DOE

Symbol	Factor Name	Factor Level			
		Level 1	Level 2	Level 3	Level 4
A	Frequency (kHz)	5	10	15	20
B	Diode Current (A)	4.5	5	5.5	6
C	Pulse Overlap (%)	60	70	80	90
D	Number of Patterns	3	4	5	6
E	Gap Size (μm)	15	20	25	30

B: L`16 orthogonal array

L`16 Orthogonal Array					
Test Condition	Factors and Levels				
	A	B	C	D	E
1	1	1	1	1	1
2	1	2	2	2	2
3	1	3	3	3	3
4	1	4	4	4	4
5	2	1	2	3	4
6	2	2	1	4	3
7	2	3	4	1	2
8	2	4	3	2	1
9	3	1	3	4	2
10	3	2	4	3	1
11	3	3	1	2	4
12	3	4	2	1	3
13	4	1	4	2	3
14	4	2	3	1	4
15	4	3	2	4	1
16	4	4	1	3	2

C: Machining time for each of the test runs and mean S/N ratio for the first Taguchi DOE iteration.

Test Condition	**Time (s)**			
	Test 1	**Test 2**	**Test 3**	**Average**
1	1206	1246	1252	1235
2	975	918	944	946
3	747	682	636	688
4	524	475	487	495
5	991	509	510	670
6	556	519	507	527
7	374	340	343	352
8	301	299	303	301
9	474	472	477	474
10	291	290	293	291
11	226	215	237	226
12	230	225	222	226
13	289	294	289	291
14	182	190	204	192
15	201	204	206	204
16	200	189	189	193

Factor Symbol	Machining Time - Mean S/N Ratio (dB)				
	Level 1	Level 2	Level 3	Level 4	Max. Delta (|*Max*|-|*Min*|)
A	-58.008	-52.990	-49.242	-46.706	11.302
B	-55.404	-52.232	-50.248	-49.062	6.342
C	-52.267	-52.440	-51.386	-50.852	1.588
D	-51.381	-51.362	-52.189	-52.014	0.827
E	-51.718	-52.421	-51.891	-50.916	1.505

D: Average surface roughness for each of the test runs and mean S/N ratio for the first Taguchi DOE iteration.

Test Condition	Average Surface Roughness (µm)			
	Test 1	Test 2	Test 3	Average
1	0.54	0.41	0.39	0.44
2	0.50	0.37	0.44	0.44
3	0.45	0.42	1.28	0.72
4	1.60	2.09	2.33	2.01
5	0.61	0.85	0.54	0.66
6	0.40	0.46	0.43	0.43
7	0.32	0.39	0.39	0.37
8	0.48	0.46	0.55	0.50
9	0.28	0.46	0.40	0.38
10	0.51	1.19	0.43	0.71
11	0.46	1.53	0.66	0.88
12	0.34	0.42	0.55	0.43
13	0.79	0.58	0.46	0.61
14	0.50	0.37	0.50	0.46
15	0.60	0.70	0.59	0.63
16	0.45	0.51	0.55	0.50

Factor Symbol	Surface Roughness - Mean S/N Ratio (dB)				
	Level 1	Level 2	Level 3	Level 4	Max. Delta (|*Max*|-|*Min*|)
A	2.240	6.363	4.351	5.192	3.943
B	5.661	5.812	3.623	3.230	2.582
C	5.073	5.404	5.665	2.184	3.481
D	7.354	4.318	3.300	3.354	4.054
E	4.786	7.486	5.060	0.993	6.493

E: Taper angle for each of the test runs and mean S/N ratio for the first Taguchi DOE iteration.

Test Condition	Taper angle (deg)			
	Test 1	Test 2	Test 3	Average
1	2.89	2.90	2.97	2.92
2	3.36	3.61	3.43	3.46
3	4.08	3.06	2.99	3.38
4	3.05	3.36	2.47	2.96
5	3.82	6.38	6.38	5.53
6	6.59	6.21	6.21	6.33
7	2.41	2.63	2.53	2.52
8	3.04	3.27	3.26	3.19
9	4.58	4.89	4.95	4.81
10	3.37	3.45	3.60	3.47
11	6.11	3.81	4.76	4.90
12	3.16	2.85	3.24	3.08
13	4.52	4.65	4.94	4.70
14	3.89	2.63	2.61	3.04
15	4.33	4.33	4.58	4.41
16	4.39	4.88	5.24	4.84

Factor Symbol	Taper Angle - Mean S/N Ratio (dB)				
	Level 1	Level 2	Level 3	Level 4	Max. Delta (|*Max*|-|*Min*|)
A	-10.067	-12.303	-12.053	-12.474	2.407
B	-12.865	-11.871	-11.391	-10.771	2.094
C	-13.253	-12.135	-11054	-10.453	2.800
D	-9.244	-12.072	-12.563	-13.017	3.773
E	-10.778	-11.548	-12.489	-12.081	1.711

F: ANOVA results for the first iteration of the Taguchi DOE.

Factor Symbol	Contribution (%)	
	Average Surface Roughness	Taper Angle
A	11.5	14.9
B	8.6	8
C	13	18.2
D	10.9	30.1
E	24	6
Error	32	22.8
Total	100	100

APPENDIX II

A: Average surface roughness for each of the test runs and mean S/N ratio for the second Taguchi DOE iteration considering interactions.

Test Condition	Average Surface Roughness (µm)		
	Test 1	Test 2	Average
1	0.4467	0.4400	0.4433
2	0.4333	0.3833	0.4083
3	0.4467	0.4067	0.4267
4	0.2767	0.3833	0.3300
5	0.4800	0.4500	0.4650
6	0.2333	0.2533	0.2433
7	0.6267	0.7000	0.6633
8	0.3000	0.3133	0.3067
9	0.4433	0.5167	0.4800
10	0.4200	0.4133	0.4167
11	0.4000	0.4067	0.4033
12	0.4167	0.4000	0.4083
13	0.2500	0.2733	0.2617
14	0.2667	0.2600	0.2633
15	0.3300	0.4000	0.3650
16	0.2300	0.2700	0.2500
17	0.3967	0.5600	0.4783
18	0.5833	0.7600	0.6717
19	1.5967	1.6433	1.6200
20	0.5867	0.53	0.5583
21	0.3800	0.3800	0.3800
22	0.8167	0.6667	0.7417
23	0.3300	0.3133	0.3217
24	0.5167	0.46	0.4883
25	0.4833	0.5933	0.5383
26	0.6400	0.7967	0.7183
27	1.3833	0.9233	1.1533

Factor Symbol	**Average Surface Roughness** - Mean S/N Ratio (dB)			
	Level 1	Level 2	Level 3	Max. Delta (|*Max*|-|*Min*|)
A	6.120352	7.57253	6.565435	1.452178
B	7.463679	7.757468	5.037169	2.720299
C	6.083293	8.776052	5.398971	3.377081
D	8.454539	6.65041	5.153367	3.301172
E	7.868526	8.542755	3.847035	4.695721

B: Taper angle for each of the test runs and mean S/N ratio for the second Taguchi DOE iteration considering interactions.

Test Condition	Taper Angle (deg)		
	Test 1	Test 2	Average
1	2.2034	2.0972	2.1503
2	2.7944	2.6855	2.7399
3	3.5125	3.9444	3.7284
4	2.1244	3.1399	2.6322
5	3.8901	3.6239	3.7570
6	2.0400	1.7456	1.8928
7	1.4239	1.4266	1.4253
8	2.0127	2.1217	2.0672
9	2.2062	2.0672	2.1367
10	4.1616	3.8901	4.0259
11	2.9005	2.7944	2.8474
12	3.3548	3.2215	3.2882
13	2.4704	2.2034	2.3369
14	3.4119	3.1671	3.2895
15	4.184684	4.0802	4.1324
16	1.9855	2.0945	2.0400
17	1.5330	1.4512	1.4921
18	2.5793	2.2552	2.4172
19	4.3163	4.2376	4.2769
20	4.6661	4.4790	4.5726
21	3.9200	3.6239	3.7719
22	3.9987	3.9173	3.9580
23	2.8461	2.8733	2.8597
24	2.5493	3.5424	3.0459
25	2.2307	2.2552	2.2429
26	2.9304	2.0127	2.4716
27	3.7842	4.1073	3.9458

Factor Symbol	Taper Angle - Mean S/N Ratio (dB)			
	Level 1	Level 2	Level 3	Max. Delta (|*Max*|-|*Min*|)
A	-8.39664	-8.86954	-9.69114	1.294495
B	-9.16683	-8.8342	-8.95629	0.332624
C	-10.6393	-9.61783	-6.70018	3.939133
D	-7.60865	-8.77272	-10.576	2.967304
E	-7.81955	-9.02484	-10.1129	2.293381